Doctoral Thesis

Comprehensive research on the deformation mechanics, support design and health assessment of mountain tunnel in soft rock

September 2017

Nagasaki University

Graduate School of Science and Technology

Xuezhen Wu

Acknowledgements

It would not have been possible to finish this doctoral thesis without the support of the kind people around me, to only some of whom it is possible to give particular mention here.

First and foremost, I would like to thank my supervisor, Prof. **Yujing Jiang**, a respectable, responsible and resourceful scholar, for his constant encouragement and guidance in the past six years. He taught me not only the skill of writing a research paper, but also the method of solving problems which is invaluable in my future study. He has provided precious guidance to my career and life planning.

Second, I am extremely grateful to Professor **Akihide Tada**, Professor **Kiyoshi Omine**, Professor **Susumu Ogawa** in Nagasaki University for their generous help and continuous supports during my daily life and research. I am very thankful to **Gang Wang** in Shandong University of Science and Technology, for his fundamental assistance and guidance in getting my Master's degree. Moreover, I would like to express my gratitude to Assistant Professor **Bo Li** in Nagasaki University, for his kind supports and valuable friendship.

I would like to thank my friends in Nagasaki, Dr. **Yang Gao**, Dr. **Richeng Liu**, Dr. **Zhaofeng Li**, Dr. **Yan Du**, Dr. **Liyuan Yu**, Dr. **Xiaoshan Wang**, Dr. **Xiao Shi**, Mr. **Chen Wang**, Miss **Na Huang**, Mr. **Xuepeng zhang**, Mr. **Bin Gong**, Mr. **Changsheng Wang** and all others who helped make my stay in Japan a very pleasant one.

Finally, I would like to thank my wife **Jianhua Wang**. During the whole time of study, she always supported and encouraged me and gave birth to our beautiful daughter **Doudou Wu**. Words are not sufficient to express the overwhelming love for her. Also, I would like to thank my parents, for their love, patience and support over my entire lifetime.

Xuezhen Wu

June 2017

ABSTRACT

Nowadays, the tunnels play an increasing important role in the modern society from many aspects. Meanwhile, tunneling is an exciting and rapidly evolving technology, and one of the few areas in civil engineering where new horizons are constantly being discovered. This doctor thesis is expected to present some contributions to the evolving discipline from some aspects, including the issue on the deformation mechanics of tunnel, the support design of tunnel in soft rock, and the health assessment method of tunnel lining.

First, a modified strain-softening model is proposed to account for the non-linear stress-strain behaviors of rocks. An equivalent residual strength, which is found to have a negative exponential relations with the confining pressure, is defined to quantify the strength of rocks in the post-failure stage. The parameters involved in the model are estimated via non-linear regression analysis upon a series of stress-strain curves. The new model can realize the gradually transition from strain-softening features to idealized elastoplastic with the increasing of confining pressure. The influence of diverse post-failure behaviors of rock was demonstrated in ground reaction analyses. Moreover, considering the effect of the confining pressure on Young's modulus, the stress and deformation of rock mass around a circular tunnel were calculated by both analytical and numerical methods. The influence of the confining-dependent Young's modulus in surrounding rock was estimated quantitatively in the ground reaction analyses. Tawara saka Tunnel in Japan was taken as an example to explain the influence of confining-dependent Young's modulus. The results show that the error with respect to the monitoring data was largely reduced with the confining-dependent Young's modulus model, which also indicate the necessary of considering the non-uniform distribution of Young's modulus.

Second, a specifically designed rock bolt, called Tension and Compression Coupled Yielding bolt was presented, which is promising to provide support for both squeezing and burst-prone rock mass encountered in mining and tunneling at depth. The performance of the conventional bolt and the new bolt subjected to fracture opening is tested. Shear tests are performed to examine the performance of different rock bolts subjected to fracture sliding. The shear behavior of rock bolt inserted in the rough joints, with the JRC ranging from 0 to 18, was investigated with a series of single shear tests under CNL condition. A dimensionless mathematical model was established to predict the shear behaviour of rock bolt inserted in different roughness conditions. Two tests with natural rough joints were conducted to verify the applicability of proposed mathematical model for the natural rough joints. Moreover, an interaction model is

proposed to describe the interaction between the energy-absorbing rock bolt and the rock mass. The proposed method was programmed in a Visual Basic environment, and a semi-analytical solution for the coupling model was achieved. The reinforcement mechanism of the energy-absorbing rock bolt in conventional tunneling is clearly demonstrated through an illustrative case study. The reinforcement effect of the energy-absorbing rock bolt under different conditions was estimated quantitatively, and its mechanical work transfer ability is presented. In addition, the validity of the proposed method was verified through numerical simulations.

Finally, a new method was proposed for the health assessment of tunnel lining, which evaluate the lining states according to the fractal dimension of cracks. A series of comparative tests and field tests were conducted to evaluate the validity of this new method. The fractal dimensions of tunnel lining cracks were obtained according to the digital inspection test of Hidake Tunnel in Japan. The correlation between fractal dimension and TCI of tunnel lining was studied. The significance of the new evaluation index is that it can identify the unusual spans of tunnel lining and provide a basis for further internal testing. As a complement to the conventional visual inspection method, the fractal dimension of the cracks is a promising health assessment index. Moreover, a new method for the health assessment of tunnel lining was proposed by Jiang et al., which can evaluate the whole structural condition according to the vibration properties of tunnel lining. The correlation of vibration properties and crack index of tunnel lining in evaluating risk of collapsing was examined in this thesis. A series of field tests were conducted to evaluate the validity of this new method and to make a comparative analysis with the visual inspection test results.

Keywords: Strain-softening model; Post-failure behavior; Confining pressure; Semi-analytical solution; Numerical simulation; Young's modulus; High in-situ stress; Yielding rock bolt; Pull tests; Shear tests; Joint roughness; Shear behaviour; Support system design; Tunnel lining; Health assessment; Fractal dimension; Tunnel-lining Crack Index; Digital inspection test; Vibration properties

Contents

1 Introduction

1.1 Background

A tunnel is an underground passageway, dug through the surrounding soil/earth/rock and enclosed except for entrance and exit, commonly at each end. It may be for foot or vehicular road traffic, for rail traffic, or for a canal. The central portions of a rapid transit network are usually in tunnel. Some tunnels are aqueducts to supply water for consumption or for hydroelectric stations or are sewers.

The oldest known tunnel in the world is Bomvu Ridge in Swaziland in southern Africa, which was in operation before 4,000 years. During the Roman time, many tunnels were built for a variety of purposes such as military, transportation, water supply and drainage. Some of these Roman tunnels are still in use, such as the aqueduct tunnel built in Athens by the Emperor Hadrian 1,800 years ago.

During the ages of Industrial Revolution, the application of explosive and the invention of rock drilling tools (e.g. pneumatic or electric drills) did speed up the rock-break process, and gave a tremendous impetus to tunneling practice. A canal tunnel situated at Malpas was built to connect France's Atlantic coast with the Mediterranean Sea in 1681, which was the first tunnel excavated by gunpowder. Auburn Tunnel in Pennsylvania, which was built during 1818-1821, was the first tunnel in American with the length of 182m. Stimulated by the boom of railway construction, the second half of 19th century has been called as the golden age of tunneling, and is typified by such great projects as the 20km long Simplon Tunnel through the Alps and the 18km long Moffat Tunnel through the Rockies.

At the beginning of 20th century, the replacement of timbering by steel linings, rock bolts and shotcrete represents another greatest achievement in the history of tunneling. It reduced the tunneling cost significantly and made the tunneling in soft ground feasible. Thanks to these new means of support and the progress in scientific knowledge, the sprayed concrete lining method reached maturity in the 1950's. Based on these achievements, the new Austria tunneling method (NATM) was developed and generalized by Muller et al. at the same period. On the other hand, the mechanized tunneling method (TBMs) and submerged tube method also emerged in the 1960's. Stimulated by the infrastructure construction in urban area, these two methods gained a rapid development the last two or three decades.

Tunneling practice is going on development in the 21st century. Engineers sometimes would face with the challenges of constructing super long and super large tunnels in complicated geological conditions, and also face with the challenges of maintaining the numerous tunnels during their service time. Tunnel maintenance has become an increasing important issue in some developed countries, since the infrastructure construction boom has completed in last century. Unlike the purely man-made structures (e.g. buildings and bridges), tunnel is a combination of man-made materials (steel and concrete) and natural materials (rocks and soils). Therefore, the issue of tunnel maintenance is not only concerned with the deterioration of man-made materials but also the features of surrounding rock mass and the varying of in-site geological conditions. Nowadays, the tunnels play an increasing important role in the modern society from many aspects. Meanwhile, tunneling is an exciting and rapidly evolving technology, and one of the few areas in civil engineering where new horizons are constantly being discovered. This doctor thesis is expected to present some contributions to the evolving discipline from some aspects.

1.1.1 The deformation mechanics of tunnel

New Austrian Tunnelling method (NATM) is a well-recognized technique in conventional tunnelling. In engineering practice however, the analytical and numerical methods are inevitably required to estimate the stress and deformation of surrounding rock mass and to help the design of support system qualitatively.

Generally, the idealized elastoplastic model was adopted for the rocks in the early stage of rock mechanics. Considering the softening behavior of rocks in the post-failure stage, the strain-softening model was adopted more and more in recent years. The post-failure behavior is important in rock engineering as the rocks surrounding deep buried excavations are basically in post-peak state in most cases. It is necessary to evaluate the exact mechanical behavior of rocks in different states for effective support design and maintenance.

A large number of laboratory experiments have shown that the rocks in the post-peak state presented strain-softening features under low confining pressure, and gradually evolved into idealized elastoplastic with the increasing of confining pressure. Due to the complex distribution of confining pressure in engineering practice, neither the idealized elastoplastic model nor the strain-softening model can accurately reflect the behavior of rocks surrounding the deep buried excavation.

The non-uniform distribution of Young's modulus is considered as an important incentive that influence the convergence of fractured rock mass and the soft rock. Numerous papers were contributed to the determination of Young's modulus of rocks during the past several decades. Some of them were focused on the relationship of the Young's modulus and the uniaxial compressive strength (UCS), rock mass rating (RMR) and geological strength index (GSI) for different type of rocks. Some other works were concentrated on the influence of confining pressure on the Young's modulus, and some empirical equations were obtained. However, the attempt to describe the exact influence of the confining-dependent Young's modulus of rock mass in the ground reaction analyses is quite few.

In engineering practice, the distribution of confining pressure is very complex. For a general excavation, the confining pressure acting on the excavation surface is zero. It increases gradually with the increasing distance between the element and the excavation surface, and will reach a constant value at locations far away from the excavation. Hence, the confining pressure acting on an element is a function of distance between the element and the excavation boundary. Since the post-peak behavior and Young's modulus is depended on the confining pressure, it is necessary to consider the stress field change in the rock mass surrounding the excavation to accurately predict the ground response, especially in deep buried excavations.

1.1.2 Support system design of tunnel

Many mines around the world are currently being operated at depths greater than 1000m, for example those in China, Germany, Australia, and South Africa. Some mountain tunnels for traffic and water diversion tunnel in water power project are buried under 2000m. The substantial difference of the rock mass at great depth and at shallow depth is the significant increase of in-situ stresses. High stress in surrounding rock mass can cause serious stability problems such as squeezing in soft rock and rock burst in hard rock.

It is observed that many conventional bolts fail when experiencing large shear and opening displacement at rock joints/fractures. The conventional rock bolt is easy to be damaged when experiencing large rock displacement. The premature failure of conventional rock bolt implies that it is too stiff to sustain rock dilations in high stress condition. The support system applied in high in-situ stress condition should be able to carry high load and accommodate large deformation of rock mass.

Yielding support was first proposed and used in the deep gold mines of South Africa. So far, there have been dozens of yielding rock bolts. According to the yielding mechanism, they can be summarized as structural components sliding type and steel deformation type. The structural components sliding type bolt mainly includes Cone bolt, Roofex, He-bolt and Cold drawing bolt. The typical representative of steel deformation rock bolt is D bolt. It is a smooth steel bar with a number of anchors along its length. Due to the limits in load capacity, deformation ability, stability and economy, it is difficult to say the performance of these bolt is absolutely satisfactory. There is large industrial requirement on developing a performance-reliable and cost-effective yielding support system.

Rock mass stabilization by bolting is an effective and economical means, which has been used for more than a century. Rock bolts develop their strength during the convergence of rock mass, especially in the jointed rock mass. Bolted joints can be subjected to two categories of movements, either to opening in a direction perpendicular to the plane or to shear displacements occurring in the plane. Generally, much more attention is paid to the pull-out capacity of rock bolt to prevent the opening of rock joint. The shear resistance of rock bolt is always not considered in the support designing. However, a case study by McHugh and Signer indicated that shear loading contributed significantly to the failure of anchoring systems. A high proportion of rock bolts have been found to fail duo to the shearing of high stress rock masses.

The shear performance of rock bolt is just as significant as tensile performance. Many experiments have been performed to study the mechanical behavior of rock bolts in resisting the shear force. Some factors that can influence the shear behavior were studied systematically, including bolt type, bolt diameter, bolt surface profile, bolt material, bolt inclination, bolt pretension, rock strength and normal pressure. Although many experiments have been performed to study the mechanical behaviour of rock bolts in resisting the shear force. However, almost all the tests were conducted on smooth rock joints, which is inconsistent with the field engineering practice. In nature, joints without any geometric irregularities are very rare. Joint roughness is one of the most important factors for understanding and estimating the shear behavior of a rock joint.

Energy-absorbing rock bolts have been widely used for rock reinforcement in mining and civil engineering under high-stress conditions. However, the mechanism of the interaction between the energy-absorbing rock bolt and rock mass is still not entirely

clear at present; no analytical model is available for the qualitative prediction of its reinforcement effect. The supporting design that employs the energy-absorbing rock bolt is still empirical or semi-empirical, and it is difficult to evaluate its performance quantitatively. The mechanical work that the energy-absorbing rock bolt can transfer on the rock mass is an important ability, which can be used to estimate its support effect. However, there is no published research work that is focused on this topic. Therefore, it is imperative to develop a reasonable model to predict the mechanical work transfer ability of energy-absorbing rock bolts in practical engineering and to quantify their performance in the context of the supporting design.

1.1.3 Health assessment of mountain tunnel lining

A large number of tunnels have been in service for the past decades all over the world. The tunnels were mainly supported by concrete lining. The persistent ageing and seismic activity lead to many problems to the concrete lining, such as cracking, corrosion and leakage. The damage of tunnel lining will decrease its integrity and subsequently increase the risk of tunnel lining collapse. In order to deal with this situation, there is an urgent requirement for accurate tunnel lining health assessment methods.

Generally, the stability of aged cast-in-place tunnel lining was mainly evaluated based on the visual inspection. But the evaluation standard was qualitative, and the results depended on the experience of different engineers. As a solution of this problem, the Tunnel-lining Crack Index (TCI) was proposed to quantitatively evaluate the severity of tunnel lining cracks. It has been widely applied for the inspecting of surface defects of tunnels in Japan. The stability assessment based on TCI is reasonable to some extent because the mechanical stability of a tunnel is greatly influenced by the severity of cracks in the lining. However, the intersection and distribution of cracks, which could greatly influence the stability of tunnel lining, was not considered in TCI. The uncertainty relationship between TCI and the instability of tunnel lining called for more alternative assessment methods and health indexes.

Fractal theory is used to analyze the distribution of complex graphics. It has been widely used in art, astronomy, geography, biology, fluid dynamics, probability theory, chaos theory, and pure mathematics in the past few decades. In recent years, the fractal theory was used to describe the propagation of cracks in rock or concrete specimens in laboratory. These studies confirmed that the cracks in concrete have fractal properties. Therefore, it is possible to describe the distribution of cracks and evaluate the states of tunnel lining by fractal theory.

Moreover, it is questionable to predict tunnel lining failure only by the crack at the

lining surface. The uncertainty relationship between the crack characteristics and the instability of tunnel lining require more alternative assessment methods. Some different methods, such as the magnetic method, ultrasonic method and ground penetrating radar method, were proposed. However, only local information of the structure can be measured in these techniques. A lot of time and cost are required to estimate the overall tunnel.

Recently, evaluating the structural condition according to the vibration properties of tunnel lining has attracted the attention of many researchers. However, these attempts have encountered great difficulties as the forced vibration test was adopted. The forced vibration test is not suitable for the damage detection of large-scale structures, where the huge reaction mass shakers are necessary. A more effective approach was proposed by the Gao et al., which evaluated condition of tunnel lining the by ambient vibration test. The vibration measurements by seismometer is a promising way to evaluate the global stability of tunnel lining.

1.2 Objective and thesis structure

This thesis mainly consists of three parts as shown in Fig. 1. Part I includes chapter 2 and chapter 3, and deal with the issue on the deformation mechanics of tunnel. Part II includes chapter 4, chapter 5 and chapter 6, and deal with the issue on the support design of tunnel in soft rock. Part III includes chapter 7 and chapter 8, and deal with the issue on the health assessment method of tunnel lining.

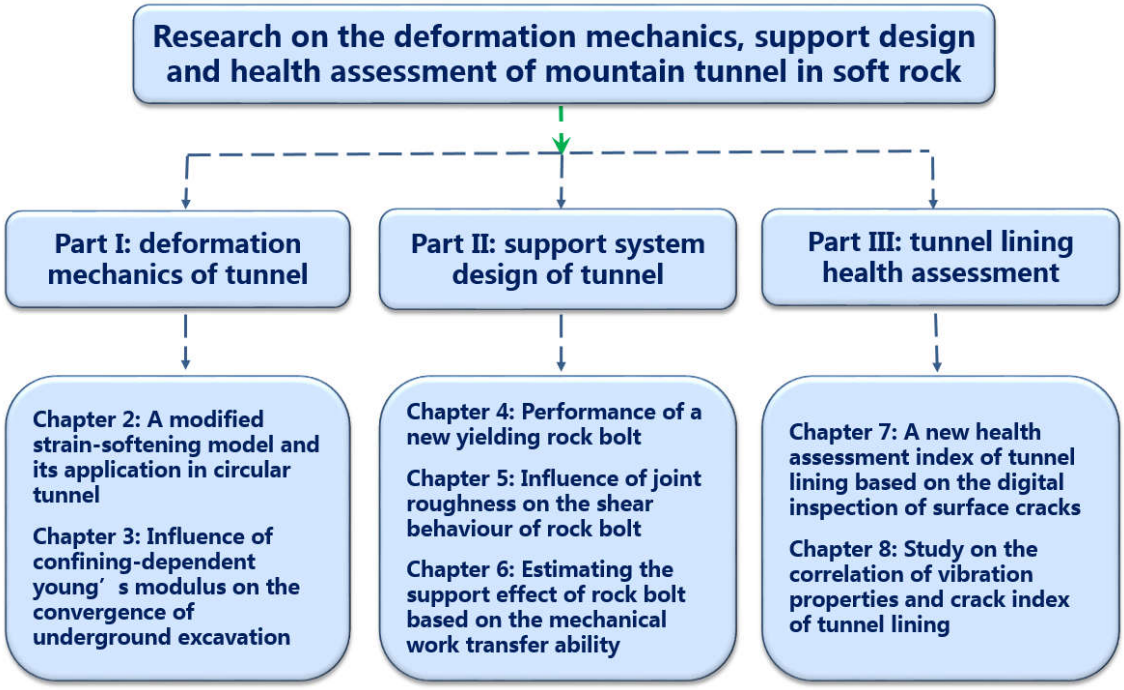

Fig. 1 The structure of this thesis

Chapter 1 gives a brief introduction of the background, the objective and the structure of this thesis.

In Chapter 2, a modified strain-softening model is proposed to account for the non-linear stress-strain behaviors of rocks. It is promising to realize the gradually transition from strain-softening features to idealized elastoplastic with the increasing of confining pressure. The influence of diverse post-failure behaviors of rock will be demonstrated in ground reaction analyses.

In Chapter 3, the stress and deformation of rock mass around a circular tunnel were calculated by both analytical and numerical methods, considering the effect of the confining pressure on Young's modulus. The influence of the confining-dependent Young's modulus in surrounding rock was estimated quantitatively in the ground reaction analyses.

Chapter 4 presents a specifically designed rock bolt, called Tension and Compression Coupled Yielding bolt, which is promising to provide support for both squeezing and burst-prone rock mass encountered in mining and tunneling at depth. The performance of the conventional bolt and the new bolt subjected to fracture opening is tested. Shear tests are performed to examine the performance of different rock bolts subjected to fracture sliding.

In Chapter 5, the shear behavior of rock bolt inserted in the rough joints, with the

JRC ranging from 0 to 18, was investigated with a series of single shear tests under CNL condition. A dimensionless mathematical model was established to predict the shear behaviour of rock bolt inserted in different roughness conditions. Two tests with natural rough joints were conducted to verify the applicability of proposed mathematical model for the natural rough joints.

In Chapter 6, an interaction model is proposed to describe the interaction between the energy-absorbing rock bolt and the rock mass. The proposed method was programmed in a Visual Basic environment, and a semi-analytical solution for the coupling model was achieved. The reinforcement mechanism of the energy-absorbing rock bolt in conventional tunneling is clearly demonstrated through an illustrative case study. The reinforcement effect of the energy-absorbing rock bolt under different conditions was estimated quantitatively, and its mechanical work transfer ability is presented. In addition, the validity of the proposed method was verified through numerical simulations.

In Chapter 7, a new method was proposed for the health assessment of tunnel lining, which evaluate the lining states according to the fractal dimension of cracks. A series of comparative tests and field tests were conducted to evaluate the validity of this new method. The fractal dimensions of tunnel lining cracks were obtained according to the digital inspection test of Hidake Tunnel in Japan. The correlation between fractal dimension and TCI of tunnel lining was studied.

Chapter 8 examines the correlation of vibration properties and crack index of tunnel lining in evaluating risk of collapsing. A series of field tests were conducted to evaluate the validity of this new method and to make a comparative analysis with the visual inspection test results.

Chapter 9 summarizes the major conclusions and provides some discussions of this thesis

Part I

Deformation mechanics of mountain tunnel in soft rock

2 A modified strain-softening model and its application in circular tunnel

2.1 Introduction

New Austrian Tunnelling method (NATM) is a well-recognized technique in conventional tunnelling (Kolymbas 2005). In engineering practice however, the analytical and numerical methods are inevitably required to estimate the stress and deformation of surrounding rock mass and to help the design of support system qualitatively (Detournay 1986). The convergence confinement method (CCM) presents a powerful tool for the designing of support system in NATM (Carranza et al. 1999). It is generally evaluated by analytical or semi-analytical analyses based on plane strain assumption (Jiang et al. 2001; Alonso et al. 2003; Hao et al. 2016). Numerous works were contributed to the convergence confinement method (CCM) during its several decades of development. In these studies, the rocks generally satisfied Mohr-Coulomb failure criterion (Jiang et al. 2001; Guan et al. 2007; Hasanpour et al. 2015) or Hoek-Brown failure criterion (Brown et al. 1983; Carranza et al. 2000; Lee 2008; Jiang et al. 2015). Generally, the idealized elastoplastic model was adopted for the rocks in the early stage of rock mechanics (Anagnostou 1993). Considering the softening behavior of rocks in the post-failure stage, the strain-softening model was adopted more and more in recent years (Alonso1 et al. 2003; Varas et al. 2005).

Due to the complex distribution of confining pressure in engineering practice, neither the idealized elastoplastic model nor the strain-softening model can accurately reflect the behavior of rocks surrounding the deep buried excavation. In this paper, a modified strain-softening model is proposed to account for the non-linear stress-strain behaviors of rocks. It is promising to realize the gradually transition from strain-softening features to idealized elastoplastic with the increasing of confining pressure. The influence of diverse post-failure behaviors of rock will be demonstrated in ground reaction analyses.

The post-failure behavior is important in rock engineering as the rocks surrounding deep buried excavations (i.e., excavation damaged zone, EDZ) are basically in post-peak state in most cases. It is necessary to evaluate the exact mechanical behavior of rocks in different states for effective support design and maintenance. It is well

known that the peak strength of rocks changes proportionally with the changing confining pressure (Alejano et al. 2010; Zhang et al. 2012; Omid et al. 2014). In the case of low confining pressure, rocks often fail in a form of splitting parallel to the major principal stress; when the confining pressure is moderate, rock failure is typically dominated by shear fracturing. If the confining pressure is sufficiently high, sliding between grains and micro-crack surfaces will be dominant (Fang et al. 2001; Kaiser et al. 2015). The transition of brittle to ductile behavior of rocks is one of the fundamentals of rock mechanics, and an accurate prediction of rock strength is essential for the understanding of many processes encountered in earth sciences and rock engineering.

A large number of laboratory experiments have been conducted to explore the post-failure behavior of rocks (Fang et al. 2001; Yang et al. 2008; Li et al. 2011; Walton et al. 2015). The stress-strain curve obtained in compression tests on rocks descends towards a residual state with the increasing axial strain after attainment of the peak stress (Tiwari et al. 2006; Alejano et al. 2009; Li et al. 2011; Tutluoğlu et al. 2015). The peak strength increases almost linearly with the increasing of confining pressure in most of the laboratory tests. However, the evolution of residual strength is quite different, which increased more quickly with the increasing of confining pressure, and the rocks exhibit non-linear behaviors in the residual stage (Joseph 2000). The rocks in the post-peak state presented strain-softening features under low confining pressure, and gradually evolved into idealized elastoplastic with the increasing of confining pressure. As the rock around an excavation is basically in post-peak state, the deformation and failure characteristic of the surrounding rock mass is inevitably influenced by the post-peak behaviour (Tiwari et al. 2006). However, the attempt to describe the influence of the diverse post-peak behaviors of rock mass in the ground reaction analyses is few.

Traditionally, the rock behaviour varies greatly in different conditions, and it is often assumed that the residual strength of a rock is constant, forming a uniform strength field (Fang et al. 2001). This practice is widely used in many research fields such as geophysical survey and earthquake engineering. However, the uniform strength assumption, even for the same rock domain, is unrealistic and inaccurate for rocks surrounding an underground excavation. When a tunnel is excavated, the excavation effect can lead to a complex non-uniform stress field surrounding the excavation. As shown in Fig. 1, the confining pressure (minimum principal stress) acting on the

excavation surface is zero. It increases gradually with the increasing distance between the element and the excavation surface, and will reach a constant value at locations far away from the excavation (Guan et al. 2007). Hence, the confining pressure acting on an element is a function of distance between the element and the excavation boundary. Since the post-failure behavior is depended on the confining pressure, a non-uniform strength field will be resulted. It is important to consider the stress field change in the rock mass surrounding the excavation to accurately predict the ground response, especially in deep buried excavations.

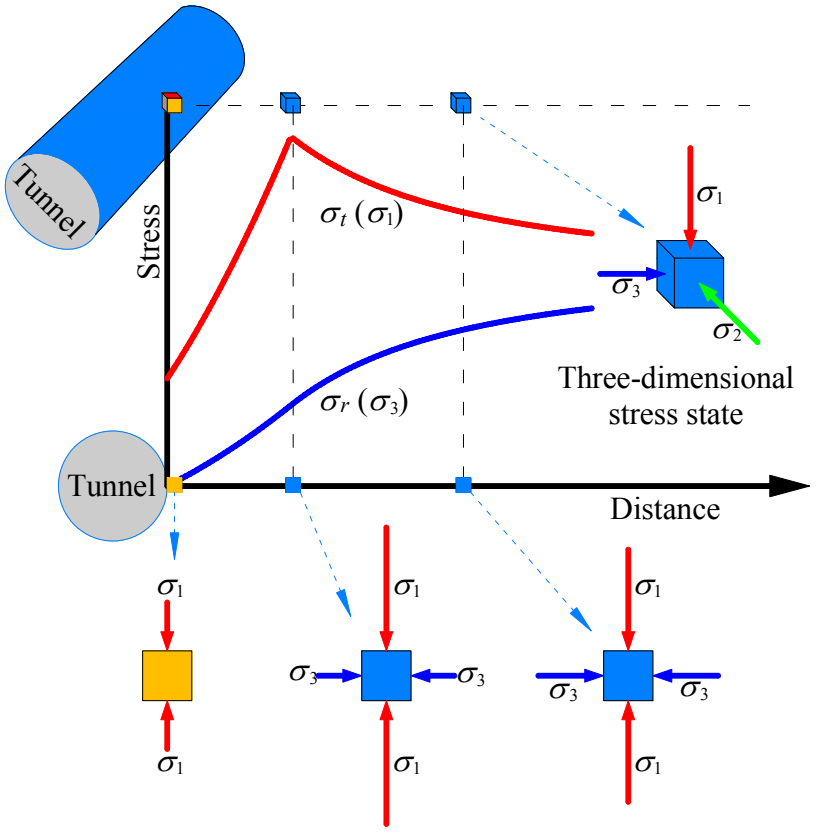

Fig. 1 A sketch illustrating the change of stresses acting on rock elements near an excavation

Due to the complex distribution of confining pressure in engineering practice, neither the idealized elastoplastic model nor the strain-softening model can accurately reflect the behavior of rocks surrounding the deep buried excavation. In this paper, a modified strain-softening model is proposed to account for the non-linear stress-strain behaviors of rocks. It is promising to realize the gradually transition from

strain-softening features to idealized elastoplastic with the increasing of confining pressure. The influence of diverse post-failure behaviors of rock will be demonstrated in ground reaction analyses.

2.2 A modified strain-softening model

2.2.1 Conventional strain-softening model

The rocks have the features of the transition from strain softening to residual state and large dilatancy under lower confining pressure. The strain-softening behavior is simplified to the form of three line segments as shown in Fig. 2 (Alonso1 et al. 2003; Guan et al. 2007). Generally, the rocks exhibiting strain-softening behavior is characterized by a transitional failure criterion $f(\sigma_{ij}, \alpha)$ and a plastic potential $g(\sigma_{ij}, \alpha)$. α is a softening parameter controlling the gradual transition of rock from a peak failure criterion to a residual one. Herein, the rock is assumed to satisfy the linear Mohr-Coulomb criterion and linear plastic potential. The major principal plastic strain ε_1^p is employed as the softening parameter, because it can be obtained easily from the results of uniaxial compression tests. Therefore, the failure criterion f and the plastic potential g can be formulated as follows, according to uniaxial compression tests.

$$f = \sigma_1 - K_p\sigma_3 - \sigma_c = \begin{cases} \sigma_1 - K_p\sigma_3 - \left(\sigma_c^1 + \dfrac{(\sigma_c^1 - \sigma_c^2)\varepsilon_1^{\,p}}{\alpha\varepsilon_{1e}}\right) & (0 \le \varepsilon_1^{\,p} \le \alpha\varepsilon_{1e}) \\ \sigma_1 - K_p\sigma_3 - \sigma_c^2 & (\varepsilon_1^{\,p} \ge \alpha\varepsilon_{1e}) \end{cases} \tag{1}$$

$$g = \sigma_1 - K_\psi\sigma_3 = \begin{cases} \sigma_1 - K_\psi^1\sigma_3 & (0 \le \varepsilon_1^{\,p} \le \alpha\varepsilon_{1e}) \\ \sigma_1 - K_\psi^2\sigma_3 & (\varepsilon_1^{\,p} \ge \alpha\varepsilon_{1e}) \end{cases} \tag{2}$$

In the above equations, K_p is the passive coefficient, and remains unchanged within the complete plastic region. σ_c is the compression strength, which transits gradually from σ_c^1 to σ_c^2, according to the evolution of the major principal plastic strain ε_1^p. K_ψ is the dilation factor, and equals to K_ψ^1 and K_ψ^2 for softening region and residual region, respectively.

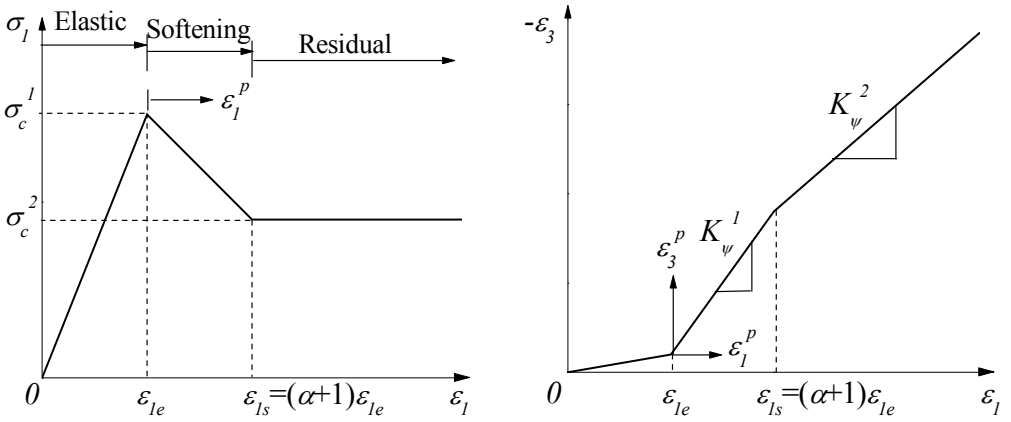

Fig. 2. Strain-softening behavior of rock samples in uniaxial compression tests

With the increasing of confining pressure, both the peak strength and residual strength increase linearly in conventional strain-softening model as shown in Fig. 3. However, the actual behavior is quite different in high confining pressure environment where the rock becomes fully ductile, and showing almost no strength reduction after failure. The residual strength is found asymptotically approaching the peak strength with the increasing of confining pressure, and almost equal when the confining pressure is large enough in a great number of laboratory tests as shown in Figs. 4-6 (Brady et al. 1992; You et al. 2007).

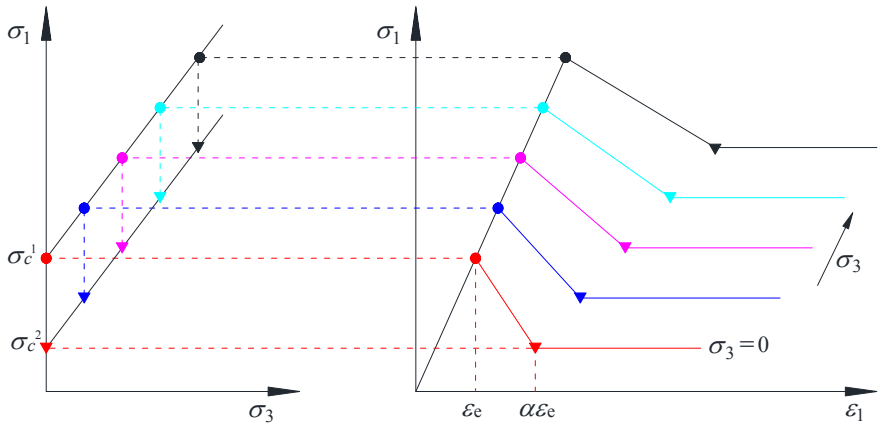

a b

Fig. 3. Conventional strain-softening model: a. evolution of strength with confining pressure; b. constitutive relation

Fig. 4a shows a set of stress-strain curves for Tennessee marble obtained in triaxial compression tests with different confining pressures (Brady et al. 1992). Following attainment of the peak stress, the stress-strain curves descend towards a residual state

with the increasing axial strain at low confining pressure. The peak strength increases almost linearly with the increasing confining pressure as shown in Fig. 4b. In contrast, the residual strength increases from considerably low values with the increasing confining pressure, and approaches the peak strength in a non-linear manner. Finally, the rock becomes fully ductile at high confining pressure, showing almost no strength reduction after failure. Similar behavior is observed in many other test results as shown in Figs. 5 and 6 (You 2007).

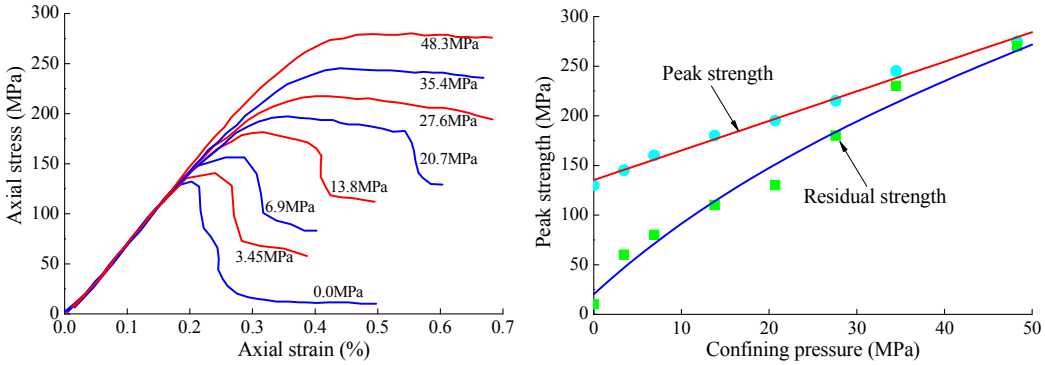

a b

Fig. 4. Tennessee marble under common triaxial compression: a. Complete axial stress-strain curves (Brady et al. 1992); b. Evolution of rock strength with confining pressure

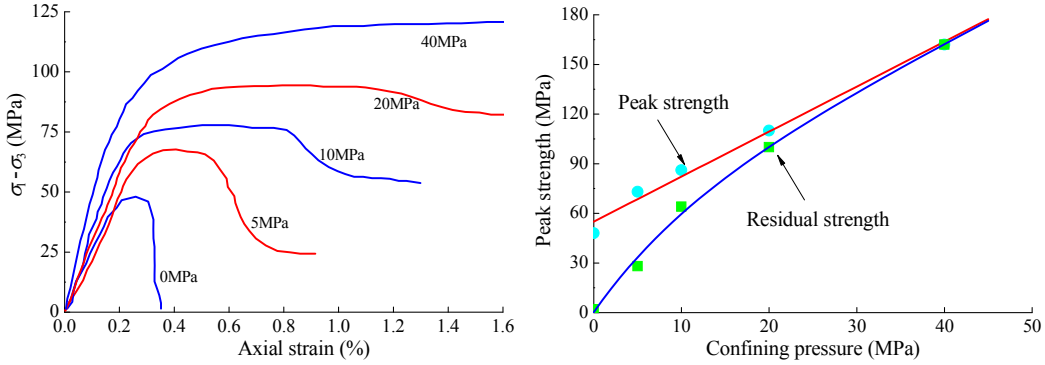

a b

Fig. 5. Fine crystal marble samples under common triaxial compression: a. Principal stress-strain curves (You 2007); b. Evolution of rock strength with confining pressure

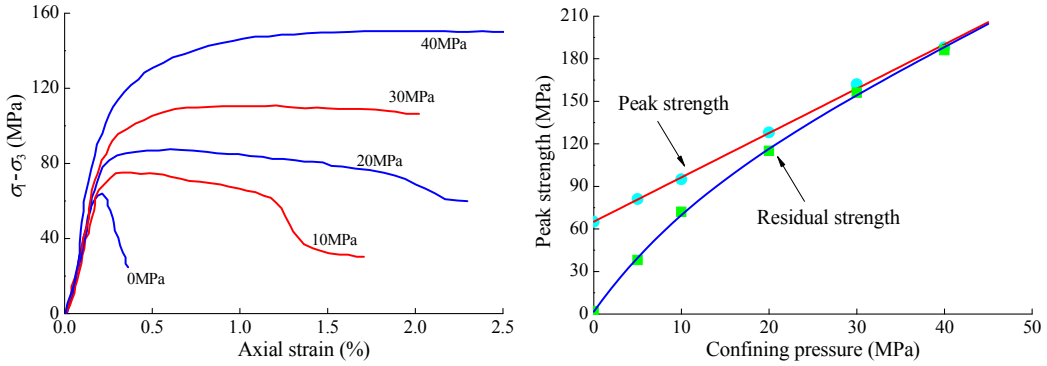

a b

Fig. 6. Medium crystal marble samples under common triaxial compression: a. Principal stress-strain curves (You 2007); b. Evolution of rock strength with confining pressure

These laboratory tests have shown that the residual strength is more sensitive to the increasing of confining pressure than the peak strength. It is necessary to establish a non-linear relationship between the confining pressure and the residual strength to develop a non-uniform strength model for rocks. With the non-uniform strength model, the deformation and failure of ground can be identified more accurately.

In order to express the non-linear behaviour of rocks, the mechanical behaviour of the basic elements must be changed under different loading conditions (Saksala et al. 2014; Li et al. 2012). In the practices of rock mechanics, the peak strength is typically described as a function of confining pressure in different forms of strength criteria (Jaeger et al.1979; Paterson 1978). However, few attempts has been progressed to describe those non-linear changes displayed in the post-peak stage in different confining conditions.

Fang and Harrison (2001) defined a strength degradation index for rock to describe the variation of strength degradation behaviour subjected to different confining pressure. The strength degradation displayed in uniaxial compression was regarded as the maximum one. The strength degradation index was expressed as the ratio between the general strength degradation and maximum strength degradation. This definition for the degradation index implied that its value ranges from 0 (no degradation associated with ductile behaviour) to 1 (complete degradation associated with brittle behaviour). However, although the laboratory experimental results suggest that rock failing under uniaxial conditions suffers maximum reduction, the strength degradation is quite

instability in different tests. Actually, the peak strength is basically stable in uniaxial conditions, while the residual strength is naturally uncertainty and not convenient to measure in the laboratory.

Alejano et al. (2009) introduced three strain softening models including constant drop modulus and constant dilatancy, variable drop modulus and constant dilatancy, variable drop modulus and variable dilatancy. The third one was considered to represent the actual behaviour of rock mass. However, the relationship of residual strength and confining pressure is still linearly dependent, which is not coincidence with the rock behaviour shown in Figs. 4-6.

Li et al. (2012) proposed a statistical damage constitutive model for rocks to reflect the phenomenon of strain softening. A practical procedure for identifying the model parameters was provided and an associated flow for solving this constitutive model was presented. In this model, the strain softening behaviour of rocks was expressed. However, the nonlinear influence of confining pressure on the residual strength was also not considered.

Saksala et al. (2014) presents a new constitutive model for rocks that exhibit either brittle or ductile behaviour. The Drucker-Prager yield function and the Modified Rankine criterion with a tension cut-off and a parabolic cap surface are used to indicate the stress states leading to strain softening/hardening and damage. A confining pressure dependent parabolic hardening-linear softening law in compression is calibrated with respect to the degradation index. The model is able to capture the brittle-to-ductile transition exhibited by many rocks under high confining pressure. The hardening behaviour of rock under extremely high confined stress states is described by the viscoplastic cap model. However, the constitutive equations in this study are limited to special cases and the results obtained are too complex to have practical applications.

The constitutive equations for rocks in previous studies are unable to express the non-linear evolution of residual strength with the confining pressure. In this study, we will present a new method to describe the strength evolution from pre-failure to residual stages considering the influence of confining pressure.

2.2.2 A modified strain-softening model

As shown above, the influence of confining pressure on the residual strength exhibits a non-linear behavior. The residual strength asymptotically approach the peak strength with the increasing of confining pressure in laboratory tests, and almost equal

when the confining pressure is large enough. According to the rock behaviour that transition from brittle strain softening to ductile failure perfect plasticity with the increasing of confining pressure, a modified strain-softening model is proposed to account for the evolution of residual strength with the confining pressure as shown in Fig. 7. In the new model, the constitution of strain-softening behavior is also approximated as three line segments, but the evolution of residual strength exhibits a non-linear behavior. In the stage before peak strength the equation is the same with the conventional strain-softening model.

A new variable is defined as equivalent peak strength $\sigma_c(\sigma_3)$ to get rid of the linear influence of confining pressure as shown in equation (3). Similarly, equivalent residual strength $\sigma_c^*(\sigma_3)$ is defined as shown in equation (4). Fig. 8a shows that both the equivalent peak strength and the equivalent residual strength are constants in the conventional model. In the new model, the equivalent peak strength $\sigma_c(\sigma_3)$ is also constant, while the equivalent residual strength $\sigma_c^*(\sigma_3)$ could be attributed to a function of confining pressure in the post-failure process as shown in Fig. 8b.

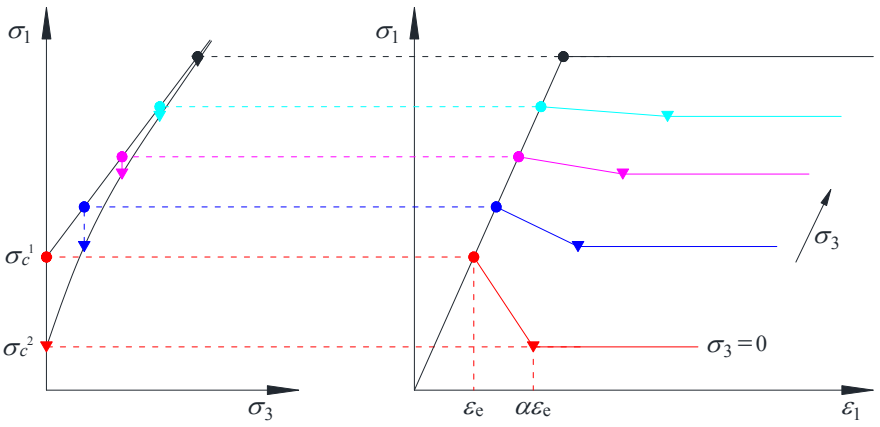

Fig. 7. A modified strain-softening model: a. evolution of strength with confining pressure, b. constitutive relation

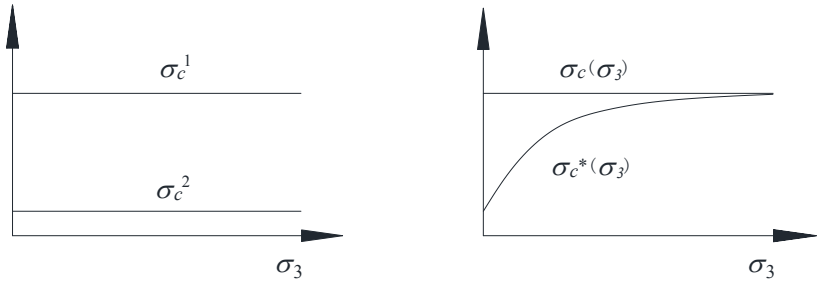

a b

Fig. 8. The equivalent residual strength of rock: a. conventional strain-softening model, b. modified strain-softening model

$$\sigma_c(\sigma_3) = \sigma_c - K_p * \sigma_3 \tag{3}$$

$$\sigma_c^*(\sigma_3) = \sigma_c^* - K_p * \sigma_3 \tag{4}$$

Where, σ_c is the peak compression strength, and σ_c^* is residual compression strength in laboratory tests. K_p is the passive coefficient, which remains unchanged within the complete plastic region. K_p and $\sigma_c(\sigma_3)$ can be obtained by linear regression based on the relation of σ_1 and σ_3 as shown in equation (5).

$$\sigma_1 = K_p * \sigma_3 + \sigma_c(\sigma_3) \tag{5}$$

Considering the influence of confining pressure on equivalent residual strength, the constitutive relations for the modified strain-softening model can be given as follows:

$$\sigma_1 = \begin{cases} K_p\sigma_3 + \left(\sigma_c(\sigma_3) + \dfrac{(\sigma_c(\sigma_3) - \sigma_c^*(\sigma_3))\varepsilon_1^{\,p}}{\alpha\varepsilon_{1e}} \right) & (0 \le \varepsilon_1^{\,p} \le \alpha\varepsilon_{1e}) \\ K_p\sigma_3 + \sigma_c^*(\sigma_3) & (\varepsilon_1^{\,p} \ge \alpha\varepsilon_{1e}) \end{cases} \tag{6}$$

In the above equations, σ_c is the compression strength, and transits gradually from $\sigma_c(\sigma_3)$ to $\sigma_c^*(\sigma_3)$, according to the evolution of the major principal plastic strain ε_1^p. Herein, the major principal plastic strain ε_1^p is employed as the softening parameter, because it is relatively simple and can be obtained easily from the results of uniaxial compression tests. K_p is the passive coefficient. The equivalent residual strength $\sigma_c^*(\sigma_3)$ will be estimated based on the laboratory test data in existing literature in next section.

2.2.3 The relationship between equivalent residual strength and confining pressure

Based on the laboratory experimental data, it is suggested that the relation between the equivalent residual strength and confining pressure may be expressed as equation (7).

$$\sigma_c^*(\sigma_3) = \sigma_c(\sigma_3) - \beta * e^{-\gamma*\sigma_3} \tag{7}$$

Where, $\sigma_c^*(\sigma_3)$ is the equivalent residual strength, σ_3 is the confining pressure, and $\sigma_c(\sigma_3)$ is equivalent peak strength. The equivalent residual strength $\sigma_c^*(\sigma_3)$ for different types of rocks can be calculated by equation (4), and $\sigma_c(\sigma_3)$ can be obtained according to equation (5). According to the definition, the values of $\sigma_c^*(\sigma_3)$ must less than $\sigma_c(\sigma_3)$ and gradually approached to it. It represents the rock behaviour transform

from brittle in unconfined conditions, through quasi brittle under moderate confining stress, to ductile at high confining stresses. β represents the difference between equivalent peak strength and equivalent residual strength when the confining pressure is equal to zero. γ is an exponential parameter, which control the transformation speed of residual strength to peak strength. β and γ will be estimated by curvilinear regression based on a series of stress-strain curves under common triaxial compression.

For example, the source data for Tennessee marble are obtained by estimating the peak and residual strengths of each stress–strain curve under different confining pressure as shown in Fig. 4. According to Eq. (4) and Eq. (5), the equivalent peak strength and equivalent residual strength for Tennessee marble are computed and tabulated in Table 1. The data for other kind of marbles, mudstone, limestone, coal and sandstone are presented in Table 2-10 and Fig. 9.

Table 1 Estimation of the equivalent residual strength of Tennessee marble (data from Brady et al. (1992))

Confining pressure	Peak strength	Residual strength	Equivalent peak strength	Equivalent residual strength
0	130	10	135.31	10.00
3.45	145	60	135.31	49.995
6.9	160	80	135.31	59.99
13.8	180	110	135.31	69.98
20.7	195	130	135.31	69.97
27.6	215	180	135.31	99.96
34.5	245	230	135.31	129.95
48.3	275	270	135.31	129.93

Table 2 Estimation of the equivalent residual strength of Marble T2b (data from Zhou et al. (2012))

Confining pressure	Peak strength	Residual strength	Equivalent peak strength	Equivalent residual strength
0	162	50	160.25	50.00
5	170	70	160.25	57.55
10	186	92	160.25	67.10

20	210	135	160.25	85.20
40	260	225	160.25	125.40

Table 3 Estimation of the equivalent residual strength of Fine crystal marble (data from You et al. (2007))

Confining pressure	Peak strength	Residual strength	Equivalent peak strength	Equivalent residual strength
0	48	2	55	2.00
5	73	28	55	14.40
10	86	64	55	36.80
20	110	100	55	45.60
40	162	162	55	53.20

Table 4 Estimation of the equivalent residual strength of Medium crystal marble (data from You et al. (2007))

Confining pressure	Peak strength	Residual strength	Equivalent peak strength	Equivalent residual strength
0	65	2	65.12	2.00
5	81	38	65.12	22.37
10	95	72	65.12	40.74
20	128	115	65.12	52.47
30	162	156	65.12	62.21
40	188	186	65.12	60.95

Table 5 Estimation of the equivalent residual strength of Coarse marble (data from Yang et al. (2008))

Confining pressure	Peak strength	Residual strength	Equivalent peak strength	Equivalent residual strength
0	68	4	74	4.00
5	90	45	74	31.00
10	108	77	74	49.00
20	131	116	74	60.00
30	155	144	74	60.00

Table 6 Estimation of the equivalent residual strength of Marble (data from Shen et al. (2014))

Confining pressure	Peak strength	Residual strength	Equivalent peak strength	Equivalent residual strength
10	102.4	65.3	85.17	41.64
20	135.8	109.5	85.17	62.18
40	188	165.7	85.17	71.07
60	224.5	216.6	85.17	74.65
70	248.3	246.3	85.17	80.69

Table 7 Estimation of the equivalent residual strength of Shanxi mudstone (data from Lu et al. (2010))

Confining pressure	Peak strength	Residual strength	Equivalent peak strength	Equivalent residual strength
0	21.1	8.9	24.45	8.90
5	31.4	18.2	24.45	12.78
10	38.1	25.7	24.45	14.86
20	47.1	35	24.45	13.32
30	54.6	48.2	24.45	15.68
40	66.5	66.5	24.45	23.14

Table 8 Estimation of the equivalent residual strength of Indiana limestone (data from Walton et al. (2015))

Confining pressure	Peak strength	Residual strength	Equivalent peak strength	Equivalent residual strength
1	67	18	63.71	14.32
2	71	22	63.71	14.65
4	78	33	63.71	18.30
6	87	60	63.71	37.95
8	93	66	63.71	36.60
10	101	75	63.71	38.24
12	107	83	63.71	38.89

Table 9 Estimation of the equivalent residual strength of Vosges sandstone (data from Besuellea et al. (2000))

Confining pressure	Peak strength	Residual strength	Equivalent peak strength	Equivalent residual strength
10	83	65	67.7	44.30
20	113	93	67.7	51.60
30	135	114	67.7	51.90
40	150	136	67.7	53.20
50	168	158	67.7	54.50

Table 10 Estimation of the equivalent residual strength of typical coal samples (data from Liu et al. (2014))

Confining pressure	Peak strength	Residual strength	Equivalent peak strength	Equivalent residual strength
0	23	1	30.71	1.00
10	62	32	30.71	5.69
20	87	63	30.71	10.37
30	114	95	30.71	16.06
40	135	116	30.71	10.74
50	158	146	30.71	14.43

The mathematical relationship of equivalent residual strength and confining pressure is fitted to negative exponential function, and the data together with the best-fit curves are shown in Fig. 9. In the case of Tennessee marble, curvilinear regression on the data listed in Table 1 shows the value of β to be 115, and the value of γ to be 0.0443. The correlation coefficient for this analyses is 0.8976. The result implies that the evolution of equivalent residual strength is a mechanical property of rock, and that different rocks may have different value for β and γ. Thus, laboratory testing will be required to determine these parameter for a specific rock.

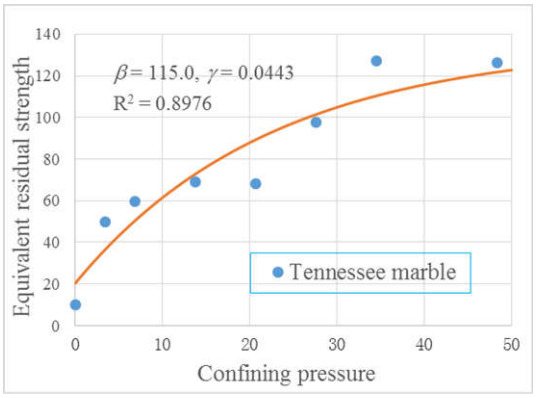
β= 115.0, γ= 0.0443
R² = 0.8976
Tennessee marble
Equivalent residual strength
Confining pressure

a

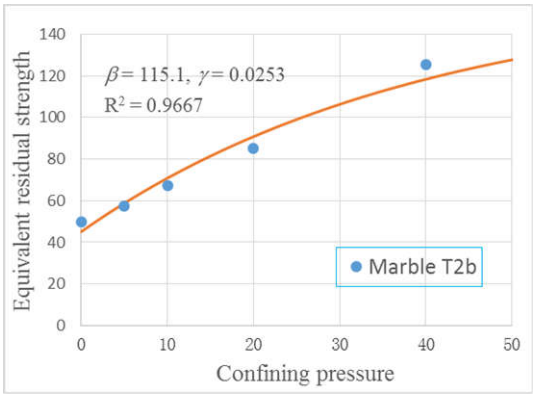
β= 115.1, γ= 0.0253
R² = 0.9667
Marble T2b
Equivalent residual strength
Confining pressure

b

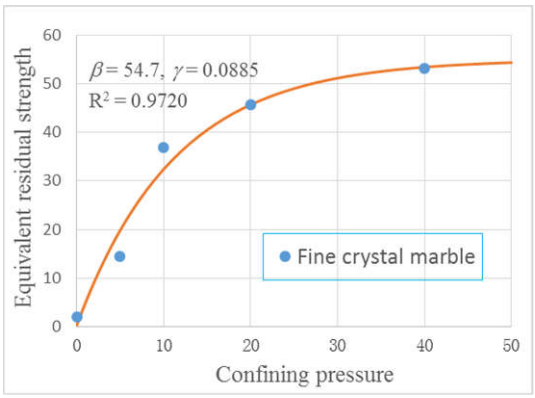
β= 54.7, γ= 0.0885
R² = 0.9720
Fine crystal marble
Equivalent residual strength
Confining pressure

c

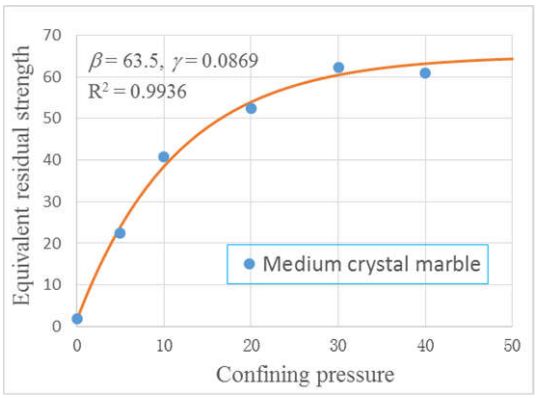
β= 63.5, γ= 0.0869
R² = 0.9936
Medium crystal marble
Equivalent residual strength
Confining pressure

d

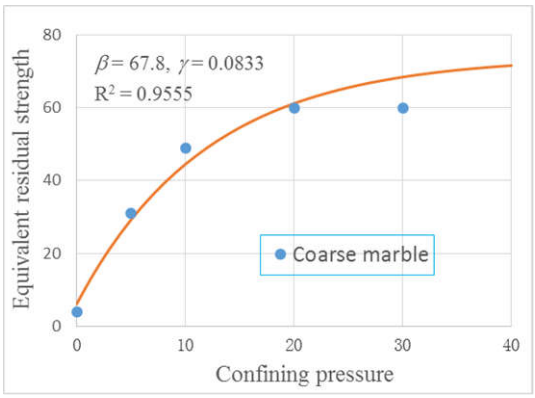
β= 67.8, γ= 0.0833
R² = 0.9555
Coarse marble
Equivalent residual strength
Confining pressure

e

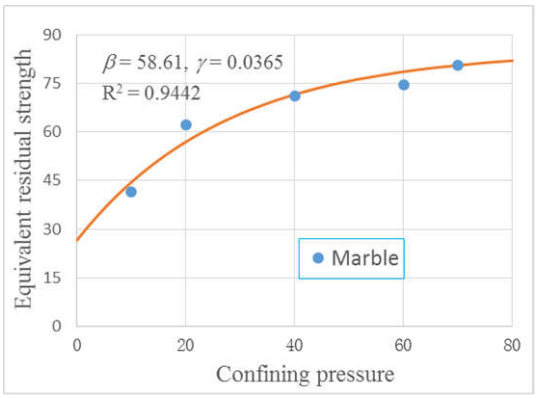
β= 58.61, γ= 0.0365
R² = 0.9442
Marble
Equivalent residual strength
Confining pressure

f

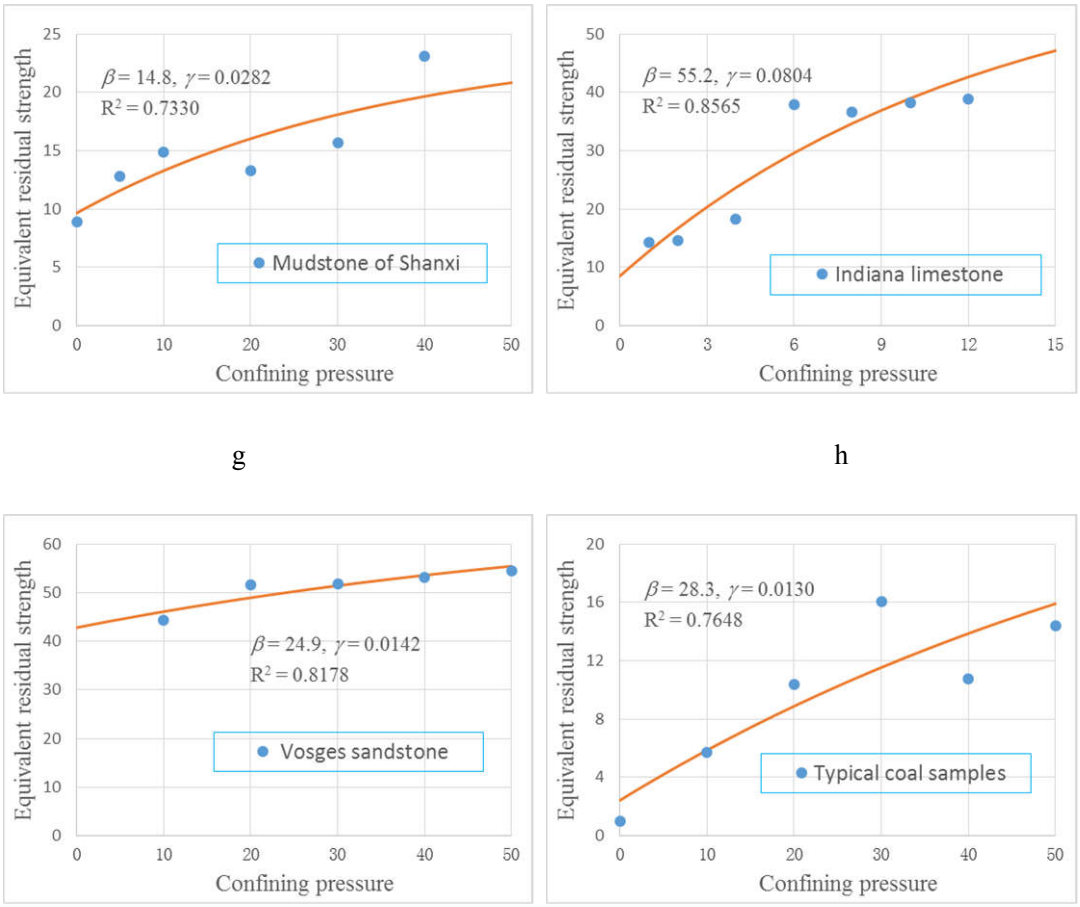

g h

i j

Fig.9. Variation of equivalent residual strength with confining stress for different rocks

The value of β, γ and correlation coefficients for different types of rock are listed in Table 11. According to the mathematical sense of equation (7), β represents the difference between equivalent peak strength and equivalent residual strength when the confining pressure is equal to zero. However, the internal instability of residual strength in uniaxial condition results that the equivalent residual strength is also inaccuracy. Therefore, the value of β can only be determined by curvilinear regression. The difference between equivalent peak strength and equivalent residual strength is just a reference of β. These results also imply that the value of γ lies between 0.01 and 0.1. The value of correlation coefficients are greater than 0.7 for all the rock samples, which indicates that the correlation between equivalent residual strength and confining pressure is very significant. In addition, the correlation coefficients are relatively higher in the case of marble than the case of mudstone, limestone, sandstone and coal. The results indicate that the relation is more remarkable for hard rock than soft rock. The

instability behaviour of soft rock could also be confirmed by the laboratory results by Indraratna (2014).

Table 11 Estimation of the equivalent residual strength of typical samples

Rock types	β	γ	R-square
Tennessee marble	115.0	0.0443	0.8976
marble T2b	115.1	0.0253	0.9667
fine crystal marble	54.7	0.0855	0.9720
medium crystal marble	63.5	0.0869	0.9936
coarse marble	67.8	0.0833	0.9555
marble	58.6	0.0365	0.9442
mudstone of Shanxi	14.8	0.0282	0.7330
Indiana limestone	55.2	0.0804	0.8565
Vosges sandstone	24.9	0.0142	0.8178
coal	28.3	0.0130	0.7648

2.3 Implementation of the new constitutive model by numerical tests

In order to verify the effective of the new constitutive model, numerical simulation is conducted to reproduce the post-failure behavior of the rock. FLAC3D is selected because of its convenience and popularity in modelling geo-mechanics problems. The new model in the numerical simulations is developed based on the strain-softening model by the Fish language in FLAC^{3D}. The transitional strength is updated according to the stress and deformation state of every element after every step. The modified strain-softening constitutive laws in FLAC^{3D} are characterized by six parameters: bulk modulus K, shear modulus G, friction angle ϕ, cohesion c, dilation angle ψ, softening parameter η and the two new parameters β and γ.

The performance of the present model is demonstrated at the material point level using a computational model of a single 8-node hexahedral element. The confining pressures are set to be 0MPa, 27.6MPa, 34.5MPa, 48.3MPa in different tests. Compressive axial loading is applied in the form of a velocity boundary condition with a constant velocity of -5×10^{-7} m/s on the upper surfaces. The material properties of Tennessee marble and model parameters given in Table 12 are used throughout simulations.

Table 12 The properties of Tennessee marble employed in the verification case

E (Pa)	ν	K_p	σ_c^1 (Pa)	σ_c^2 (Pa)	K_ψ	β	γ
6.5e10	0.2	3.0	1.38e8	2.03e7	1.33	1.15e8	0.0044

The numerical test results at different confining pressure are shown in Fig. 10. To highlight the advantages of the new model, the stress-strain curves with the conventional strain-softening model and results from the laboratory experiments are also depicted in these figures. A better agreement can be observed between numerical results with the new model and the experiment data in these figures.

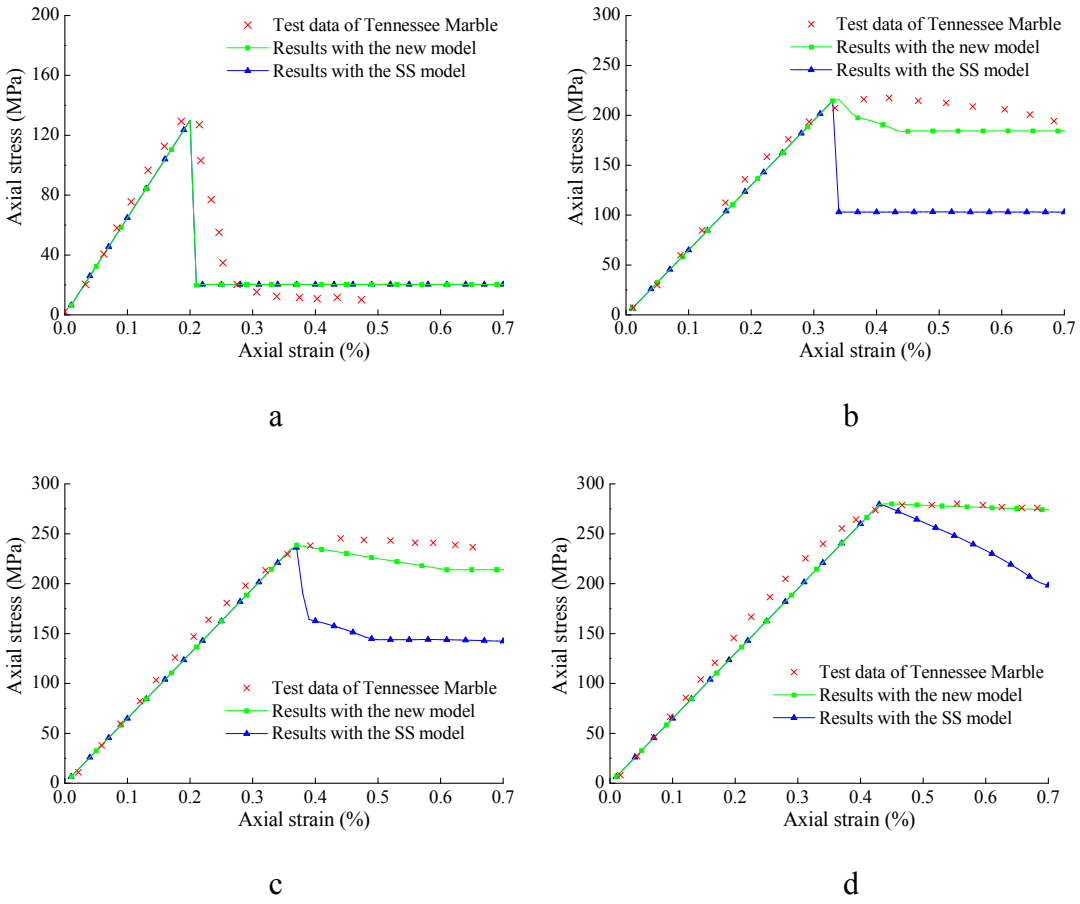

Fig. 10. Comparison between experimental and theoretical curves at different confining pressures: (a) σ_3=0 MPa; (b) σ_3=27.6 MPa; (c) σ_3=34.5 MPa; (d) σ_3=48.3 MPa.

At the condition of σ_3=0 MPa, the rock behaviour with different model are all the same, and close to the experiment data. It is reasonable as no confining pressure is applied, resulting no effect on the residual strength. With the increasing of confining pressure, the advantages of the new model becomes more and more obvious. The rock behaviour in high confining pressure conditions could also be confirmed by the

laboratory results by Li (2013).

2.4 Ground Reaction Analyses of a Circular Tunnel

2.4.1 Problem Description

The proposed model will be applied in the ground reaction analyses of a circular tunnel to reveal the influence of post-failure behavior of rock mass on the tunnel convergence. The calculation is developed from the solution for circular tunnels excavated in conventional strain-softening materials by the authors (Guan et al. 2007). The excavation of long deep tunnels with circular cross section under hydrostatic in-situ stress condition can be considered as an axial symmetry plane strain problem, while neglecting the influence of gravity, and restricting the out-of-plane principal stress as intermediate stress. After tunnel excavation, the surrounding rock mass will experience elastic, softening and residual regions sequentially. The objective is to evaluate the stress and displacement redistributions (or namely ground responses) after excavation. In addition, the geomechanics sign convention is employed, and the radial displacement towards tunnel axis is taken as positive consequently.

2.4.2 Equilibrium Equations for Rock Mass

Consider an infinitesimal volume in the radial direction as shown in Fig. 11. The rock mass is subjected to a radial stress σ_r, a tangential stress σ_t. The static equilibrium condition of the infinitesimal rock mass volume can be formulated as:

$$\sigma_r r d\omega L_z + 2\sigma_t dr L_z \sin\frac{d\omega}{2} = (\sigma_r + d\sigma_r)(r + dr) d\omega L_z \tag{8}$$

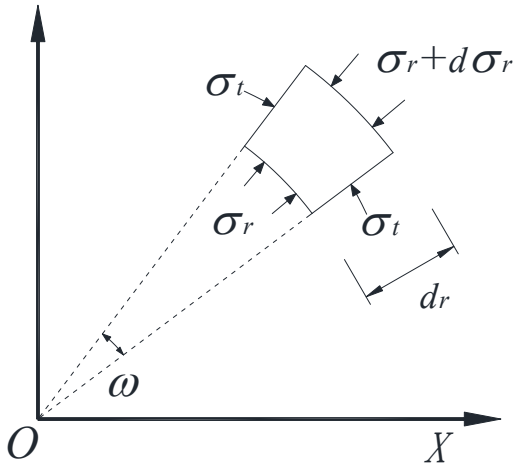

Fig. 11 Static equilibrium condition for the surrounding rock mass.

Noticing that $\sin(\frac{d\omega}{2})$ approximately equals $\frac{d\omega}{2}$ since $d\omega$ is an infinitesimal, the equilibrium equation can be deduced as:

$$\frac{d\sigma_r}{dr} = \frac{\sigma_t - \sigma_r}{r} \tag{9}$$

When applying Eq. (9) to the elastic region, where the stress state of rock mass should verify the hydrostatic in-situ stress condition that the sum of σ_r and σ_t equals $2P_0$, the equilibrium equation for elastic region can be formulated as:

$$\frac{d\sigma_r}{dr} = \frac{2P_0 - 2\sigma_r}{r} \tag{10}$$

When applying it to the plastic region, where the stress state of rock mass should verify the failure criterion as shown in Eq. (6), the equilibrium equation for the plastic region can be formulated as:

$$\frac{d\sigma_r}{dr} = \frac{(K_p - 1)\sigma_r + \sigma_c}{r} \tag{11}$$

Where, σ_c is a dynamic value which is always changing with the major principal plastic strain ε_1^p as shown below:

$$\sigma_c = \begin{cases} \sigma_c(\sigma_3) + \dfrac{(\sigma_c(\sigma_3) - \sigma_c^*(\sigma_3))\varepsilon_1^{\,p}}{\alpha\varepsilon_{1e}} & (0 \le \varepsilon_1^{\,p} \le \alpha\varepsilon_{1e}) \\ \sigma_c^*(\sigma_3) & (\varepsilon_1^{\,p} \ge \alpha\varepsilon_{1e}) \end{cases} \tag{12}$$

2.4.3 Displacement Compatibility Equations for Rock Mass

Due to the plane strain axial symmetry assumption, the strain-displacement relationships for the rock mass can be simplified significantly as:

$$\frac{du}{dr} = \varepsilon_r \quad \frac{u}{r} = \varepsilon_t \tag{13}$$

In the elastic region, according to Hook's law, the tangential strain of the rock mass can be evaluated from its stress state, as formulated in Eq. (14), where E and ν are the Young's modulus and the Poisson ratio of the rock mass.

$$\varepsilon_t = (\frac{\sigma_t}{E} - \nu\frac{\sigma_r}{E} - \nu\frac{2P_0\nu}{E}) - (\frac{P_0}{E} - \nu\frac{P_0}{E} - \nu\frac{2P_0\nu}{E}) \tag{14}$$

Notice that only the strain caused by tunnel excavation is concerned, which means

the initial strain due to in-situ stresses should be removed. Then, associating these two equations and considering the hydrostatic in-situ stress condition, the displacement compatibility equation for the elastic region can be formulated as Eq. (15).

$$u = r\varepsilon_t = \frac{P_0 - \sigma_r}{E}(1+\nu)r \tag{15}$$

For the plastic region, the loading path for this problem refers to a monotonic decrease of the fictitious inner pressure, corresponding to the advancing of the tunnel face. Consequently, the rates of all mechanical variables can be evaluated by their first-order derivatives with respect to P_i. The incremental theory of plasticity (Graziani et al. 2005) assumes that the total strain rate consists of both elastic part and plastic part, as shown in Eq. (16). The elastic part is controlled by Hooke's law and the plastic part by the potential flow rule, as formulated by Eqs. (17) and (18), respectively. The relationship between the strain rate and the displacement velocity is simplified by virtue of axial symmetry and formulated by Eq. (19).

$$\dot{\varepsilon}_r = \dot{\varepsilon}_r^{\,e} + \dot{\varepsilon}_r^{\,p}, \qquad \dot{\varepsilon}_\theta = \dot{\varepsilon}_\theta^{\,e} + \dot{\varepsilon}_\theta^{\,p} \tag{16}$$

$$\dot{\varepsilon}_r^{\,e} = \frac{1-\nu}{2G}\dot{\sigma}_r - \frac{\nu}{2G}\dot{\sigma}_\theta, \quad \dot{\varepsilon}_\theta^{\,e} = \frac{1-\nu}{2G}\dot{\sigma}_\theta - \frac{\nu}{2G}\dot{\sigma}_r \tag{17}$$

$$\dot{\varepsilon}_r^{\,p} = \lambda\frac{\partial g}{\partial \sigma_r} = \lambda, \quad \dot{\varepsilon}_\theta^{\,p} = \lambda\frac{\partial g}{\partial \sigma_\theta} = -\lambda K_\psi \tag{18}$$

$$\dot{\varepsilon}_r = \frac{\partial \dot{u}}{\partial r}, \quad \dot{\varepsilon}_\theta = \frac{\dot{u}}{r} \tag{19}$$

Here, g is the plastic potential. The rates of all mechanical variables (denoted by a dot mark) are referred as their first-order derivatives with respect to P_i. Then associating these four equations, eliminating the multiplier λ, the displacement compatibility equation for the plastic region can be expressed as:

$$\frac{\partial \dot{u}}{\partial r} + K_\psi\frac{\dot{u}}{r} = \frac{(1-\nu-\nu K_\psi)}{2G}\dot{\sigma}_r - \frac{(\nu K_\psi - K_\psi + \nu)}{2G}\dot{\sigma}_\theta \tag{20}$$

2.4.4 Semi-analytical Solution

The displacement compatibility equation and the equilibrium equation (together with the failure criterion) can only be solved by numerical methods. The fourth Runge-Kutta method is employed, and a two dimensional finite difference algorithm (i.e. along the unloading path and along the radial direction) is programed as shown in Fig. 12. All the variables describing the state of the surrounding rock mass have two indices: the first indicates a certain stage in the unloading path and the second indicates a certain position in the radial direction. Supposing that at former stage (say the $(k\text{-}1)^{th}$ stage where $P_i=P_i^{(k-1)}$), all the mechanical states of the rock mass are known, the objective is to evaluate all the mechanical states at current stage (i.e. the k^{th} stage where $P_i=P_i^{(k)}$) according to their known counterparts at the former stage, which includes the following three steps: stress evaluation, displacement evaluation and transitional strength update. After one iteration finishes, these known mechanical states at the current stage can be used to evaluate the mechanical states at next stage (i.e. the $(k+1)^{th}$ stage where $P_i=P_i^{(k+1)}$), following the same three steps. This kind of iteration is repeated until the final stage where $P_i=P_i^{fin}$.

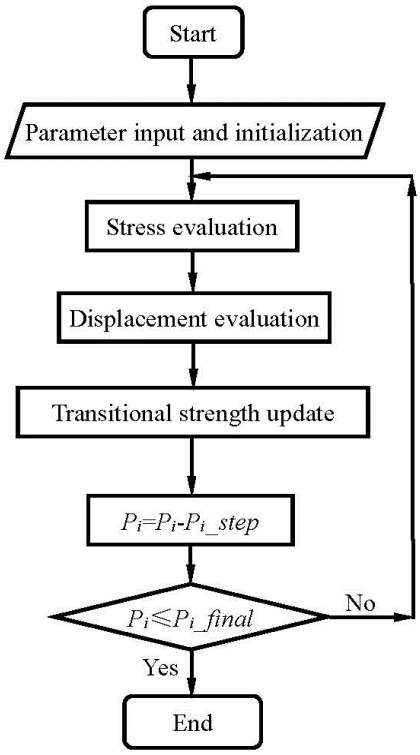

Fig. 12 Calculation flow diagram

(1) *Stress Evaluation of Rock Mass*

The equilibrium equations (10) and (11) are solved by the fourth-order Runge-Kutta method (Basheer 2000). At the current stage, the radial stress at the tunnel wall $\sigma_r(k, R_a)$ is known and equals to $P_i^{(k)}$, which serves as the boundary condition of the equilibrium equations. According to Eq. (11) and the failure criterion, the radial and tangential stresses can be obtained by Runge-Kutta method. When the radial stress increases up to the critical inner pressure P_i^{cri}, record the position as the radius of the elasto-plastic interface R_e, then go on evaluating the stress state of elastic region. According to the research of Carranza-Torres (1999), σ_{re} is a constant that only depends on the properties of rock mass itself and independent of the position of the elasto-plastic interface. The critical inner pressure can be calculated by the following formula.

$$P_i^{cri} = \sigma_{re} = \frac{2P_0 - \sigma_c(\sigma_3)}{K_p + 1} \tag{21}$$

The radial and tangential stresses at the current stage can be determined after the stress evaluation process.

(2) *Displacement Evaluation of Rock Mass*

For the elastic region, the radial displacement of the rock mass at the current stage can be evaluated directly by the radial stress of rock mass at the current stage, according to Eq. (15). For the plastic region, the radial and tangential stress rates $\dot{\sigma}_r(k,r)$ and $\dot{\sigma}_t(k,r)$ should be first evaluated by their first-order difference with respect to P_i, as shown in Eq. (22).

$$\dot{\sigma}(k,r) = \frac{\sigma(k,r) - \sigma(k-1,r)}{dP_i} \quad (r \le R_e) \tag{22}$$

Similarly, the deformation rate at the elasto-plastic interface $\dot{u}(k, R_e)$, which serves as the boundary condition of the compatibility equation, can also be obtained by its first-order difference with respect to P_i. Then the fourth-order Runge-Kutta method is utilized again to evaluate the deformation rate at each sequential calculation point (inward radial direction) according to the compatibility equations (20). Finally, the displacement at the current stage can be obtained by accumulating the displacement increment at the current stage to its counterpart at the former stage.

$$u(k,r) = u(k-1,r) + \dot{u}(k,r)dP_i \quad (r \le R_e) \tag{23}$$

The displacement and the stresses at the former stage, as well as the stresses at the current stage, are required during this step. Then the displacement at the current stage can be determined after the displacement evaluation process.

(3) *Transitional Strength Update of Rock Mass*

After the displacement evaluation, the major principle plastic strain ε_t^p at the current stage, which serves as the softening parameter herein, can be evaluated by Eq. (24). Then the transitional strength at the current stage can be computed via Eq. (6) and Eq. (7).

$$\varepsilon_t^p(k,r) = \varepsilon_t(k,r) - \varepsilon_{te}(k,r) = \frac{u(k,r)}{r} - \frac{u(k,R_e)}{R_e} \quad (r \le R_e) \tag{24}$$

The displacements and the tangential stresses at the current stage are required in this step, and the transitional strength of rock mass at the current stage can be determined.

After these three steps, all the mechanical states at the current stage are known, which can be used to evaluate their counterparts at next stage (i.e. the $(k+1)^{th}$ stage where $P_i=P_i^{(k+1)}$).

2.5 Application and Verification of the New Model

The proposed method is programmed in VB development environment, and verified by numerical simulations. An illustrative case study is presented in this section to demonstrate the influence of post-failure behavior of rocks in conventional tunnelling.

Suppose that a circular tunnel with a design radius of 5.0 m is excavated under a hydrostatic in-situ stress of 10 MPa (about 500 m rock mass covering above). The properties of the rock mass employed are listed in Table 13.

The ground responses after excavation in the analytical solution (including the distribution of stress, displacement, principal plastic strain, and transitional strength) are shown in Figs. 13-15 (represented by solid lines, Analytical_New). To highlight the influence of the different constitutive model, the ground responses with the ideal elasto-plastic model (Analytical_Ideal) and the strain-softening model (Analytical_SS) are also calculated and depicted in these figures.

The analytical results show that the plastic region and the displacement from the new model falls between the ideal elasto-plastic model and the strain-softening model. The post-peak strength is consistent with the peak strength in the ideal elasto-plastic model, which obviously doesn't fit with the actual behaviors of rock materials. For the new model, the plastic region and the displacement is smaller than the strain-softening model due to the increasing of post-peak strength. In this case study, the difference of the maximum displacements is about 5%. Although the value is not very large compared with the actual error between the theoretical results and measured data, eliminating the system errors is a meaningful work. The influence rules of various parameters on the deformation and failure of rock mass will be revealed in the following parameters analysis.

As shown in Fig. 16, the equivalent transitional strength in the elastic region is constant, and no softening appears. The equivalent transitional strength distributions in the surrounding rock mass is influenced by the confining pressure and the principal plastic strain in the plastic region. The plastic region is divided into residual region and softening region according to the principal plastic strain. In the residual region, the equivalent transitional strength is constant in the strain-softening model. While, the equivalent transitional strength increase with the increasing of confining pressure (σ_r) in the modified strain-softening model, indicating that the strength evolution characteristic of the rock mass is well expressed. The proposed model can elucidate the deformation and failure characteristics of rock mass in tunnelling more rationally.

The validity of analytical method is verified by numerical simulations (codes: FLAC^{3D}). The new model in the numerical simulations is developed based on the strain-softening model by the Fish language in FLAC^{3D}. The transitional strength is updated according to the stress and deformation state of every element after every step. The results from the numerical simulations are depicted in Figs. 13-15, as denoted by triangle, cross and circle marks for three different models respectively. As shown in these figures, the ground responses computed by the analytical method and by the numerical simulations fit each other exactly for the most part, indicating that the semi-analytical solutions for the new model in the circular tunnel is valid.

Table 13 The properties of rock mass employed in the verification case

E /Pa	ν	K_p	K_ψ	$\sigma_c(0)$/Pa	$\sigma_c^*(0)$ /Pa	α	β	γ
1e9	0.25	3.0	1.33	5e6	3e6	0.0025	2e6	0.1

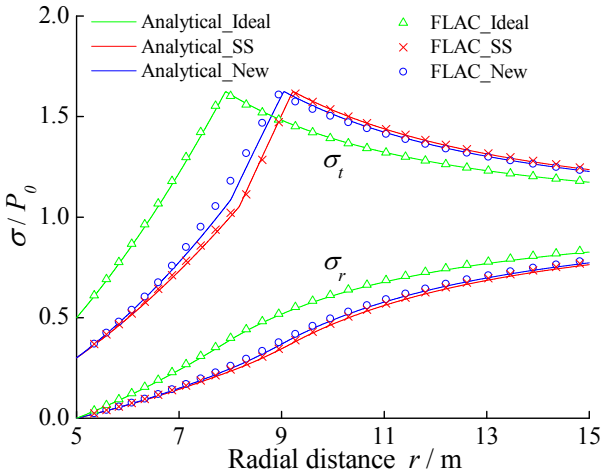

Fig. 13 The stress distributions in the surrounding rock mass

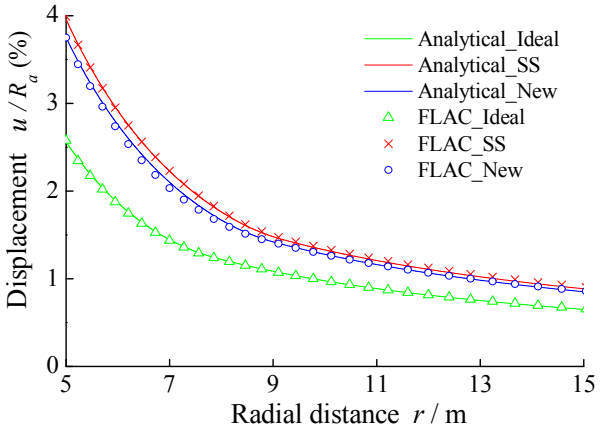

Fig. 14 The displacement distributions in the surrounding rock mass

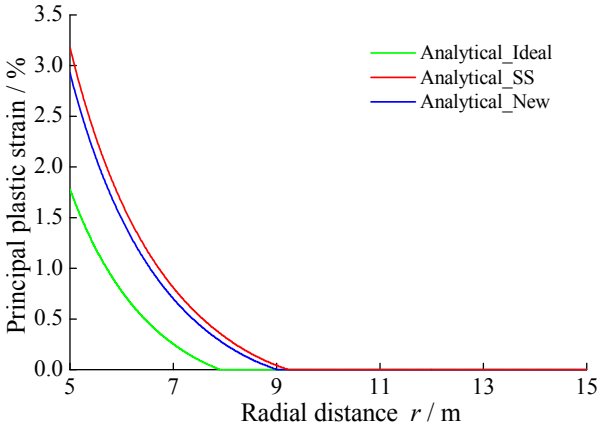

Fig. 15 The principal plastic strain distributions in the surrounding rock mass

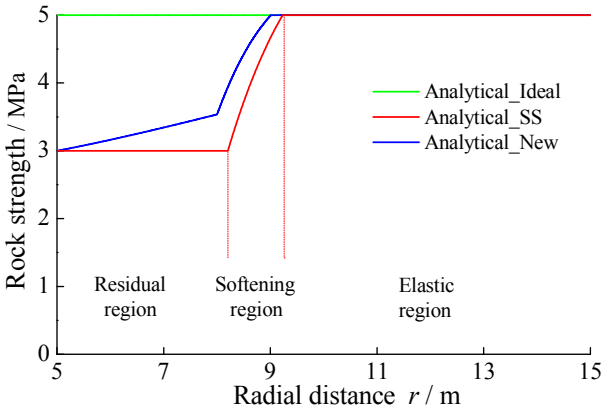

Fig. 16 The transitional strength distributions in the surrounding rock mass

2.6 Parameters Analysis

Parameters analysis are conducted to study the influence of the parameters in the new model quantitatively. The studied parameters included the equivalent peak strength $\sigma_c(0)$, the equivalent residual strength $\sigma_c^*(0)$ and the exponential factor γ. Taking the illustrative case above as a standard one and varying a single parameter, the relative significance of different parameters on the deformation and failure characteristics of rock mass is illustrated.

The tunnel convergence is selected as the estimation index in this study. The error between the results of strain-softening model and the new model is defined as Eq. (25), which physically stands for the ratios of tunnel convergence.

$$err_{\max} = \frac{u_{SS} - u_{New}}{u_{SS}} \tag{25}$$

Where, u_{ss} is the maximum tunnel convergence with strain-softening model, u_{New} is the maximum tunnel convergence with the new model.

2.6.1 The Influence of Equivalent Peak Strength

The equivalent peak strength of rock mass is selected to study its influence on the tunnel convergence. As the equivalent residual strength is 3MPa in the standard case, the equivalent peak strength is set from 3MPa to 17MPa in the following examples. Meanwhile, the other parameters are same with the standard case.

The evolution of the maximum displacement with the increasing of equivalent peak strength is shown in Fig. 17. To highlight the difference, the result of the strain-softening model and the $err_{\max}$ are also calculated and depicted in this figure. In

the strain-softening model, the peak strength σ_c^1 and the residual strength σ_c^2 are considered to be equal to the equivalent peak strength $\sigma_c(0)$ and the equivalent residual strength $\sigma_c^*(0)$, respectively.

The results show that the maximum displacement in both models decreases gradually with the increasing of equivalent peak strength. The $err_{\max}$ increases first and then decreases, and reach the maximum value at the stage of 8 MPa. These behaviors are reasonable and comprehensible. When the equivalent peak strength is very low, the difference between the equivalent peak strength and the equivalent residual strength is very small, certainly resulting in small $err_{\max}$ value. When the equivalent peak strength is very high, the plastic zone is very small. So the influence of post peak behaviors decreases, which also results in small $err_{\max}$ value. The displacement distribution of some typical cases in the surrounding rock mass are shown in Fig. 18. This figure shows that the displacement difference between the two models mainly located in the plastic zone.

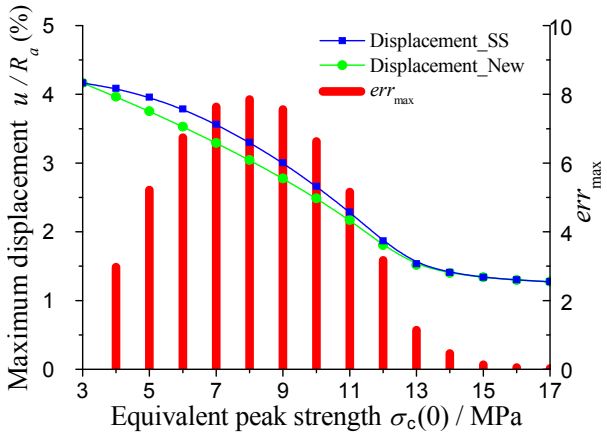

Fig. 17 The evolution of the maximum displacement and the error with the increasing of equivalent peak strength

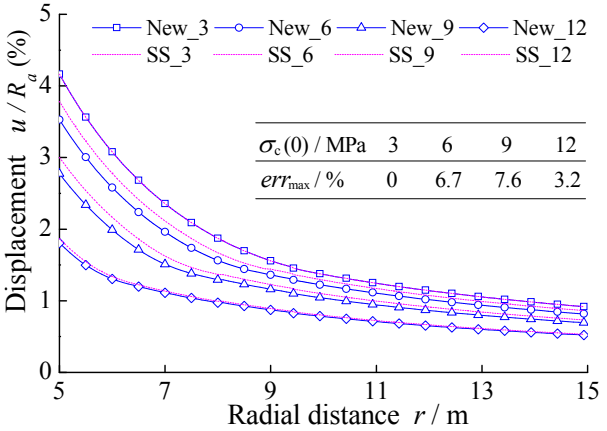

Fig. 18 The displacement distribution of some typical cases in the surrounding rock mass

2.6.2 The Influence of Equivalent Residual Strength

The influence of equivalent peak strength is studied in this part. As the equivalent peak strength is 5MPa in the standard case, the equivalent residual strength is set from 0MPa to 5MPa in the following examples. The other parameters are also same with the standard case. The evolution of the maximum displacement and the err_{max} with the increasing of equivalent residual strength are shown in Fig. 19.

The results show that the maximum displacement decreases sharply with the increasing of equivalent residual strength. The err_{max} also increases first and then decreases, and reach the maximum value at the stage of 1 MPa. When the equivalent residual strength is close to the equivalent peak strength (5MPa), the small difference also results in small err_{max} value. However, when the equivalent residual strength is small (between 0MPa and 1MPa), meanwhile the difference is very large, the err_{max} also became smaller. This behaviour is rooted from the small value of confining pressure in small equivalent residual strength case as shown in Fig. 20. The displacement distribution of some typical cases in the surrounding rock mass are shown in Fig. 21.

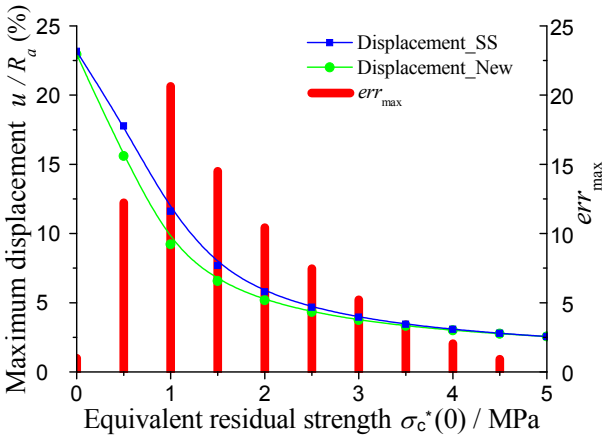

Fig. 19 The evolution of the maximum displacement and the error with the increasing of equivalent residual strength

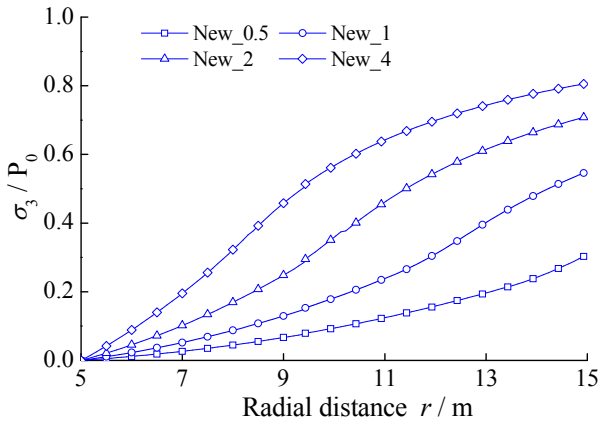

Fig. 20 The confining pressure distributions in the surrounding rock mass

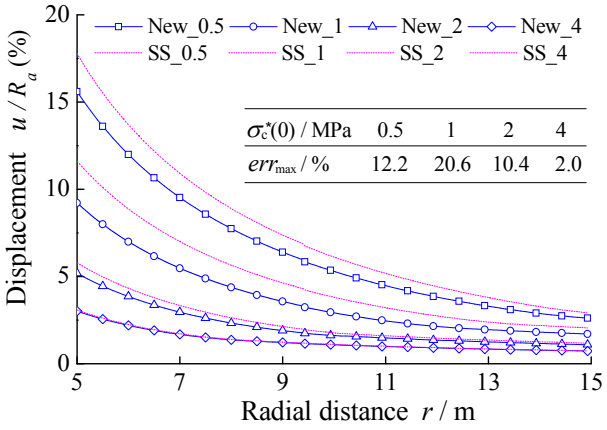

Fig. 21 The displacement distribution of some typical cases in the surrounding rock mass

2.6.3 The Influence of Exponential Factor

The influence of exponential factor is studied in this part. It is set from 0.01 to 10 in the following examples. The other parameters are also same with the standard case. The evolution of the maximum displacement and the err_{max} with the increasing of equivalent residual strength are shown in Fig. 22. The result of ideal elasto-plastic model and strain-softening model are also depicted in this figure.

The results show that the maximum displacement from the new model decreases gradually with the increasing of exponential factor. The error between the results of strain-softening model and the new model err_{max} increases monotonously. There is a clearly trend that the maximum displacement from the new model gradually approaching the ideal elasto-plastic model from the strain-softening model with the increasing of exponential factor. This behaviour can also be seen in Fig. 23. This

behaviour can be explained by the distribution of equivalent residual strength with different value of exponential factor as shown in Fig. 24. The essential difference of the new model and the ideal elasto-plastic model, the strain-softening model is herein revealed.

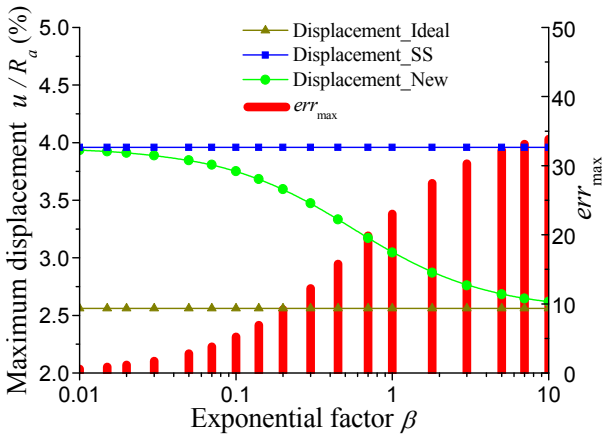

Fig. 22 The evolution of the maximum displacement and the error with the increasing of exponential factor

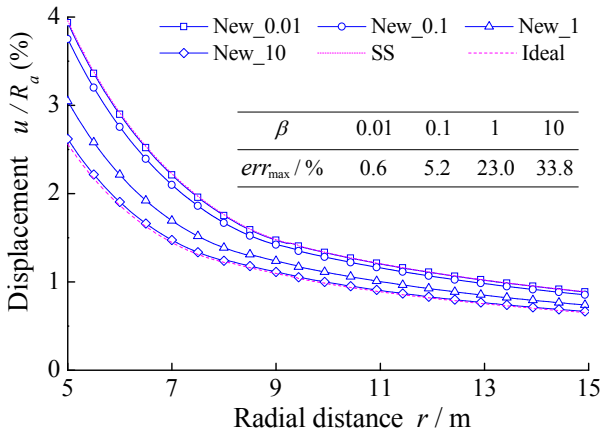

Fig. 23 The displacement distribution of some typical cases in the surrounding rock mass

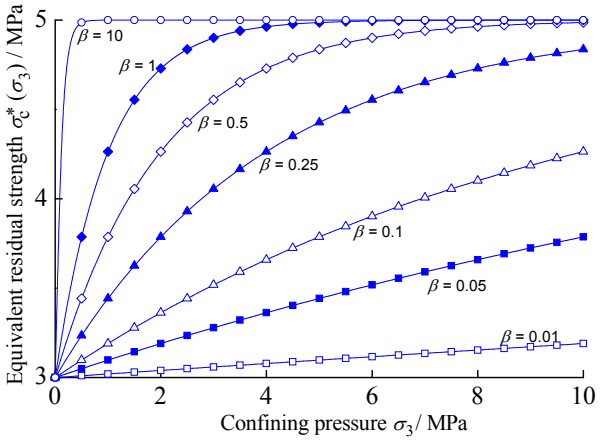

Fig. 24 The distribution of equivalent residual strength with different value of exponential factor

The results above show that the post-peak behaviour of rock mass influence the tunnel convergence dramatically. According to parameter studies, the error between the results of strain-softening model and the new model is estimated to range from 0% to 35% in common conditions.

2.7 Conclusions

A modified strain-softening model is proposed to account for the non-linear evolution of residual strength of rock mass under the influence of confining pressure. The new model for rocks can realize the gradually transition from strain-softening features to idealized elastoplastic with the increasing of confining pressure.

In the new model, equivalent residual strength is defined to describe the actual behaviour of rocks. Based on the laboratory experimental data, the relation between the equivalent residual strength and confining pressure is attributed to a negative exponential function. The parameters are estimated by curvilinear regression based on a series of stress-strain curves under common triaxial compression. The value of correlation coefficients are greater than 0.7 for all the rock samples, which indicated that the correlation between equivalent residual strength and confining pressure is very significant. In order to verify the new constitutive model, numerical simulation is conducted to reproduce the post-failure behavior of the rock. A better agreement can be observed with the new model than the conventional model in the numerical results, especially in the high confining pressure conditions.

Based on the plane strain axial symmetry assumption and the incremental theory of plasticity, equilibrium equations and compatibility equations of rock mass around a

circular tunnel is deduced theoretically. The equations are programmed in the Visual Basic development environment, and a semi-analytical solution is achieved. The influence of post-failure behavior of rocks is demonstrated through an illustrative case study. The distribution of stress, displacement, principal plastic strain and transitional strength around the circular tunnel are presented, and the discrepancy with the idealized elastoplastic model, the strain-softening model and the new model is estimated quantitatively. In addition, the validity of proposed method is verified by numerical simulations.

Parameters analysis shows that the post-peak behaviour of rock mass influence the tunnel convergence dramatically. According to parameter studies, the error between the results of strain-softening model and the new model is estimated to range from 0% to 35% in common conditions. The post-failure behavior is extremely important as the rock around an excavation is basically in post-peak state in most cases.

Reference

Alonso1 E, Alejano LR, Varas F et al (2003). Ground response curves for rock masses exhibiting strain-softening behaviour. Int J Numer Anal Meth Geomech 27: 1153-1185

Alejano LR, Rodriguez DA, Alonso E, Fdez MG (2009) Ground reaction curves for tunnels excavated in different quality rock masses showing several types of post-failure behaviour. Tunn Undergr Sp Technol 24: 689-705

Alejano LR, Alonso E, Rodriguez DA, Fernandez MG (2010) Application of the convergence-confinement method to tunnels in rock masses exhibiting Hoek-Brown strain-softening behaviour. Int J Rock Mech Min Sci 47: 150-160

Anagnostou G (1993) A model for swelling rock in tunnelling. Rock Mech Rock Eng 26(4): 07-331

Basheer I, Hajmeer M (2000) Artificial neural network: fundamentals, computing, design and application. J Microbiological Methods 43(1): 3-31

Besuellea P, Desruesb J, Raynaud S (2000) Experimental characterisation of the localisation phenomenon inside a Vosges sandstone in a triaxial cell. Int J Rock Mech Min Sci 37: 1223-37

Brady BHG, Brown ET (1992) Rock mechanics for underground mining, 2nd ed. London: Chapman & Hall, 571.

Brown E, Bray J, Landayi B, Hoek E (1983) Ground response curves for rock tunnels. J

Geotech Eng ASCE 109 (1): 15-39

Carranza TC, Fairhurst C (1999) The elasto-plastic response of underground excavations in rock masses that satisfy the Hoek-Brown failure criterion. Int J Rock Mech Min Sci 36(6): 777-809

Carranza TC, Fairhurst C (2000) Application of convergence-confinement method of tunnel design to rock masses that satisfy the Hoek-Brown failure criterion. Tunn Undergr Sp Technol 15(2): 187-213

Detournay E (1986) Elastoplastic model of a deep tunnel for a rock with variable dilatancy. Rock Mech Rock Eng 19(1): 99-108

Fang Z, Harrison JP (2001) A mechanical reduction index for rock. Int J Rock Mech Min Sci 38(8): 1193-1199

Graziani A, Boldini D, Ribacchi R (2005) Practical estimate of deformations and stress relief factors for deep tunnels supported by shotcrete. Rock Mech Rock Eng 38(5): 345-372

Guan Z, Jiang Y, and Tanabasi Y (2007) Ground reaction analyses in conventional tunneling excavation. Tunn Undergr Sp Technol 22(2): 230-237

Hao XJ, Feng XT, Yang CX, Jiang Q, Li SJ (2016) Analysis of EDZ development of columnar jointed rock mass in the Baihetan diversion tunnel. Rock Mech Rock Eng 49:1289–1312

Hasanpour R, Rostami J, Barla G (2015) Impact of advance rate on entrapment risk of a double-shielded TBM in squeezing ground. Rock Mech Rock Eng 48: 1115-1130

Indraratna B, Nimbalkar S, Coop M, Sloan SW (2014) A constitutive model for coal-fouled ballast capturing the effects of particle degradation. Comput Geotech 61: 96-107

Jaeger JC, Cook NGW. Fundamentals of rock mechanics, 3rd ed. London: Chapman and Hall, 1979. p. 593

Jiang H, Zhao J (2015) A Simple Three-dimensional Failure Criterion for Rocks Based on the Hoek–Brown Criterion. Rock Mech Rock Eng 48: 1807–1819

Jiang Y, Yoneda H, Tanabashi Y (2001) Theoretical estimation of loosening pressure on tunnels in soft rocks. Tunn Undergr Sp Technol 16(2): 99-105

Joseph T G. Estimation of the post-failure stiffness of rock. Alberta: University of Alberta, 2000

Kaiser PK, Kim BH (2015) Characterization of Strength of Intact Brittle Rock

Considering Confinement-Dependent Failure Processes. Rock Mech Rock Eng 48:107-119

Kolymbas D (2005) Tunnelling and Tunnel Mechanics: A Rational Approach to Tunneling. Springer

Lee, Y.-K., Pietruszczak, S., 2008. A new numerical procedure for elasto-plastic analysis of a circular opening excavated in a strain-softening rock mass. Tunn Undergr Sp Technol 23, 588-599

Li W, Li S, Feng X (2011) Study of post-peak strain softening mechanical properties of rock based on Mohr-Coulomb criterion. Chin J Rock Mech Eng 30(7): 1460-1466 (in Chinese)

Li X, Cao W, Su Y (2012) A statistical damage constitutive model for softening behavior of rocks, Eng Geol 143-144: 1-17

Li Y, Song Y, Liu W, Yu F, Wang R (2013) A new strength criterion and constitutive model of gas hydrate-bearing sediments under high confining pressures. J Petrol Sci Eng 109: 45-50

Liu Q, Liu K, Zhu J, Lu X (2014) Study of mechanical properties of raw coal under high stress with triaxial compression. Chin J Rock Mech Eng 33(1): 24-34

Lu Y, Wang L, Yang F (2010) Post-peak strain softening mechanical properties of weak rock. Chin J Rock Mech Eng 29(3): 640-648

Omid P, Mahdi S (2014) Development of an elasto-plastic constitutive model for intact rocks. Int J Rock Mech Min Sci 66: 1-12

Paterson MS. Experimental rock deformation: the brittle field. Berlin: Springer, 1978. p. 254

Saksala T, Ibrahimbegovic A (2014) Anisotropic viscodamage-viscoplastic consistency constitutive model with a parabolic cap for rocks with brittle and ductile behaviour. Int J Rock Mech Min Sci 70: 460-473

Shen H, Wang S, Liu Q (2014) Simulation of constitutive curves for strain-softening rock in triaxial compression. Rock Soil Mech 35(6): 1647-1654 (in Chinese)

Tiwari RP, Rao KS (2006) Post failure behaviour of a rock mass under the influence of triaxial and true triaxial confinement. Eng Geol 84: 112-129

Tutluoğlu L, Öge İF, Karpuz C (2015) Relationship between pre-failure and post-failure mechanical properties of rock material of different origin. Rock Mech Rock Eng 48: 121-141

Varas F, Alonso E, Alejano L, Fdez-Manin G (2005) Study of bifurcation in problem of unloading a circular excavation in a strain-softening material. Tunn Undergr Sp Technol 20(4): 311-322

Walton G, Arzua J, Alejano LR, Diederichs MS (2015) A laboratory-testing-based study on the strength, deformability, and dilatancy of carbonate rocks at low confinement. Rock Mech Rock Eng 48(3): 941-958

Yang SQ, Jiang YZ, Xu WY, Chen XQ (2008) Experimental investigation on strength and failure behavior of pre-cracked marble under conventional triaxial compression. Int J Solids Struct 45: 4796-4819

You M, Su C, Gou Y (2007) Experimental study on strength and deformation properties of hollow cylindrical specimens of marbles. Chin J Rock Mech Eng 26(12): 2420-2429

Zhang Q, Jiang B, Wang S, Ge X, Zhang H (2012) Elasto-plastic analysis of a circular opening in strain-softening rock mass. Int J Rock Mech Min Sci 50: 38-46

Zhou H, Yang F, Zhang C, Xu R, Zhang K (2012) An elastoplastic coupling mechanical model for marble considering confining pressure effect. Chin J Rock Mech Eng 31(12): 2389-2399

3 Influence of confining-dependent young's modulus on the convergence of underground excavation

3.1 Introduction

In engineering practice, the analytical and numerical methods are inevitably required to estimate the stress and deformation of surrounding rock mass and to help the design of support system (Brown et al., 1983; Jiang et al., 2001; Alonsol et al., 2003; Guan et al., 2007; Li et al., 2008; Zhang et al., 2015). However, the actual convergence of fractured rock mass and the soft rock is sometimes largely different with the theoretical results (Guan et al., 2007; Li et al., 2008). The non-uniform distribution of Young's modulus is considered as an important incentive (Nawrocki et al., 1995; Hsieh et al., 2007; Cai et al., 2015). Accurate rock parameters, especially the Young's modulus, are indispensable for the convergence and stability evaluation by analytical and numerical methods.

Numerous papers were contributed to the determination of Young's modulus of rocks during the past several decades (Palmstrom et al., 2001; You et al., 2003; Isik et al., 2008; Géraldine et al., 2011; Bahar et al., 2012; Kodama et al., 2013; Agan et al., 2014; Tinoco et al., 2014; Guo et al., 2015; Li et al., 2016; Domede et al., 2017). Some of them were focused on the relationship of the Young's modulus and the uniaxial compressive strength (UCS), rock mass rating (RMR) and geological strength index (GSI) for different type of rocks (Leite et al., 2001; Gokceoglua et al., 2003; Kayabasi et al., 2003; Karakus et al., 2005; Hoek et al., 2006; Asghar et al., 2014; Feng et al., 2014). Some other works were concentrated on the influence of confining pressure on the Young's modulus, and some empirical equations were obtained (You et al., 2003; Arslan et al., 2008; Wang et al., 2009; Cai et al., 2015; Yang et al., 2016). However, the attempt to describe the exact influence of the confining-dependent Young's modulus of rock mass in the ground reaction analyses is quite few. Zhang et al (2012) first obtained a closed-form solution for circular openings modeled by the Unified Strength Theory and radius-dependent Young's modulus. While, the modulus was defined as a direct function of radius rather than the confining pressure, which was not exactly conform to the actual behaviour of surrounding rock mass.

In engineering practice, the distribution of confining pressure is very complex

(Jiang et al., 2001**)**. For a general excavation, the confining pressure (minor principal stress) acting on the excavation surface is zero. It increases gradually with the increasing distance between the element and the excavation surface, and will reach a constant value at locations far away from the excavation (Carranza et al., 1999; Graziani et al., 2005; Hasanpour et al., 2015). Hence, the confining pressure acting on an element is a function of distance between the element and the excavation boundary. Since the Young's modulus is depended on the confining pressure, it is necessary to consider the stress field change in the rock mass surrounding the excavation to accurately predict the ground response, especially in deep buried excavations.

Considering the effect of the confining pressure on Young's modulus, the stress and deformation of rock mass around a circular tunnel were calculated by both analytical and numerical methods. The influence of the confining-dependent Young's modulus in surrounding rock was estimated quantitatively in the ground reaction analyses.

3.2 Relation of confining pressure and young's modulus

Generally, the Young's modulus of rock mass was often assumed to be uniform in the ground reaction analyses (Carranza et al., 1999; Graziani et al., 2005; Hasanpour et al., 2015). However, it was observed that the Young's modulus around an excavation was not constant, but rather non-uniform (Zhang et al., 2012; Cai et al., 2015**)**. The Young's modulus of rock mass depends on many factors such as rock quality and confinement. In particular, confinement has a large influence on the Young's modulus. Hence, the stress redistribution due to excavation has a profound influence on the Young's modulus in underground engineering.

Based on a large amount of laboratory test results, You et al., (2003) pointed out that high confining pressure influence the Young's modulus of specimen from weathered rock or weak rock significantly. The relationship between confining stress and Young's modulus for rock masses was approximate to be exponent dependence. The increasing of fiction in the fissures with confining pressure reduces the shear slide, which makes Young's modulus higher.

To obtain a general function to describe the non-linear Young's modulus model, Cai et al. selected four sets experimental data of different rocks (Meglis et al.,1996**;** He et al., 2006**;** Mohammad et al., 2013; Cai et al., 2015**)**, and get the best-fit curves. Fig. 1 presented the relationship between the confining pressure and the Young's modulus for the selected test data and the best-fit curves using the non-linear weighted fitting

method. The best-fit equations that correspond to different rocks were also shown in Fig. 1.

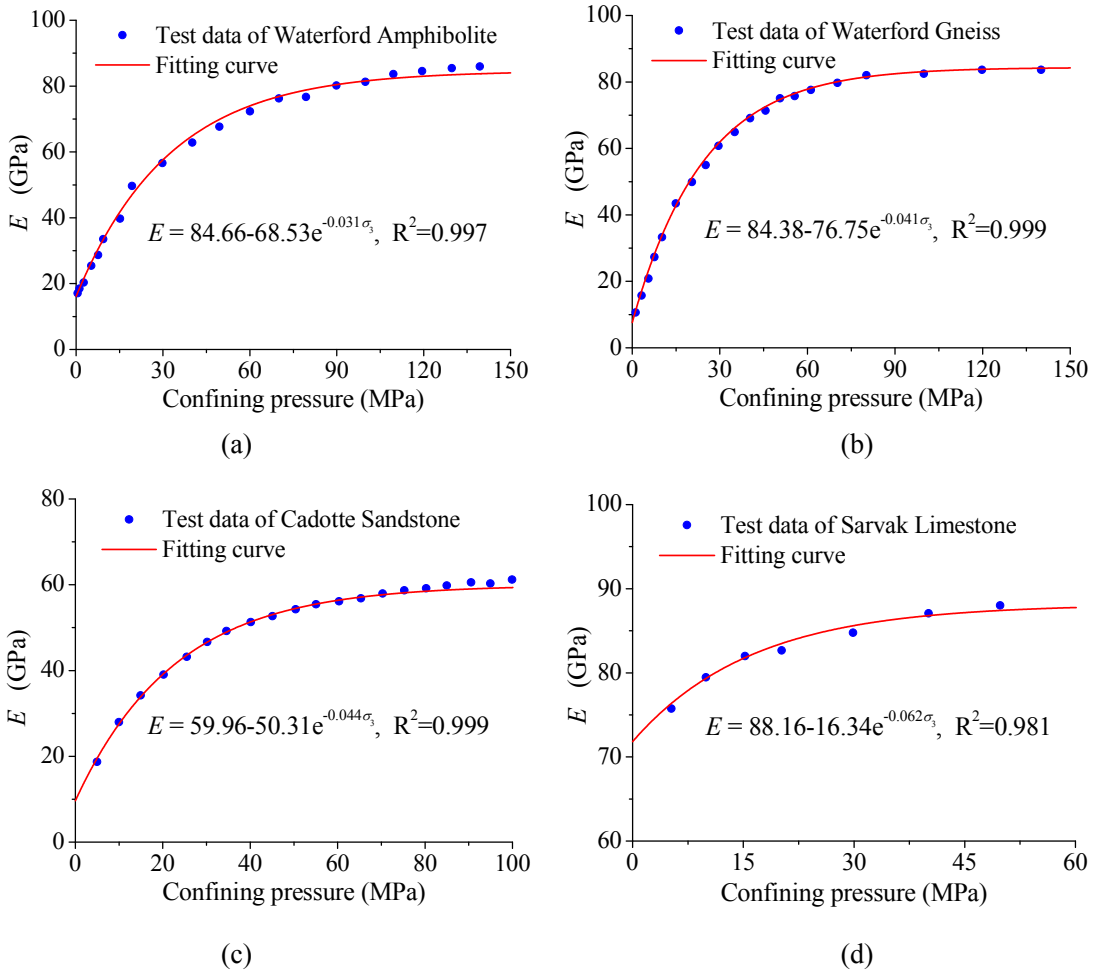

Fig. 1 The Young's modulus versus confining pressure of the experimental data and best-fit curves (a) Waterford amphibolites, (b) Waterford gneiss, (c) Cadotte Sandstone, and (d) Sarvak limestone

Based on the fitting results, the non-linear model of Young's modulus and minor principal stress was shown in Fig. 2. A non-linear function was proposed to describe the relationship between the Young's modulus and confining pressure (Cai et al., 2015):

$$E = E_{max} - (E_{max} - E_0)\, e^{(-a*\sigma 3)} . \quad (1)$$

where E_{max} is the maximum Young's modulus at the critical confining pressure, E_0 is the Young's modulus at no confining condition, and a is a model constant. This function can describe the curves very well for rock masses at non-uniform confinement condition. The physical meaning of the properties in Eq. (1) is clear. E_{max} can be considered as the Young's modulus of rock mass at in-situ stress state; E_0 can be viewed as the minimum

Young's modulus at the excavation surface, and *a* controls the non-linearity of the curve and it varies for different rock masses. The influence of model constant *a* will be discussed later.

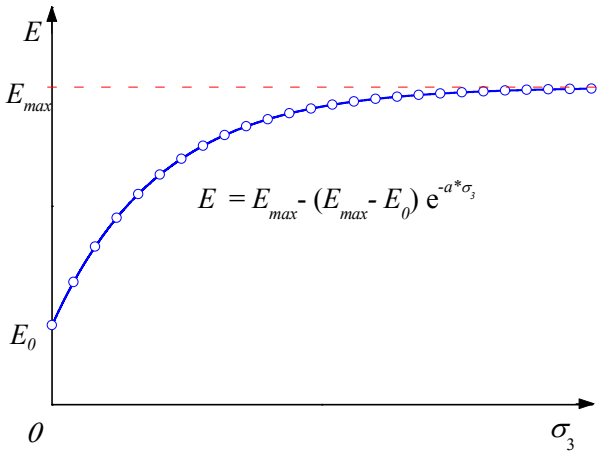

Fig. 2 The relationship of Young's modulus and confining pressure (minimum principal stress)

As the confining pressure could influence the Young's modulus dramatically, it was necessary to estimate the influence of the non-linear Young's modulus model on the deformation and failure characteristics of rock mass near excavation boundaries. Because of the lacking of well controlled in-situ experiments, field data was rarely available to determine the influence of the non-linear Young's modulus. Fortunately, the development of semi-analytical and numerical methods based on the computer makes it possible to estimate the influence of the confining-dependent Young's modulus in surrounding rock quantitatively in the ground reaction analyses.

3.3 Ground reaction analyses of a circular tunnel

The confining-dependent Young's modulus model was applied in the ground reaction analyses of a circular tunnel to reveal its influence on the tunnel convergence.

3.3.1 Problem description

The excavation of long deep tunnels with circular cross section under hydrostatic in-situ stress condition could be considered as an axial symmetry plane strain problem, while neglecting the influence of gravity, and restricting the out-of-plane principal stress as intermediate stress (Li et al., 2013; Mohamad et al., 2013). The geomechanics sign convention was employed, and the radial displacement towards tunnel axis was taken as

positive consequently. The stress and displacement redistributions (or namely ground responses) after excavation were evaluated with different Young's modulus models.

3.3.2 Equilibrium equations for rock mass

Consider an infinitesimal volume in the radial direction as shown in Fig. 3. The rock mass is subjected to a radial stress σ_r, a tangential stress σ_t. The static equilibrium condition of the infinitesimal rock mass volume can be formulated as:

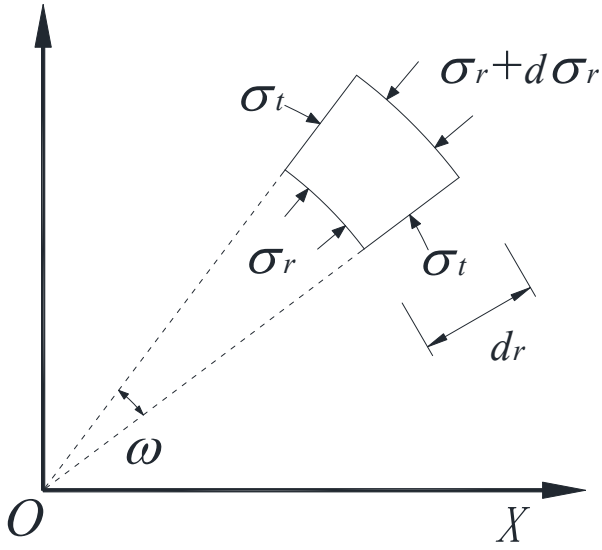

Fig. 3 Static equilibrium condition for the surrounding rock mass.

$$\sigma_r r d\omega L_z + 2\sigma_t dr L_z \sin\frac{d\omega}{2} = (\sigma_r + d\sigma_r)(r + dr)d\omega L_z . \tag{2}$$

Noticing that $\sin(\frac{d\omega}{2})$ approximately equals $\frac{d\omega}{2}$ since $d\omega$ is an infinitesimal, the equilibrium equation can be deduced as:

$$\frac{d\sigma_r}{dr} = \frac{\sigma_t - \sigma_r}{r} . \tag{3}$$

When applying Eq. (3) to the elastic region, where the stress state of rock mass should verify the hydrostatic in-situ stress condition that the sum of σ_r and σ_t equals $2P_0$, the equilibrium equation for elastic region can be formulated as:

$$\frac{d\sigma_r}{dr} = \frac{2P_0 - 2\sigma_r}{r} . \tag{4}$$

When applying it to the plastic region, where the stress state of rock mass should verify the Mohr–Coulomb failure criterion, the equilibrium equation for the plastic

region can be formulated as:

$$\frac{d\sigma_r}{dr} = \frac{(K_p - 1)\sigma_r + \sigma_c}{r}. \tag{5}$$

Where, σ_c is a dynamic value which is always changing with the major principal plastic strain ε_1^p as shown below:

$$\sigma_c = \begin{cases} \sigma_c^1 - \dfrac{(\sigma_c^1 - \sigma_c^2)\varepsilon_1^{\,p}}{\alpha\varepsilon_1^e} & (0 \le \varepsilon_1^{\,p} \le \alpha\varepsilon_1^e) \\ \sigma_c^2 & (\varepsilon_1^{\,p} \ge \alpha\varepsilon_1^e) \end{cases}. \tag{6}$$

3.3.3 Displacement compatibility equations for rock mass

Due to the plane strain axial symmetry assumption, the strain-displacement relationships for the rock mass can be simplified significantly as:

$$\frac{du}{dr} = \varepsilon_r \quad \frac{u}{r} = \varepsilon_t. \tag{7}$$

In the elastic region, according to Hook's law, the tangential strain of the rock mass can be evaluated from its stress state, as formulated in Eq. (8), where E and ν are the Young's modulus and the Poisson ratio of the rock mass. Here, E is a dynamic value which is always changing with the confining pressure as shown in Eq. (1).

$$\varepsilon_t = \left(\frac{\sigma_t}{E} - \nu\frac{\sigma_r}{E} - \nu\frac{2P_0\nu}{E}\right) - \left(\frac{P_0}{E} - \nu\frac{P_0}{E} - \nu\frac{2P_0\nu}{E}\right). \tag{8}$$

Notice that only the strain caused by tunnel excavation is concerned, which means the initial strain due to in-situ stresses should be removed. Then, associating these two equations and considering the hydrostatic in-situ stress condition, the displacement compatibility equation for the elastic region can be formulated as Eq. (9).

$$u = r\varepsilon_t = \frac{P_0 - \sigma_r}{E}(1+\nu)r. \tag{9}$$

For the plastic region, the incremental theory of plasticity (Graziani **et al.,** 2005) is adopted, and the loading path refers to a monotonic decrease of the fictitious inner pressure, corresponding to the advancing of the tunnel face. Consequently, the rates of all mechanical variables can be evaluated by their first-order derivatives with respect to P_i. The total strain rate consists of both elastic part and plastic part, as shown in Eq. (10). The elastic part is controlled by Hooke's law and the plastic part by the potential flow rule, as formulated by Eqs. (11) and (12), respectively. The relationship between the strain rate and the displacement velocity is simplified by virtue of axial symmetry and

formulated by Eq. (13).

$$\dot{\varepsilon}_r = \dot{\varepsilon}_r^{\,e} + \dot{\varepsilon}_r^{\,p}, \qquad \dot{\varepsilon}_\theta = \dot{\varepsilon}_\theta^{\,e} + \dot{\varepsilon}_\theta^{\,p}, \tag{10}$$

$$\dot{\varepsilon}_r^{\,e} = \frac{1-\nu}{2G}\dot{\sigma}_r - \frac{\nu}{2G}\dot{\sigma}_\theta, \quad \dot{\varepsilon}_\theta^{\,e} = \frac{1-\nu}{2G}\dot{\sigma}_\theta - \frac{\nu}{2G}\dot{\sigma}_r, \tag{11}$$

$$\dot{\varepsilon}_r^{\,p} = \lambda\frac{\partial g}{\partial \sigma_r} = \lambda, \quad \dot{\varepsilon}_\theta^{\,p} = \lambda\frac{\partial g}{\partial \sigma_\theta} = -\lambda K_\psi, \tag{12}$$

$$\dot{\varepsilon}_r = \frac{\partial \dot{u}}{\partial r}, \quad \dot{\varepsilon}_\theta = \frac{\dot{u}}{r}. \tag{13}$$

Here, g is the plastic potential. The rates of all mechanical variables (denoted by a dot mark) are referred as their first-order derivatives with respect to P_i. Then associating these four equations, eliminating the multiplier λ, the displacement compatibility equation for the plastic region can be expressed as:

$$\frac{\partial \dot{u}}{\partial r} + K_\psi \frac{\dot{u}}{r} = \frac{(1-\nu-\nu K_\psi)}{2G}\dot{\sigma}_r - \frac{(\nu K_\psi - K_\psi + \nu)}{2G}\dot{\sigma}_\theta. \tag{14}$$

3.3.4 Semi-analytical solution

As the Young's modulus E is a dynamic value which is always changing with the confining pressure, it is impossible to get the rigid analytical solution. The displacement compatibility equation and the equilibrium equation could only be solved by semi-analytical methods. The fourth-order Runge-Kutta method (Basheer et al., 2000) was employed, and a two dimensional finite difference algorithm (i.e. along the unloading path and along the radial direction) was programed. All the variables describing the state of the surrounding rock mass have two indices: the first indicates a certain stage in the unloading path and the second indicates a certain position in the radial direction. Supposing that at former stage (say the $(k\text{-}1)^{\text{th}}$ stage where $P_i=P_i^{(k-1)}$), all the mechanical states of the rock mass were known, the objective was to evaluate all the mechanical states at current stage (i.e. the k^{th} stage where $P_i=P_i^{(k)}$) according to their known counterparts at the former stage, which included the following three steps: stress evaluation, displacement evaluation and parameters update. The parameters that need to be updated include the transitional strength and the Young's modulus of rock mass. After one iteration finished, these known mechanical states at the current stage could be used to evaluate the mechanical states at next stage, following the same three steps, and

the iteration was repeated until the final stage.

(1) *Stress evaluation of rock mass*

The equilibrium equations (4) and (5) were solved by the fourth-order Runge-Kutta method. The radial stress at the tunnel wall $\sigma_r(k, R_a)$ was known and equals to $P_i^{(k)}$, which served as the boundary condition of the equilibrium equations. When the radial stress increased up to the critical inner pressure P_i^{cri}, record the position as the radius of the elasto-plastic interface R_e, then go on evaluating the stress state of elastic region. According to the research of Carranza-Torres et al., (1999), P_i^{cri} was a constant that only depends on the properties of rock mass itself and independent of the position of the elasto-plastic interface. The critical inner pressure can be calculated by the following formula.

$$P_i^{cri} = \sigma_{re} = \frac{2P_0 - \sigma_c(\sigma_3)}{K_p + 1}. \tag{15}$$

The radial and tangential stresses at the current stage could be determined after the stress evaluation process.

(2) Displacement *evaluation of rock mass*

For the elastic region, the radial displacement of the rock mass could be evaluated directly by the radial stress of rock mass at the current stage, according to Eqs. (1) and (9). For the plastic region, the radial and tangential stress rates $\dot{\sigma}_r(k,r)$ and $\dot{\sigma}_t(k,r)$ should be first evaluated by their first-order difference with respect to P_i, as shown in Eq. (16).

$$\dot{\sigma}(k,r) = \frac{\sigma(k,r) - \sigma(k-1,r)}{dP_i} \quad (r \le R_e). \tag{16}$$

Similarly, the deformation rate at the elasto-plastic interface $\dot{u}(k, R_e)$, which served as the boundary condition of the compatibility equation, could also be obtained by its first-order difference with respect to P_i. Then the fourth-order Runge-Kutta method was utilized again to evaluate the deformation rate at each sequential calculation point (inward radial direction) according to the compatibility equations (14). Finally, the displacement at the current stage could be obtained by accumulating the displacement increment at the current stage to its counterpart at the former stage.

$$u(k,r) = u(k-1,r) + \dot{u}(k,r)dP_i \quad (r \le R_e). \tag{17}$$

The displacement and the stresses at the former stage, as well as the stresses at the current stage, were required during this step. Then the displacement at the current stage

could be determined after the displacement evaluation process.

(3) *Rock mass* parameters *update*

After the stress evaluation, the confining pressure (minimum principal stress) at the current stage was obtained. Then, the Young's modulus of rock mass at different locations at the current stage could be computed via Eq. (1).

After the displacement evaluation, the major principle plastic strain ε_t^p at the current stage, which served as the softening parameter herein, could be evaluated by Eq. (18). Then the transitional strength at the current stage could be computed via Eq. (6).

$$\varepsilon_t^p(k,r) = \varepsilon_t(k,r) - \varepsilon_{te}(k,r) = \frac{u(k,r)}{r} - \frac{u(k,R_e)}{R_e} \quad (r \le R_e)\,. \tag{18}$$

The radial stress, tangential stresses and the displacement at the current stage were required in this step, and the Young's modulus and transitional strength of rock mass at the current stage can be determined. After these three steps, all the mechanical states at the current stage were known, which could be used to evaluate their counterparts at next stage.

3.4 Application and verification of the confining-dependent young's modulus model

The proposed method was programmed in Visual Basic development environment, and will be verified by numerical simulations in this section. An illustrative case study was conducted to demonstrate the influence of confining-dependent Young's modulus in conventional tunnelling.

3.4.1 An illustrative case study

Suppose that a circular tunnel with a design radius of 5.0 m was excavated under a hydrostatic in-situ stress of 40 MPa. The Young's modulus was assumed to transform from 20GPa (E_0) to 80GPa (E_{max}) with the increasing of confining pressure. The model constant a equaled to 0.05. The other properties of the rock mass employed were listed in Table 1.

The ground responses after excavation in the semi-analytical solution (including the distribution of stress, displacement, and Young's modulus) were shown in Fig. 4, Fig. 5, and Fig. 6 (represented by solid lines, Analytical_E_X). To highlight the influence of confining-dependent Young's modulus, the ground responses with the constant Young's

modulus model (Analytical_E_{20} and Analytical_E_{80}) were also calculated and depicted in these figures.

The semi-analytical results show that the stress distributions in the surrounding rock mass were almost the same for different models. The only difference lied in the softening region ($0 \le \varepsilon_1^p \le \alpha\varepsilon_1^e$). It is reasonable as the rock strength σ_c in this region is influenced by the major principal plastic strain ε_1^p as shown in Eq. 6. The displacement of rock mass is significantly affected by the confining-dependent Young's modulus as shown in Fig. 5. The displacement with the new model falls between the two constant Young's modulus models, and more close to the 80GPa condition. Taking the maximum tunnel convergence as the estimation index, the error between the results of E_X and E_{80} is 49.26%, and the error between the results of E_X and E_{20} is 102.96%.

The Young's modulus distributions along the radial direction in the surrounding rock mass was shown in Fig. 6. The result shows that the Young's modulus increases nonlinearly with the increasing of radial distance. It is reasonable as the confining pressure (σ_r) increases with the increasing of radial distance and the Young's modulus is influenced by the confining pressure. The result also indicated that the new model is well expressed in the calculations. The influence rules of various parameters on the deformation and failure of rock mass will be revealed in the following parameters analysis.

Table 1. The properties of rock mass employed in the standard case

ν	K_p	K_ψ	α	σ_c^1/Pa	σ_c^2/Pa
0.25	3.0	1.33	0.5	10e6	6e6

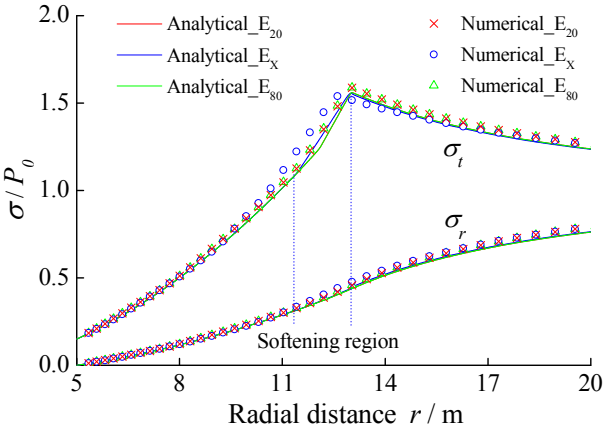

Fig. 4 The stress distributions in the surrounding rock mass

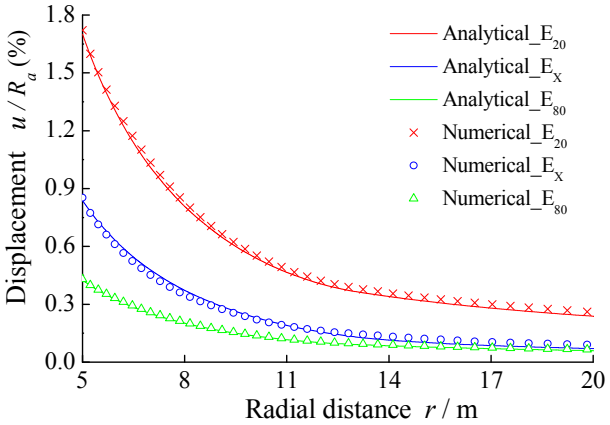

Fig. 5 The displacement distributions in the surrounding rock mass

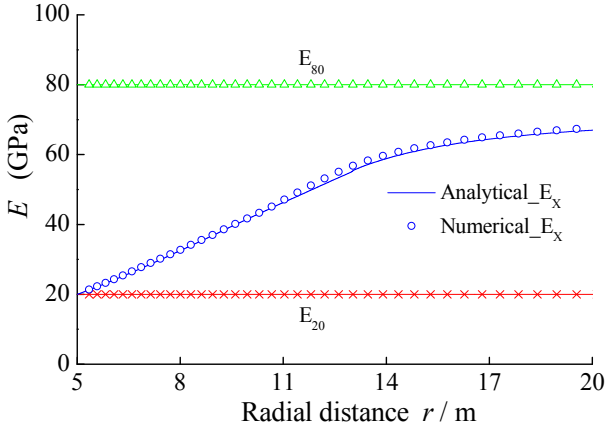

Fig. 6 The Young's modulus distributions in the surrounding rock mass

3.4.2 Verification by numerical simulations

The validity of analytical method was verified by numerical simulations (codes: FLAC^{3D}). The strain-softening constitutive laws in FLAC^{3D} are characterized by six parameters: bulk modulus K, shear modulus G, friction angle ϕ, cohesion c, dilation angle ψ, and softening parameter η. It is obvious that the former five parameters can be evaluated directly from the parameters employed in the analytical method, via following relations:

$$K = \frac{E}{3(1-2\nu)}, \tag{19-1}$$

$$G = \frac{E}{2(1+\nu)}, \tag{19-2}$$

$$K_p = \frac{1+\sin\phi}{1-\sin\phi}, \tag{19-3}$$

$$\sigma_c = 2c\sqrt{K_p}, \tag{19-4}$$

$$K_\psi = \frac{1+\sin\psi}{1-\sin\psi}. \tag{19-5}$$

However, the softening parameter in FLAC^{3D} is defined as shown in Eq. 20-1:

$$\delta\eta_{Flac} = \frac{1}{\sqrt{2}}\sqrt{(\delta\varepsilon_1{}^p - \delta\varepsilon_m{}^p)^2 + (\delta\varepsilon_m{}^p)^2 + (\delta\varepsilon_3{}^p - \delta\varepsilon_m{}^p)^2} \quad \text{with} \quad \delta\varepsilon_m^p = \frac{\delta\varepsilon_1^p + \delta\varepsilon_3^p}{3}. \tag{20-1}$$

Therefore, the shift point of the softening parameter in FLAC^{3D} can be obtained from the parameters used in the analytical method by:

$$\eta_{Flac}^s = \frac{\alpha}{\sqrt{3}}\sqrt{K_\psi{}^2 + K_\psi + 1}. \tag{20-2}$$

The confining-dependent Young's modulus model used in the semi-analytical method cannot be directly simulate by the default model in FLAC^{3D}. Fortunately, it provides a user-defined programming language FISH, which can adjust the Young's modulus according to the stress state of every element after every step. Then the modified Young's modulus is used in the next cycling of FLAC^{3D}.

The results from the numerical simulations were also depicted in Figs. 4-6, as denoted by triangle, cross and circle marks for three different cases respectively. In addition, the Young's modulus contour in numerical result is shown in Fig. 7. As shown in these figures, the ground responses computed by the analytical method and by the numerical simulation fit each other exactly for the most part, indicating that the semi-analytical solutions for the new model in the circular tunnel was valid. As the analytical method is two-dimensional, while the numerical method is three-dimensional, which may be the reason of the slight errors.

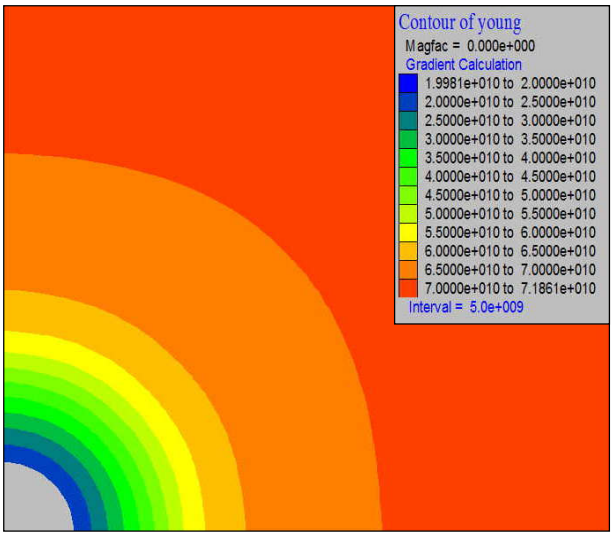

Fig. 7 The Young's modulus contours in numerical results

3.5 Parameters analysis

Parameters analysis was conducted to study the influence of different parameters in the confining-dependent Young's modulus model. The studied parameters included the maximum Young's modulus (E_{max}), the minimum Young's modulus (E_0), and the model constant a. The semi-analytical method was adopted in this part as the calculation can be finished in a few seconds. While, a lot of time is needed in numerical method to get the similar results. The maximum tunnel convergence was selected as the estimation index in this study. Taking the illustrative case above as a standard one and varying a single parameter, the relative significance of different parameters on the deformation characteristics of rock mass will be illustrated.

3.5.1 Influence of the maximum Young's Modulus

The maximum Young's modulus (E_{max}) was selected to study its influence on the tunnel convergence. As the minimum Young's modulus (E_0) is 20GPa in the standard case, the E_{max} is set from 20GPa to 100GPa in the following studies. Meanwhile, the other parameters are all the same with the standard case.

The evolution of the maximum displacement with the increasing of maximum Young's modulus was shown in Fig. 8. To highlight the difference, the results of constant Young's modulus model (E_0 and E_{max}) were also calculated and depicted in this figure. The results show that the maximum displacement in the new model decreases

gradually with the increasing of E_{max}. Similar behaviour was found in the case of constant Young's modulus model when the Young's modulus equals to E_{max}. In the case of constant Young's modulus model when the Young's modulus equals to E_0, the maximum displacement doesn't change. When the E_{max} is very small, the difference between E_{max} and E_0 is very small, which certainly resulting in small difference for different models.

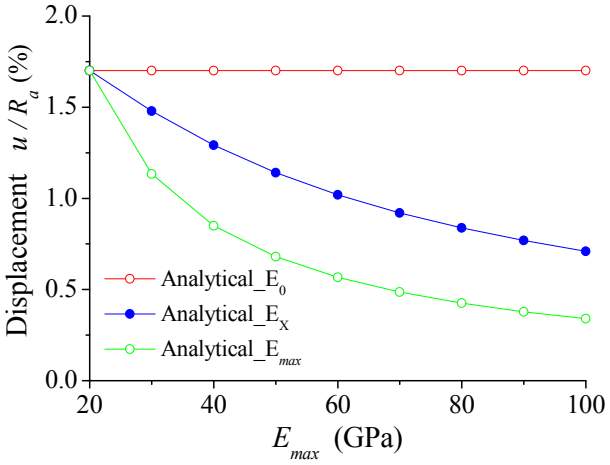

Fig. 8 The evolution of the maximum displacement with the increasing of E_{max}

3.5.2 Influence of the minimum Young's Modulus

The influence of the minimum Young's modulus E_0 was studied in this part. As the maximum Young's modulus E_{max} is 80GPa in the standard case, E_0 was set from 10GPa to 80GPa in the following examples. The other parameters were also the same with the standard case. The evolution of the maximum displacement with the increasing of E_0 were shown in Fig. 9.

The results show that the maximum displacement decreases sharply with the increasing of E_0 in the case of constant Young's modulus E_0. The displacement with the new model always falls between the two constant Young's modulus models. When the value of E_0 is close to E_{max}, the difference between the three cases is also small. The result illustrates that the difference between E_{max} and E_0 is a key parameter that influence the error between the confining-dependent Young's modulus model and uniform Young's modulus model.

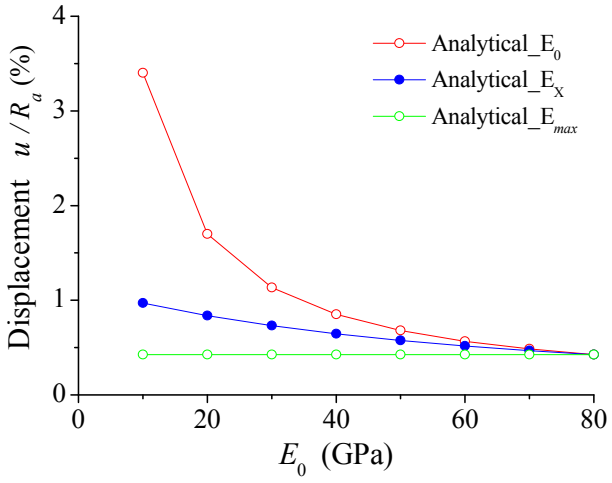

Fig. 9 The evolution of the maximum displacement with the increasing of E_0

3.5.3 Influence of the model constant

The influence of model constant (a) was studied in this part. It was set from 0.001 to 1 in the following examples. The other parameters were also same with the standard case. The evolution of the maximum displacement with the increasing of model constant are shown in Fig. 10. The results of two constant Young's modulus models were also depicted in this figure.

The results show that the maximum displacement from the new model decreases gradually with the increasing of model constant. There is a clearly trend that the maximum displacement from the confining-dependent Young's modulus model gradually approaching the E_{max} case from the E_0 case with the increasing of model constant. This behaviour can be explained by the distribution of Young's modulus with different value of model constant as shown in Fig. 11. The results above show that the confining-dependent Young's modulus of rock mass influences the tunnel convergence dramatically, which shouldn't be ignored.

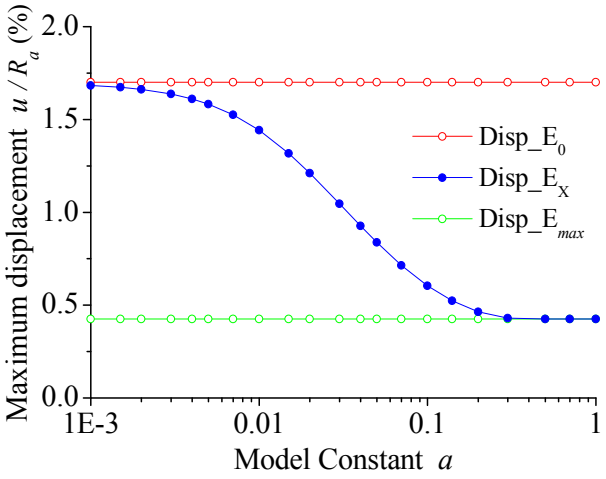

Fig. 10 The evolution of the maximum displacement and the error with the increasing of model constant

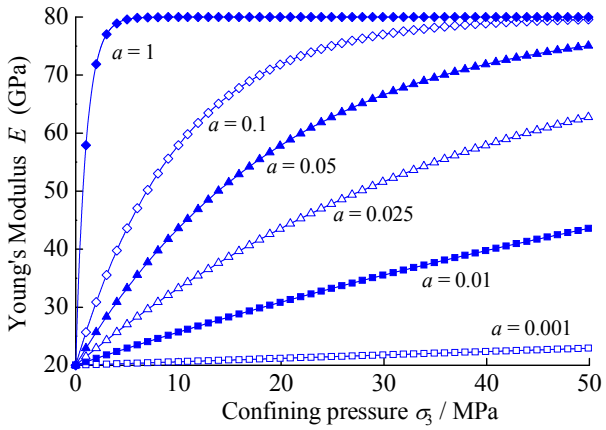

Fig. 11 The distribution of Young's modulus with different value of model constant

3.6. Predicting the deformation of surrounding rock mass in tunnel construction

3.6.1. Geological and excavation conditions of Tawara saka tunnel

The excavation of Tawara saka Tunnel on Kyushu Shinkansen in Nagasaki was taken as an example to explain the influence of confining-dependent Young's modulus. The tunnel convergence at the position of 16.074km from Takeo Onsen was discussed in detail. Its buried depth is 234.9 m. There are two types of rocks around the tunnel as shown in Fig. 12. The geological investigations and the laboratory experimental results show that the strength of the rock around the tunnel is very low, and both of them are classified as DII, which belongs to the classification of the soft rock.

The dimensions of cross section and the monitoring positions for tunnel

convergence, mainly including the convergence at the crown (u_c) and at 1m above the springline (u_{sr} and u_{sl}), were schematically illustrated in Fig. 13. The standard supporting pattern in Japan was adopted. The upper stage was excavated first, and then the first lining and the rock bolts were installed immediately. After that, the displacement meters were installed and started to monitor the tunnel convergence. Then, the lower stage was excavated and supported similarly. The second lining was cast in place a few days later. The internal pressure of the support structure on the rock mass is determined to be 0.817MPa according to the monitoring data of pressure cell.

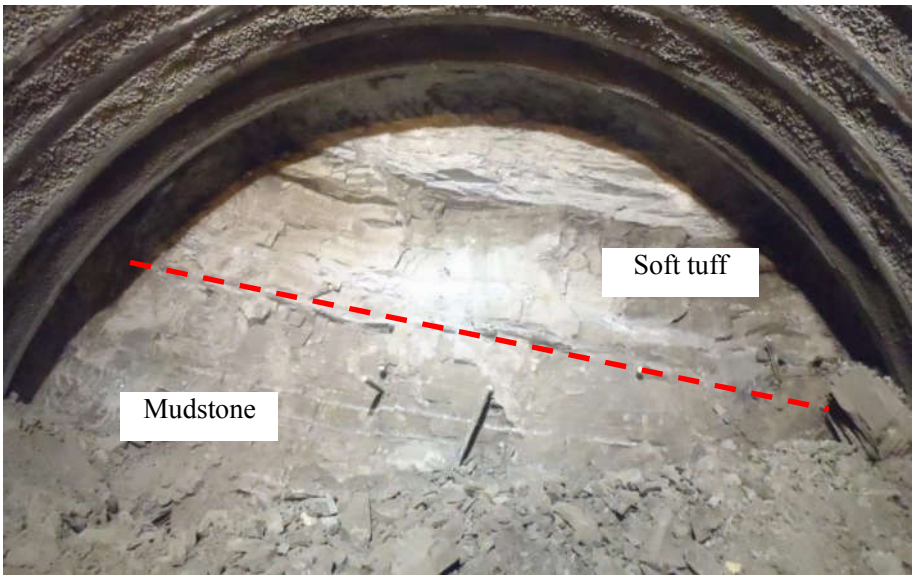

Fig. 12 The exposure of rocks on tunnel face

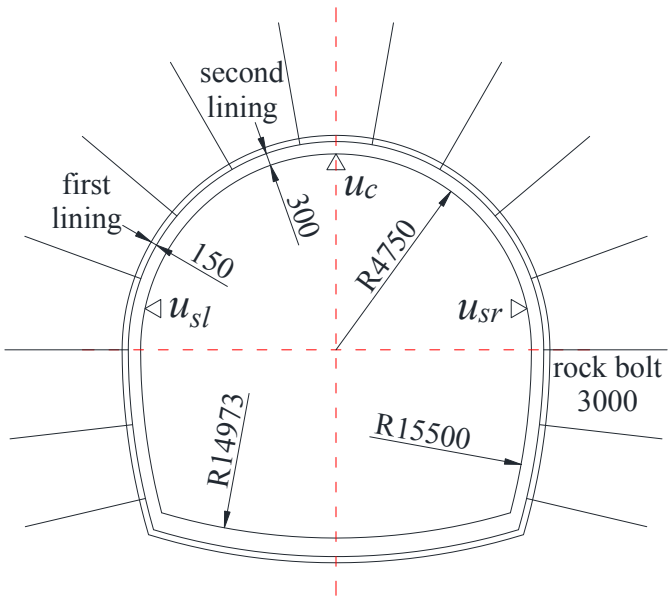

Fig. 13 The cross section dimensions and the convergence monitoring positions

3.6.2. Numerical simulation to predict the tunnel convergence

A numerical model (codes: FLAC^{3D}) including five groups was established as shown in Fig. 14, including three groups in the tunnel to be excavated and two groups to stand for the different rocks. Both of the rocks are assumed as Mohr-Coulomb materials, and their properties are listed in Table 2. The confining-dependent Young's modulus model here is also characterized by adjust the Young's modulus according to the stress state of every element.

In the numerical simulation, the groups 1 and 2 were set to be null after the initial state, and then an internal pressure of 70% in situ stress was applied on the tunnel surface to simulate the support effect of the rock mass ahead of the tunnel face and the support structure. After the balance of the calculation model, the displacement were initialed to correspond to the in situ monitoring data. Then, the group 3 was set to be null, and an internal pressure was applied on the tunnel surface. Finally, the internal pressure was reduced gradually to simulate the advance of tunnel face. According to the monitoring data of pressure cell, the internal pressure was identified to be 0.817MPa to replace the effect of support.

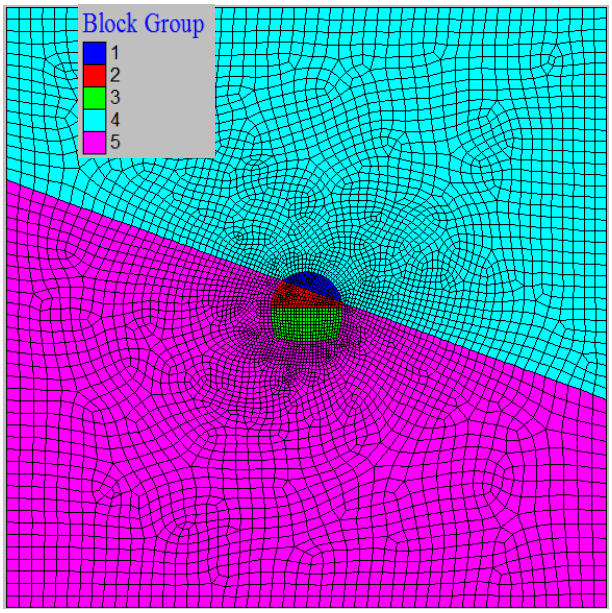

Fig. 14 Numerical model of Tawara saka Tunnel at 16.074km

Table 2. The properties of rock mass employed in the standard case

	E_0/GPa	E_{max}/GPa	a	ν	σ_c^1/MPa	σ_c^2/MPa	ρ/kg/m^3	K_p	K_ψ	α
Soft tuff	0.80	2.20	0.06	0.35	1.0	0.4	2100	3.0	1.33	0.5
Mudstone	0.15	0.70	0.04	0.35	0.5	0.2	2200	3.0	1.33	0.5

The results from the numerical simulations by two methods were shown in Fig. 15 and Fig. 16 respectively. The surface displacement from different numerical methods were compared with the monitoring data in Fig. 17. All the displacements shown in Fig. 17 was ten times magnified with respect to the original data to demonstrate the difference more clearly. The quantitative data was shown in Table 3. The surface displacements of the tunnel for three monitoring points were also shown in Table 3. The errors of tunnel surface displacement with different methods compared with the monitoring data was analyzed in Table 4.

Both the numerical results show that the tunnel convergence is unsymmetrical, which is consistent with the monitoring data. The displacement at the left side is much larger than the right side. This is reasonable as the rock strength and Young's modulus of the left part is much smaller than the right side.

The tunnel convergence computed from the confining-dependent Young's modulus model is smaller than that from the uniform Young's modulus model, and more close to the field test data. The error analysis shows that the error with respect to the monitoring data is largely reduced with the confining-dependent Young's modulus model in most part. The data at 1m above the springline fits much better than the monitoring position of tunnel crown. May be the relative sliding between the two types of rock mass happened in situ, which result in a large displacement in the X direction. While, this behaviour is not occurred as the bond between the two types of rock mass is too strong in the laboratory test.

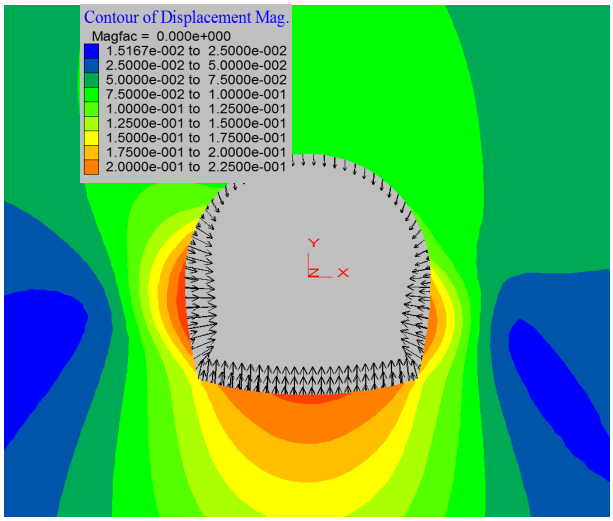

Fig. 15 Displacement of the rock mass around the tunnel by uniform Young's modulus model

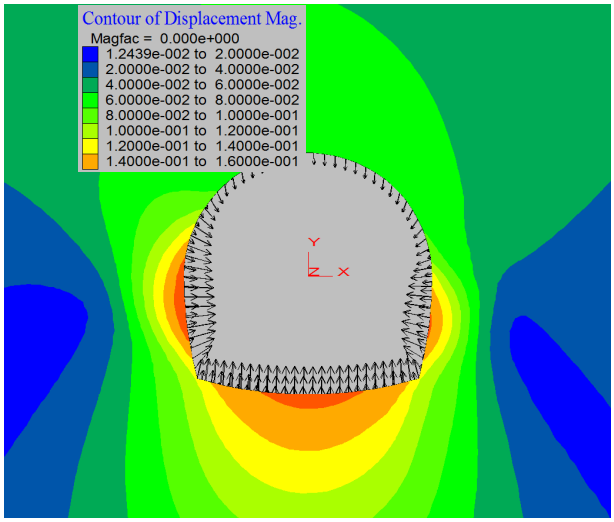

Fig. 16 Displacement of the rock mass around the tunnel by non-uniform Young's modulus model

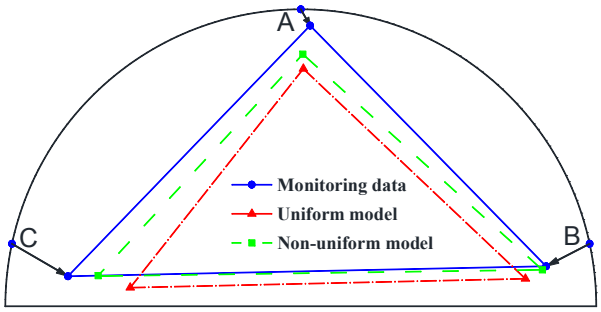

Fig. 17 Comparing of different numerical results with the monitoring data

Table 3. The surface displacement and error of the surrounding rock mass with different methods

	u_c_x	u_c_y	u_{sr}_x	u_{sr}_y	u_{sl}_x	u_{sl}_y
Monitoring data/m	0.015	-0.026	-0.070	-0.036	0.090	-0.052
Uniform model/m	0.0041	-0.0951	-0.1033	-0.0560	0.1901	-0.0703
Non-uniform model/m	0.0033	-0.0718	-0.0760	-0.0417	0.1378	-0.0518

Table 4. The errors of surface displacement with different methods

	u_c_x	u_c_y	u_{sr}_x	u_{sr}_y	u_{sl}_x	u_{sl}_y
Error of uniform model / %	-72.9	265.7	47.5	55.5	111.2	35.1
Error of non-uniform model / %	-78.1 ↑	176.3 ↓	8.6 ↓	15.8 ↓	53.2 ↓	-0.3 ↓

As the other properties of rock mass, such as the residual strength and dilation angle, are also influenced by the confining pressure, which are not considered in these simulations may be the reason of the slight errors. Nevertheless, the simulation results indicate that it is necessary to consider the confining-dependent of Young's modulus in rock mass around the tunnel.

3.7 Conclusions

According to test data and research achievement available in literature, the relationship between Young's modulus and confining pressure was introduced first. In an underground excavation, the confining pressure acting on an element is a function of distance between the element and the excavation boundary. Since the Young's modulus is depended on the confining pressure, it is necessary to consider the stress field change in the rock mass surrounding the excavation to accurately predict the ground response, especially in deep buried excavations.

Based on the plane strain axial symmetry assumption and the incremental theory of plasticity, equilibrium equations and compatibility equations of rock mass around a circular tunnel were deduced theoretically. These equations were programmed in the Visual Basic development environment, and a semi-analytical solution was achieved with the fourth Runge-Kutta method. In the calculation, the Young's modulus of rock mass was real-time updated according to the local confining pressure.

Considering the effect of the confining pressure on the Young's modulus, the stress

and deformation of rock mass was calculated in the ground reaction analyses by both analytical and numerical methods. The influence of the confining-dependent Young's modulus in surrounding rock was estimated quantitatively. Taking the maximum tunnel convergence as the estimation index, the error between the results of confining-dependent Young's modulus model and two uniform Young's modulus models were 49.26% and 102.96%.

Parameters analysis were conducted to study the influence of the maximum Young's modulus (E_{max}), the minimum Young's modulus (E_0), and the model constant a in the confining-dependent Young's modulus model. The result illustrated that the difference between E_{max} and E_0 is a key parameter that influence the error between the confining-dependent Young's modulus model and uniform Young's modulus model. There is a clearly trend that the maximum displacement from the confining-dependent Young's modulus model gradually approaching the E_{max} case from the E_0 case with the increasing of model constant.

Finally, the Tawara saka Tunnel on Kyushu Shinkansen was taken as an example to explain the influence of the confining-dependent Young's modulus. A numerical model with two different types of rock mass was established to simulate the tunnel behaviour after excavation. Both of the numerical results showed that the tunnel convergence was unsymmetrical, which was consistent with the monitoring data. The error analysis showed that the error with respect to the monitoring data was largely reduced with the confining-dependent Young's modulus model. The simulation results indicated that it is necessary to consider the non-uniform distribution of Young's modulus in rock mass around the tunnel.

References

Agan, C., 2014, Determination of the deformation modulus of dispersible-intercalated-jointed cherts using the Menard pressuremeter test. International Journal of Rock Mechanics and Mining Sciences, 65, 20–28.

Alonso1, E., Alejano, L.R., Varas, F., Fdez-Manin, G., and Carranza-Torres, C., 2003, Ground response curves for rock masses exhibiting strain-softening behaviour. International Journal for Numerical and Analytical Methods in Geomechanics, 27, 1153–1185.

Arslan, A.T., Koca, M.Y., Aydogmus, T., Klapperich, H., and Yılmaz, H.R., 2008, Correlation of Unconfined Compressive Strength with Young's Modulus and

Poisson's Ratio in Gypsum from Sivas (Turkey). Rock Mechanics and Rock Engineering, 41, 941–950.

Asghar, R., Lohrasb, F., and Manouchehr, S., 2014, Development of a new method for RMR and Q classification method to optimize support system in tunneling. Frontiers of Structural and Civil Engineering, 8, 448–455.

Bahar, R., Baidi, F., Belhassani, O., Vincens, E., Undrained strength of clays derived from pressuremeter tests. European Journal of Environmental and Civil Engineering, 2012, 16(10): 1238-1260.

Basheer, I., and Hajmeer, M., 2000, Artificial neural network: fundamentals, computing, design and application. Journal of Microbiological Methods, 43, 3–31.

Brown, E., Bray, J., Landayi, B., and Hoek, E., 1983, Ground response curves for rock tunnels. Journal of Geotechnical and Geoenvironmental Engineering, 109, 15–39.

Cai, M., and Wang, X., 2015, A non-uniform velocity model and Flac/Specfem2d coupled numerical simulation of wave propagation in underground mines. 13th ISRM International Congress of Rock Mechanics, Montreal, May 10–13, p. 1–17

Carranza, T.C., and Fairhurst, C., 1999, The elasto-plastic response of underground excavations in rock masses that satisfy the Hoek-Brown failure criterion. International Journal of Rock Mechanics and Mining Sciences, 36, 777–809.

Domede, N., Parent, T., Sellier, A., Mechanical behaviour of granite: a compilation, analysis and correlation of data from around the world. European Journal of Environmental and Civil Engineering, 2017, doi: 10.1080/19648189.2016.1275984

Feng, X.D., and Jimenez, R., 2014, Bayesian prediction of elastic modulus of intact rocks using their uniaxial compressive strength. Engineering Geology, 173, 32–40.

Géraldine, V., Marrec, L., Lalaonirina, L. R., Determination of the bulk elastic moduli of various concretes by resonance frequency analysis of slabs submitted to impact echo. European Journal of Environmental and Civil Engineering, 2011, 15(4): 601 – 617.

Gokceoglua, C., Sonmeza, H., and Kayabasi, A., 2003, Predicting the deformation moduli of rock masses. International Journal of Rock Mechanics and Mining Sciences, 40, 701–710.

Graziani, A., Boldini, D., and Ribacchi, R., 2005, Practical estimate of deformations and stress relief factors for deep tunnels supported by shotcrete. Rock Mechanics and Rock Engineering, 38, 345–372.

Guan, Z., Jiang, Y., and and Tanabasi, Y., 2007, Ground reaction analyses in conventional tunneling excavation. Tunnelling and Underground Space Technology, 22, 230–237.

Guo, X., Liang, S., and Shen, Z., 2015, Experiment on aluminum alloy members under axial compression. Frontiers of Structural and Civil Engineering, 9, 48–64.

Hasanpour, R., Rostami, J., and Barla, G., 2015, Impact of Advance Rate on Entrapment Risk of a Double-Shielded TBM in Squeezing Ground. Rock Mechanics and Rock Engineering, 48, 1115–1130.

He, T.W., 2006, P- and S-wave velocity measurement and pressure sensitivity analysis of AVA response. Master thesis. University of Alberta, Alberta, Canada, 178 p.

Hoek, E., and Diederichs, M.S., 2006, Empirical estimation of rock mass modulus. International Journal of Rock Mechanics and Mining Sciences, 43, 203–215.

Hsieh, A., Dyskin, A.V., and Dight, P., 2014, The increase in Young's modulus of rocks under uniaxial compression. International Journal of Rock Mechanics and Mining Sciences, 70, 425–434.

Isik, N.S., Ulusay, R., and Doyuran, V., 2008, Deformation modulus of heavily jointed–sheared and blocky greywackes by pressuremeter tests: Numerical, experimental and empirical assessments. Engineering Geology, 101, 269–282.

Jiang, Y., Yoneda, H., and Tanabashi, Y., 2001, Theoretical estimation of loosening pressure on tunnels in soft rocks. Tunnelling and Underground Space Technology, 16, 99–105.

Karakus, M., Kumral, M., and Kilic, O., 2005, Predicting elastic properties of intact rocks from index tests using multiple regression modelling. International Journal of Rock Mechanics and Mining Sciences, 42, 323–330.

Kayabasi, A., Gokceoglub, C., and Ercanoglu, M., 2003, Estimating the deformation modulus of rock masses: a comparative study. International Journal of Rock Mechanics and Mining Sciences, 40, 55–63.

Kodama, J., Miyamoto, T., Kawasaki, S., Fujii, Y., Kaneko, K., and Hagan, P., 2013, Estimation of regional stress state and Young’s modulus by back analysis of mining-induced deformation. International Journal of Rock Mechanics and Mining Sciences, 63, 1–11.

Leite, M.H., and Ferland, F., 2001, Determination of unconfined compressive strength and Young's modulus of porous materials by indentation tests. Engineering

Geology, 59, 267–280.

Li, B., Mao, J., Lv, J., Zhou, L., Effects of micropore structure on hydration degree and mechanical properties of concrete in later curing age. European Journal of Environmental and Civil Engineering, 2016, 20(5): 544-559

Li, S.C., Cong, H., Li, L.P., Song, S.G., Zhou, Y., and Shi, S.S., 2013, Bidirectional construction process mechanics for tunnels in dipping layered formation. Tunnelling and Underground Space Technology, 36, 57–65.

Li, S.C., and Wang, M.B., 2008, Elastic analysis of stress–displacement field for a lined circular tunnel at great depth due to ground loads and internal pressure. Tunnelling and Underground Space Technology, 23, 609–617.

Meglis, I.L., Greenfield, R.J., Engelder, T., and Graham, E.K., 1996, Pressure dependence of velocity and attenuation and its relationship to crack closure in crystalline rocks. Journal of Geophysical Research, 17, 523–517.

Mohamad, K., and Chang, Y.O., 2013, Evaluation of deformation parameter for deep excavation in sand through case histories. Computers and Geotechnics, 47, 57–67.

Mohammad, R.A., and Najibi, A.R., 2013, The effect of confining pressure on elastic wave velocities and dynamic to static Young modulus ratio. Geophysics, 78, 135–142.

Nawrocki, P.A., and Dusseault, M.B., 1995, Modelling of damaged zones around openings using radius-dependent Young's modulus. Rock Mechanics and Rock Engineering, 28, 227–39.

Palmstrom, A., and Singh, R., 2001, The deformation modulus of rock masses-comparisons between in situ tests and indirect estimates. Tunnelling and Underground Space Technology, 16, 115–131.

Tinoco, J., Correia, A.G., and Cortez, P., 2014, A novel approach to predicting Young's modulus of jet grouting laboratory formulations over time using data mining techniques. Engineering Geology, 169, 50–60.

Wang, X.S., Jiang, X.W., Wan, L., Song, G., and Xia, Q., 2009, Evaluation of depth-dependent porosity and bulk modulus of a shear using permeability-depth trends. International Journal of Rock Mechanics and Mining Sciences, 46, 1175–1181.

Yang, J.P., Chen, W.Z., Yang, D.S., and Tian, H.M., 2016, Estimation of elastic moduli of non-persistent fractured rock masses. Rock Mechanics and Rock Engineering,

49, 1977–1983.

You, M.Q., 2003, Effect of confining pressure on the young's modulus of rock specimen and the friction in fissures. Rock and Soil Mechanics, S2, 167–170.

Zhang, C.G., Zhao, J.H., Zhang, Q.H., and Hu, X.D., 2012, A new closed-form solution for circular openings modeled by the Unified Strength Theory and radius-dependent Young's modulus. Computers and Geotechnics, 42, 118–128.

Zhang, J., Chen, H.Z., Huang, H.W., and Luo, Z., 2015, Efficient response surface method for practical geotechnical reliability analysis. Computers and Geotechnics, 69, 496–505.

Part II

Support system design of mountain tunnel in soft rock

4 Performance of a new yielding rock bolt under pull and shear loading conditions

4.1 Introduction

Many mines around the world are currently being operated at depths greater than 1000m, for example those in China, Germany, Australia, and South Africa (Amusin 1998; Li et al. 2012). Some mountain tunnels for traffic and water diversion tunnel in water power project are buried under 2000m (Li et al. 2011). The high in-situ stress at depth puts towards a higher request on the underground support technology.

The major stability concern in the shallow depths is rock falls under gravity. Conventional rock bolts are usually installed to stabilize the loosened rock blocks. The bolts are only required to be strong enough to sustain the dead weight of the loosened block (Hoek 2007). Bolt strength is the crucial parameter in rock support design. The fully encapsulated rebar bolt is the most widely used rock bolt in geotechnical engineering. It is verified to be a satisfactory bolt for this purpose since it fully utilizes the strength of the bolt steel (Li 2012).

The substantial difference of the rock mass at great depth and at shallow depth is the significant increase of in-situ stresses. As a consequence, large squeezing deformation may appear in soft and weak rocks, or rock burst may occur in hard rocks (Ortlepp 2001; Ansell 2005; Li 2010). It is observed that many conventional bolts fail when experiencing large shear and opening displacement at rock joints/fractures (Ortlepp 2000; Li et al. 2011; Srivastava 2015). The conventional rock bolt is easy to be damaged when experiencing large rock displacement. The premature failure of conventional rock bolt implies that it is too stiff to sustain rock dilations in high stress condition (Stillborg 1994; Hoek et al. 1995). The desired rock bolt for supporting in high stress rock masses should be not only strong, but also deformable, i.e., energy absorbent.

In this paper, the progress of yielding rock bolt is reviewed firstly. After that, a new yielding rock bolt is introduced in details, including the structure and principle. The performance of the new bolt is verified by pull tests and shear tests.

4.2 A review of the yielding rock bolts

The support system used in depth should be able to carry high loads and also

accommodate large deformation without experiencing serious damage. Yielding support was first proposed and used in the deep gold mines of South Africa (Cook and Ortlepp 1968). Windsor and Thompson (1992) proposed the concept of ideal reinforcement device, which should have the strength of rebar and the deformation capacity of Split Set bolts, with the ability to be rapidly mobilized to a load level similar to the strength of the material. The yielding rock bolt that have high strength is called energy-absorbing rock bolt (Li 2010).

So far, there have been dozens of yielding rock bolts. According to the yielding mechanism, they can be summarized as structural components sliding type and steel deformation type as shown in Figure 1.

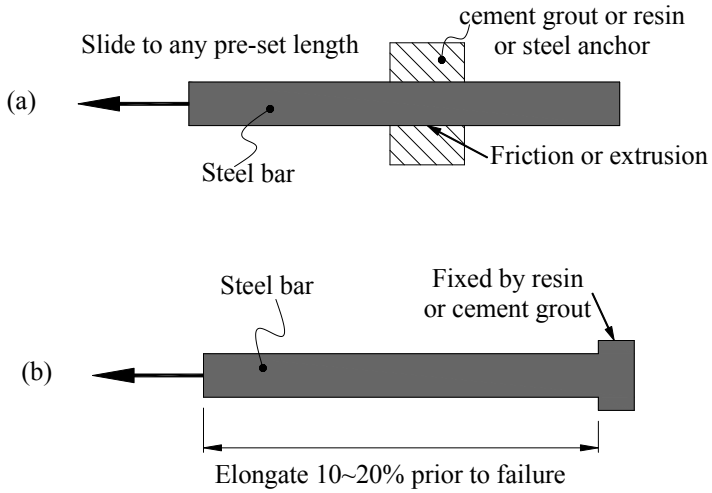

Fig. 1. Yielding mechanism of rock bolt. (a) structural components sliding, (b) steel deformation

The structural components sliding type bolt mainly includes Cone bolt, Roofex, He-bolt and Cold drawing bolt. Cone bolt was the first energy-absorbing rock bolt used in South Africa gold mine (Jager 1992). It consists of a smooth steel bar with a flattened conical flaring, which is designed to plough through the grout when the pull load exceeds a pre-defined value. Its performance is closely controlled by the properties of the grout material, diameter of drill hole, mixing efficiency and the encapsulation condition. In most cases these factors are not completely under control, the effect of a cone bolt (or modified cone bolt) therefore is less consistent and reliable (Gillerstedt 1999). Roofex, He-bolt and Cold drawing bolt are all based on a steel-steel interaction with a high quality steel bar travelling through the energy absorbing element fixed in the borehole (Salzburg 2009; Wang 2013; He et al. 2014). They have stable performance for

both large squeezing and rock burst prone grounds because of the single performance of steel-steel interaction. However, the “energy-absorber” unit makes the bolt inherently cost expensive due to its complex structure. A thicker bolt hole, which is needed, also makes the installing more complex.

The typical representative of steel deformation rock bolt is D bolt. It is a smooth steel bar with a number of anchors along its length (Li 2010). The anchors are fixed in the borehole with either cement grout or resin, while the smooth sections of the bolt between the anchors can deform freely in response to rock dilation. D bolt has large load-bearing and deformation capacities. Pull tests show that the bolt can elongate 14–20% at a high load level, thereby absorbing a large amount of energy. While, filed measurements show that resin mixing is critical to ensure that the anchors do not move in extreme conditions, according to technical information data shifts from Natural Resources Canada (Chantale and Benoit 2012). On the other hand, the pre-stress, which is necessary in deep engineering, is difficult to apply for D bolt.

Due to the limits in load capacity, deformation ability, stability and economy, it is difficult to say the performance of these bolt is absolutely satisfactory. There is large industrial requirement on developing a performance-reliable and cost-effective yielding support system.

4.3 Structure and principle of the new bolt

Generally speaking, there are two problems remained to be solved in rock bolt support technique. The first is the failure in bolt-rock interface due to shear stress concentration (Aziz et al. 2016). The second is the premature failure of rock bolt itself when the pull or shear displacement of rock mass exceeded its deformation ability. A new rock bolt, called Tension and Compression Coupled Yielding bolt (TCC Yielding bolt), was proposed by the authors. It belongs to steel deformation type just as D bolt, but its anchor unit is different, which is promising to provide a larger resistance. The new bolt also has large deformation ability, which can be suitable for both dynamic and large convergence ground conditions.

4.3.1 Structure of TCC Yielding bolt

As shown in Fig. 2, the new rock bolt mainly consists of a steel rod and two additional anchors. The steel rod is a round shape bar with varying surface conditions. The inner segment is processed into rough surface to be better bonded with the

anchoring agent. The middle of the rod has smooth surface, which can detach from the grout under pull or shear loading. The outer segment is processed for threading to assemble the nut and plate. Two additional anchors are welded on both ends of smooth segment. The inner segment of the rod and the inner additional anchor are fixed inside the borehole with either cement grout or resin, while the smooth bar has no or very weak bonding to the grout. The additional anchor at the outer end of the rock bolt can reduce the force borne by bolt plate. According to their different functions, the new bolt can be divided into three parts, namely inner anchoring segment, free-elongating segment and outer anchoring segment.

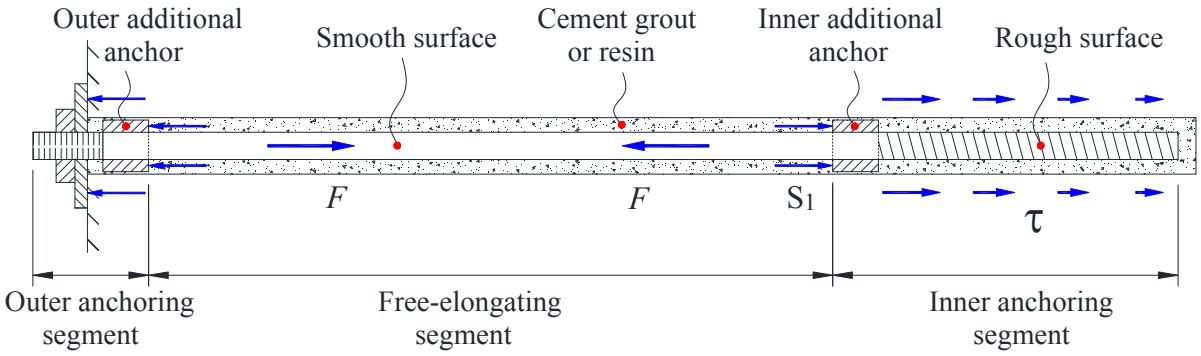

Fig. 2. Layout and stress condition of TCC-Yielding bolt

4.3.2. Principle of tension and compression coupled anchor

According to the stress states of grout, the anchor structure used in rock bolt can be divide into two mainly types, namely tensile anchor (Zhang et al. 2002; Huang et al. 2014) and pressure anchor (Zhang et al. 2009). Shear stress concentration at the interfaces of bolt-grout-rock interface is the key problem for both anchor structures. For cables, the stress concentration can be largely relieved by the separate-stretched anchors or pressure-dispersive anchors. While, the rock bolt is a single rod, and the stress dispersion methods in the cables cannot work.

The tension-type bolt includes fully encapsulated rebar bolt and partly encapsulated rebar bolt. The stress distribution of them is similar, and the partly encapsulated rebar bolt is taken as an example to introduce. The characteristics of fully encapsulated rebar bolt will be talked in next section. As shown in Fig. 3, the grout is in tension states when the rock bolt is working. The distribution of shear stress at the interfaces of bolt-grout-rock is nonuniform, and the stress concentration at the position A is very

serious. When the failure occurs at point A, the stress concentration will takes place at point B again. The gradually advanced damage at the interfaces of bolt-grout-rock interface is a great threaten for the stability of rock bolt.

The pressure-type bolt is shown in Fig. 4. It consists of an inner anchor and a steel rod which is coated with lubricant media. The steel rod has very weak bonding to the grout because of the lubricant media. When the steel rod subject to a pull loading, the load can be transmitted to the inner anchor directly. The load capacity of the pressure-type bolt depends on the strength of the grout and rock mass around the anchor and the bonding quality between them. The stress concentration around the inner anchor is also very serious, which limits the ultimate load capacity pressure-type bolt.

The stress condition of TCC-Yielding bolt is shown in Fig. 2. The deformation of the surrounding rock mass will induce a pull loading on the rock bolt. Duo to the smooth surface of the rod and the Poisson's effect, the free-elongating segment will detach from the grout under pull loading. The pull load can be transmitted to the inner anchoring segment directly. A large portion of the pull load is dissipated in lateral rock mass by the inner additional anchor, and the other part is transmitted to the rough surface rod. The grout at the outer side of the inner additional anchor is in compression state, and the grout at the inner side of the inner additional anchor is in tension state. The coupling action of them can largely increase the ultimate load capacity of the new rock bolt. The gradually advanced damage at the interfaces of bolt-grout can also be reduced effectively. The loads beard by the inner additional anchor and rough surface rod can be coordinated by adjusting the diameter of the inner anchor or the length of the rough surface segment. The new bolt integrates the tensile anchor and pressure anchor, and overcomes their shortcomings by the cooperation of the smooth surface segment, inner additional anchor and the rough surface segment. The reasonable stress distribution at the interfaces of bolt-grout-rock results in a much higher load capacity.

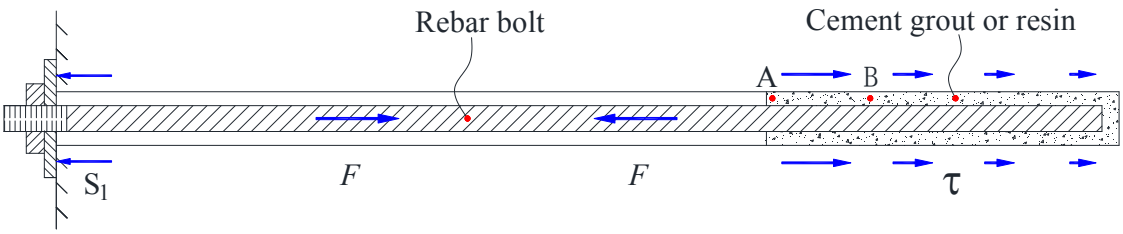

Fig. 3. Force analysis of tension-type bolt

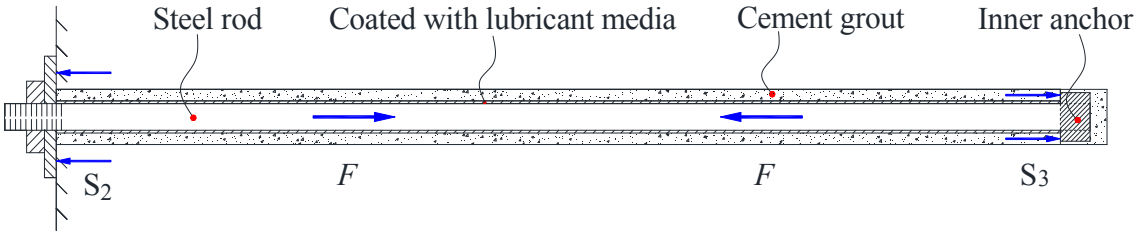

Fig. 4. Force analysis of pressure -type bolt

4.3.3. Principle of large deformation mechanism

The deformation of rock mass will induce a relative displacement between the both ends of rock bolt. When the conventional rock bolt is subjected to large deformation of rock mass, fracture opening or shearing for instance as shown in Figs. 5 and 6, an unevenly distributed stress and strain would be induced in the rock bolt. The maximum force and strain is always at the position of fracture, as shown in Fig. 7a. As the rough bar is strongly bonded to the grout, load and strain elevations at the opening fractures could result in premature failure of the rock bolt (Ortlepp 2000).

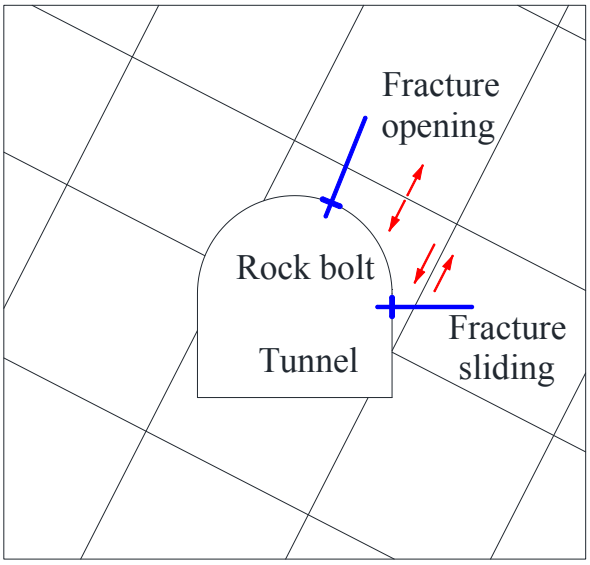

Fig. 5. Failure mode of rebar bolts under large deformation conditions

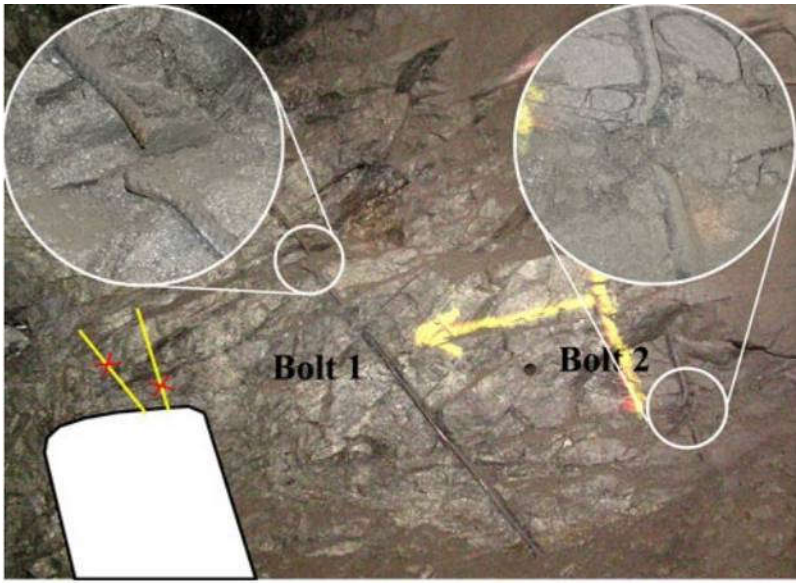

Fig. 6. Failure of two cement-encapsulated rebar bolts (from Li 2010)

The TCC Yielding rock bolt, however, has a long smooth section between inner and outer anchoring segment, which can easily detach from the grout under pull loading and freely deform when subjected to rock dilation. Opening or sliding of a single fracture will induce a relative uniform load and strain distribution in the bolt, as shown in Fig. 7b. The strain induced in the new bolt is remarkably lower than conventional bolt, because that the displacement of the rock mass is distributed over the entire length of free-elongating segment. The smooth segment can provide large deformation to accommodate rock dilations. The amount of deformation is in proportion to the length of smooth segment and can be fully adjusted to requirements of specific rock mass environment. With the new bolt, the energy released by the rock deformation process is absorbed during the plastic deformation of the steel bar.

In order to express the deformation ability of the new bolt, not only the bonding capacity between inner anchoring segment and rock mass should be larger than the maximum load of the bolt. Meanwhile, it should be ensure that failure would not happen at the steel rod of inner anchoring segment and outer anchoring segment during the stretch of smooth segment. These two critical issues are successfully resolved by two additional anchors in TCC Yielding rock bolt. As shown above, the coupling action of tension to the rough rod and compression on the inner additional anchor by grout in different positions increases the ultimate bearing capacity of inner anchoring segment greatly. The stress dispersion structure makes the load of rough rod lower than the load of smooth rod, therefore the premature failure of steel rod at inner anchoring segment is

prevented. Similarly, the additional anchor at the outer end of the rock bolt can also reduce the force borne by bolt plate and thread segment.

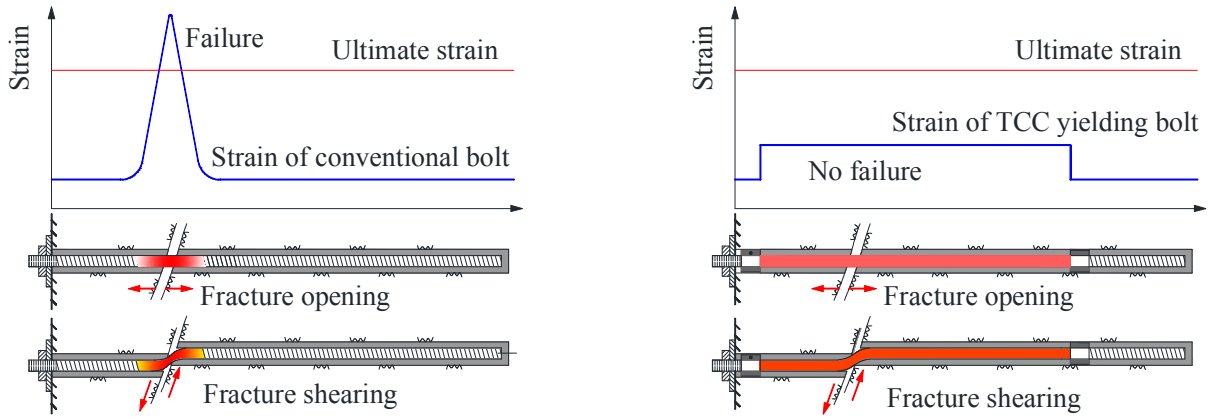

a. Conventional rock bolt b. TCC Yielding rock bolt

Fig. 7. Sketches illustrating the strain induced in bolt when subjected to opening or shearing of single fracture

The new bolt is designed to dissipate large amounts of energy liberated from the rock mass deformation and therefore suitable for extreme conditions at depth. After large deformations, the new rock bolt is still able to provide a reserve load to the rock mass. The behavior of the new bolt allows the users to pre-design the support system to the expected rock deformation, and therefore optimizing the rock reinforcement design to facilitate greater levels of safety and productivity.

4.4 Test on the load capacity of tension and compression coupled anchor

Direct quasi-static pull tests are performed to examine the load capacity of tension and compression coupled anchor at the end of the new bolt. The performance of most commonly used conventional tensile anchor and the new anchor subjected to a pull load will be test in these experiments.

4.4.1 Test procedures

The arrangement of the tests are shown in Fig. 8. The rock bolt specimens are pulled on a test rig specially constructed for bolt testing. The test rig mainly consists of a steel tube, with a length of 460 mm. The steel tube is 74/54 mm in outer/inner diameter. The internal surface of the tube is shallow grooved to simulate the roughness of the borehole wall. The steel tube is filled with concrete to simulate the rock mass. A borehole with a

diameter of 30mm is drilled to install the bolt as shown in Fig. 9.

Two new bolt specimens and two conventional bolt specimens are tested. All the bolt specimens used in the tests are made from 16Mn steel, with a yielding strength of 345 MPa and tensile strength of 570 MPa. The diameters of the rod and anchor are 22mm and 26 mm respectively. The total length of the steel rod is 500 mm, with an anchorage length of 200mm as shown in Fig. 10. Before encased in the concrete, the strain gauges are plastered in the slots at both sides of the bolt specimens. The specimens are encapsulated in the steel tubes by 42.5R cement grout. The cement/sand/water/retarder ratio is 1:1:0.25:0.005. The seven days uniaxial compressive strength of the cement grout is 50~60MPa.

During the test, one end of the steel tube is fixed, and a tensile force is applied on the rock bolt specimen by the testing machine. The specimens are loaded at a speed of 2mm per minute. The displacement of the bolt is recorded relative to the applied load during testing. The strain distribution along the specimens is recorded by the strain gauges to calculate the distribution of axial force and shear stress. All the measurement instruments are connected to an automatic data acquisition system.

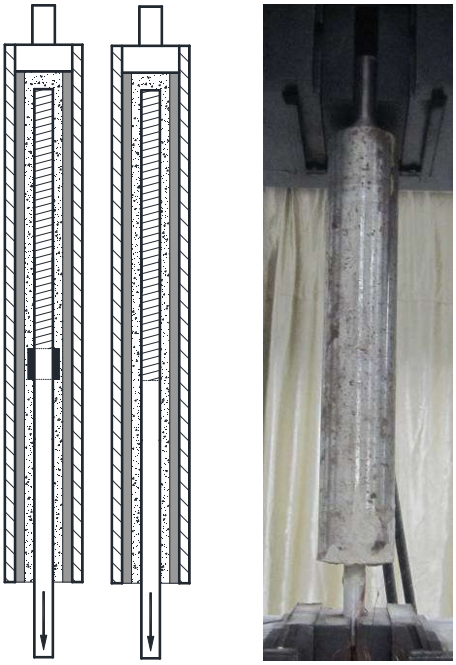

Fig. 8. Arrangement of the pull tests

Fig. 9. Preparation of test specimens

Fig.10. Two specimens used in the tests

4.4.2 Test results and discussions

Fig. 11 shows the photos of different specimens after failure. The failure modes of two type specimens are quite different. The failure happens at the bolt-grout interface for the conventional rock bolt, which illustrates that the load capacity of the tensile anchor in conventional rock bolt is not enough. While, the TCC Yielding rock bolt breaks at the rod itself, illustrating that the load capacity of the new anchor is larger than the ultimate strength of the steel rod.

The load–displacement curves of four samples in the tests are presented in Fig. 12. The load of the conventional rock bolt decreases sharply after the peak value of 140kN. The TCC Yielding rock bolts yield at about 140kN, but they do not failure until the peak value of 200kN. The failure characteristic of TCC Yielding rock bolt specimens in this test is quite like the failure of a steel rod under a tensile load, which illustrating that the performance of the tension and compression coupled anchor is excellent and no shear failure happens.

The shear stress distribution of conventional rock bolt and TCC Yielding rock bolt at the bolt-grout interface are shown in Figs. 13 and 14, respectively. The results show that the shear stress of the conventional rock bolt is much larger than the TCC Yielding rock bolt under similar load conditions. This behaviour illustrates that the inner additional anchor can reduce the shear stress at bolt-grout interface effectively.

Fig. 11. Different failure modes in the test

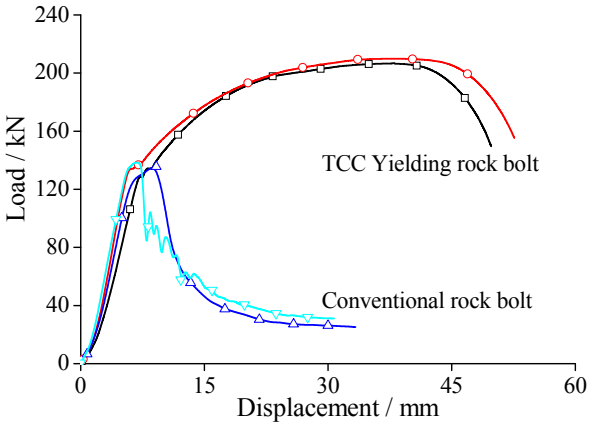

Fig. 12. Load versus displacement curves from different samples

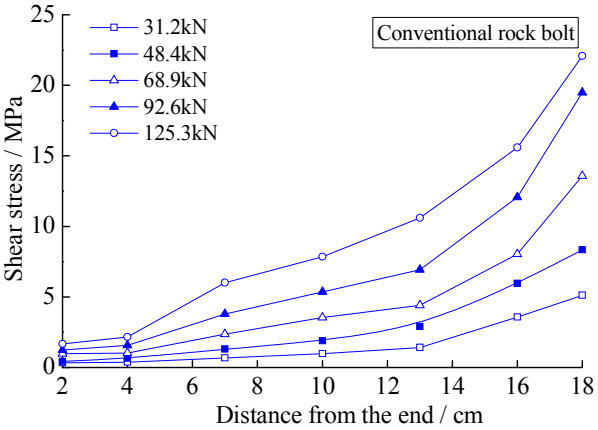

Fig. 13. Shear stress distribution of conventional rock bolt at the bolt-grout interface

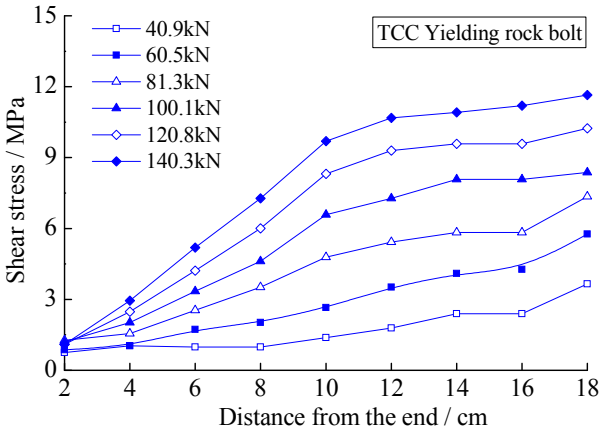

Fig. 14. Shear stress distribution of TCC Yielding rock bolt at the bolt-grout interface

4.5 Test on the large deformation characteristics under pull condition

Direct quasi-static pull tests are performed to examine the deformation performance of the new bolt. Two series tests are prepared in this study. The performance of the conventional bolt and the new bolt subjected to fracture opening will be test in the first series tests. The second series tests are performed to develop a method to predict the deformation ability of the new bolt.

4.5.1 Test procedures

The arrangement of the first series tests is shown in Fig. 15. The samples are also pulled on a test rig specially constructed for bolt testing. The test rig consists of two steel tubes, with the lengths of 445 mm and 700 mm, respectively. The steel tubes are 60/40 mm in outer/inner diameter.

Four bolt specimens are tested. The bolt specimens used in the tests are also made from 16Mn steel. The diameters of the rod and anchors are 22mm and 26 mm respectively. Short samples had to be used due to the space limitation of the test machine. The total length of the steel rod is 1150 mm, with an anchorage length of 300mm and smooth length of 760mm. The diameter of conventional bolt specimen is 20mm. All samples are fully encapsulated in the jointed steel tubes by 42.5R cement grout. Fig. 16 shows a new bolt specimen, a conventional bolt specimen, and test rigs used in the testing. During the test, one of the steel tubes is fixed, and a tensile force is applied on the other one by the testing machine. The samples are also loaded at a speed of 2mm per minute.

The percentage elongation of the steel used in industry is calculated from test of steel

bar with specified length and diameter (δ5 and δ10). It can't be used for predicting the deformation ability of the new bolt, so the second series tests are conducted under the same condition of first series tests. In these tests, the lengths of smooth segment are 110mm, 220mm, 440mm×2, 660mm×2.

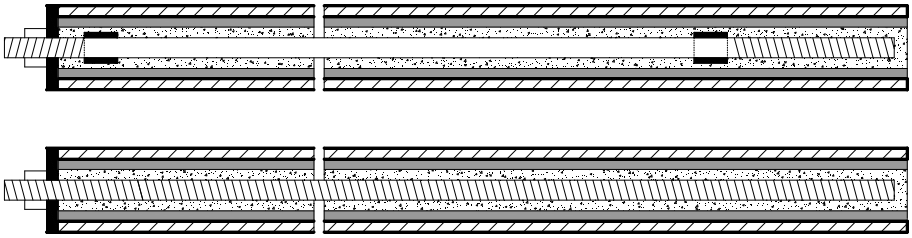

Fig. 15. Arrangement of the large deformation pull test

Fig.16. Samples used in the tests

4.5.2 Test results and discussions

(1) Deformation characteristics

Fig. 17a shows the photos of conventional bolt specimens after failure, and 17b shows the new bolt specimens during failure. The load–displacement curves of four specimen s in the tests are presented in Fig. 18.

(a) Conventional bolt specimen

(b) New bolt specimen

Fig. 17. Failure modes of two different specimens

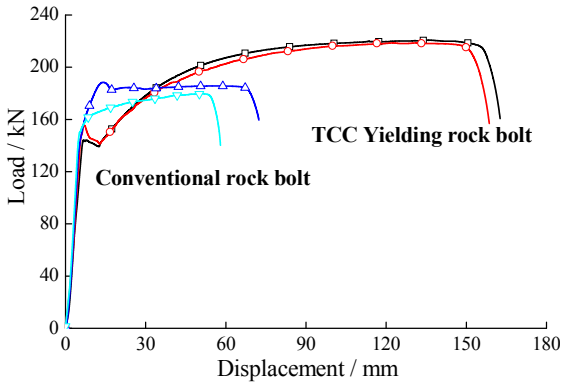

Fig. 18. Results from the first series tests

The failure mechanism of conventional fully grout bolt is verified in these tests. As shown in Figures 18, the load of conventional bolts increases quickly in the early stage before reaching the yielding load. And then, the load will almost remain constant and the displacement increase to approximately 70mm before failure occurred. This phenomenon is probably because of the couple action of steel yielding and decoupling of bolt and grout interface. However, an elongation of 70 mm is far from enough for high stress rock masses.

The results of new bolt samples show that the elongation is 160mm for a 760mm long smooth segment, which is greatly larger than conventional bolts, indicating that the deformation characteristics of the new bolt can be well expressed. The new bolt also has a large load capacity equal to the tensile strength of steel material. The energy absorbed by rock bolt is represented by the area under the load–displacement curves. It is obvious that the new bolt can absorb much more energy liberated from rock mass.

(2) Predicting of the elongation

The elongation of the new bolt is 160mm when the length of smooth segment is 760mm. However, the length of rock bolt is usually 2500~5000mm when used in-site, and the corresponding length of smooth segment will be 2000~4000mm. The load–displacement curves of the six samples in the second series tests together with the two new bolts in first series tests are presented in Fig. 19.

As shown in Fig. 19, the ultimate displacement of the new bolt is composed of four parts, namely the deformation in elastic stage, yield stage, hardening stage and necking stage. The deformation in the first three stages is roughly proportional to the length of smooth segment, while the necking stage remains unchanged basically. Therefore, the

relationship between bolt elongation and length of smooth segment may be represented by a linear function on an arithmetic scale.

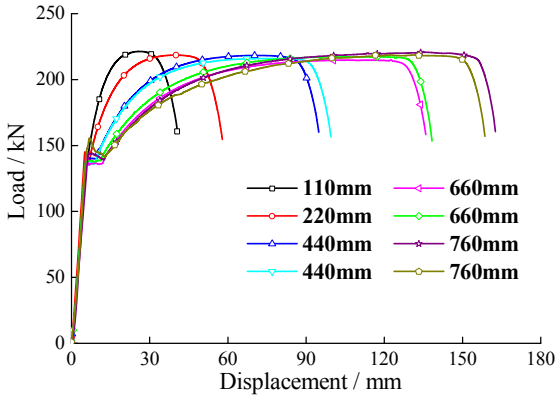

Fig. 19. Results from the second series tests

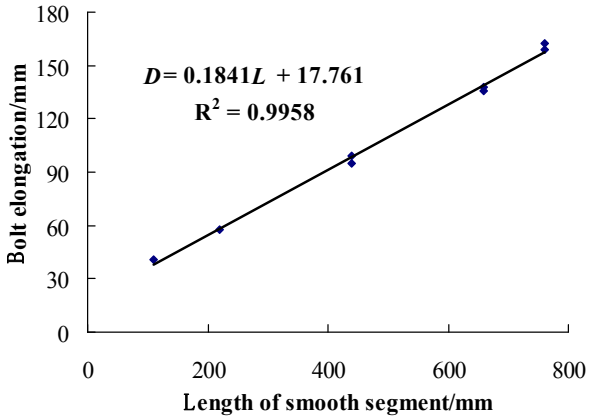

Fig. 20. Relationship between maximum deformation and length of smooth section

As shown in Fig. 20, the results verified above inference, and the relationship between them can be expressed as Eq. (1).

$$D = a * L + b \tag{1}$$

Where D is the bolt elongation, L is length of smooth segment, a and b are parameters associated with properties of the steel material and bolt diameter. According to results in this study, a and b are determined as 0.1841 and 17.761 by linear regression method. The values of R^2 are greater than 0.9958, indicating that the results are accurate enough. According to above formula, the bolt elongation will be 386~754mm for 2000~4000mm (bolt length 2500~5000mm) long smooth segment, which is enough for the deformation of high stress rock mass.

(3) The load at the rock bolt plate

Generally, the conventional rock is easy to be failure at the outer thread segment under large pull loading, because that the sectional area is reduced during the process of thread, resulting that the load capacity of thread segment is lower than the other segment. In order to exert the deformation ability of the smooth segment in the new bolt, it should be ensure that failure would not happen at the outer anchoring segment during the stretch of smooth segment. The additional anchor at the outer end of the rock bolt is designed to reduce the force borne by bolt plate and the thread segment, which has been shown in Fig. 2.

In the first series tests, the axial force at the outer thread segment is measure by two strain gages as shown in Fig. 21. The test results together with the maximum axial force of the new rock bolt is shown in Fig. 22. The results show that the axial force at the outer thread segment is only about 60% percent of the maximum axial force, illustrating that the stress dispersion effect of outer additional anchor is excellent.

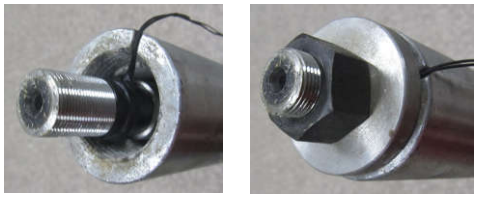

Fig. 21. Test of bolt axial force at plate

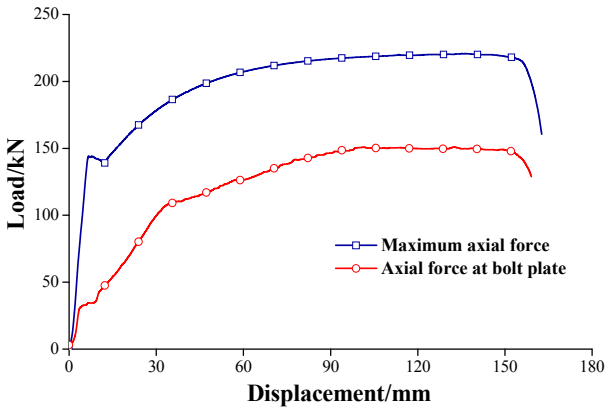

Fig. 22. Axial forces of the TCC Yielding rock bolt at different positions

4.6 Test on the large deformation characteristics under shear condition

The previous shear tests of rock bolts mainly aimed to study their effect in the reinforcement of rock joints (Grasselli 2005; Jalalifar et al. 2006; Li et al. 2016a; Li et al. 2016b). Chen et al. (2015) conducted a series of shear tests to examine the performance

of D-Bolt, which is a meaningful indicator to test the deformation characteristics of the TCC Yielding rock bolt. The shear tests of TCC Yielding rock bolt is designed based on their works.

4.6.1 Test procedures

Direct shear tests are performed to examine the performance of the new bolt under shear conditions. The performance of the conventional bolt and the new bolt subjected to fracture sliding will be tested. Small samples had to be used due to the space limitation of the shear testing machine. The conventional rock bolt is simulated by a thread bar, and the new bolt is simulated by a smooth bar made from S45C steel.

The arrangement of the test is shown in Figs. 23 and 24. The bolt specimen is installed in a block with a fracture in the middle. The block is made of rock like material, with a seven days uniaxial compressive strength of 70MPa to simulate the medial strength rock. The plaster/water/retarder ratio is 1:0.2:0.005. The dimensions of the block is designed as L=200mm, W=100mm and H=90 mm, according to the space of shear testing machine. Generally, the support area of a single rock bolt in engineering practice is 1000mm×1000mm, and the bolt diameter is 22mm, while the support area of a bolt specimen in this test is 100mm×200mm. The bolt diameter is identified as 3mm according a similarity ratio of 7:1. A borehole with a diameter of 5mm is drilled to install the bolt specimen. The bolt specimens are encapsulated in the borehole by the same rock like material as the block. The total length of the bolt specimen is 100 mm, with 5mm exposed at both ends. Two steel plates with a thickness of 5mm is placed on both sides of the block to protect the bolt when a normal stress is applied.

During the test, the normal stress is set as 1MPa. The lower part of the block is fixed, and a force is applied on the upper part by the testing machine. The samples are loaded at a shear speed of 0.5mm per minute. The shear displacement and shear stress of are recorded during testing.

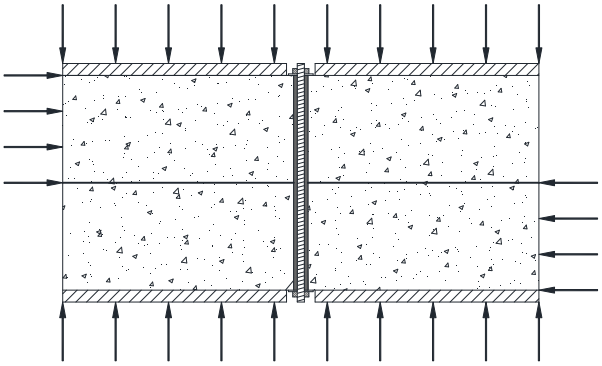

Fig. 23. Arrangement of the shear test

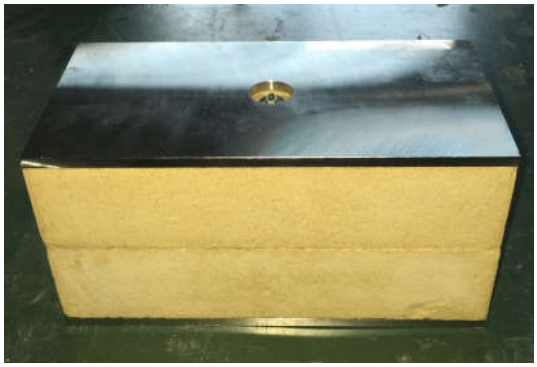

Fig.24. Samples used in the tests

4.6.2 Test results and discussions

Fig. 25 shows the photos of different bolt specimens before and after failure. The failure region in the block caused by different bolt specimens is shown in Fig. 26. The failure modes of two type specimens are also quite different as shown in Figs 25 and 26. The conventional bolt specimen exerts a remarkable shear failure, and the failure region in the rock block is quite small. The new bolt specimen exerts a remarkable tension failure, and the failure region in the rock block is much larger than the conventional bolt specimen. This behaviour implies that the stress and strain concentration of the conventional bolt specimen at the fracture is quite serious. While, the smooth section of the new bolt specimen can deform freely to accommodate the sliding of fracture.

The shear stress-displacement curves of different bolt specimens are shown in Fig 27. The suddenly drop in the shear stress-displacement curves implied that the bolt is broken at this position. The results implies that the maximum shear displacement of the new bolt specimen is much larger than the conventional bolt specimen. The behaviour of new bolt specimen is promising a better ability to accommodate the large displacement sliding of fracture in the engineering practice. The shear stress of the

fracture is raised to 0.64MPa from 0.37MPa for the conventional bolt specimen. However, the maximum shear stress in the case of new bolt specimen is 0.86MPa. The rising of shear stress for the new bolt specimen is owing to two aspects. The first is the direct shear resistance of bolt itself, which is similar with the conventional bolt specimen. The other reason is that the axial force of the bolt specimen increases with the sliding of the fracture because of the smooth surface. The axial force is applied on the rock block, which increased the normal stress of the fracture. So the shear stress increasing of the new bolt specimen is much larger than the conventional bolt specimen.

Fig. 25. Specimens before and after the shear tests

(a) (b)

Fig. 26. Failure modes of two different specimens: (a) Conventional bolt specimen (b) New bolt specimen

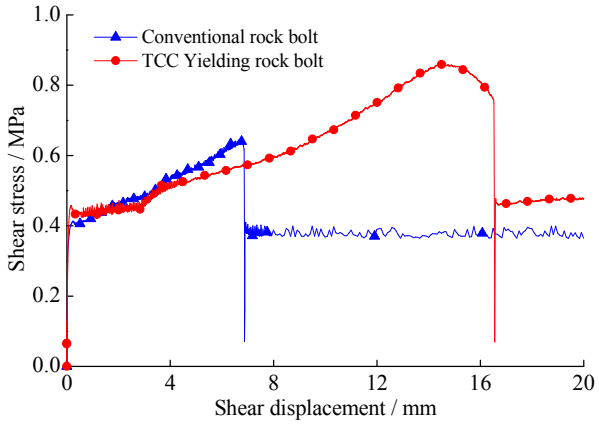

Fig. 27. Shear behaviour of different bolt specimens

4.7 Conclusions and Outlook

A new rock bolt for energy-absorbing applications is proposed in this paper. The new bolt consists of a steel rod and two additional anchors. The steel rod is a round shape bar with varying surface conditions. The inner segment is processed into rough surface, while the middle of the rod has smooth surface. Two additional anchors were welded on both ends of smooth segment. The bolt is fully encapsulated with either cement or resin grout in a borehole. The rough rod and the inner additional anchor are firmly fixed in the bottom of the borehole, while the smooth bar has no or very weak bonding to the grout, which can stretch to accommodate rock dilatation.

Direct quasi-static pull tests are performed to examine the load capacity of tension and compression coupled anchor in the new bolt. The results show that the coupling action of tension to the rough rod and compression on the inner additional anchor by grout in different position can increase the ultimate bearing capacity of inner anchoring segment greatly. The shear stress of the TCC Yielding rock bolt is much smaller than the conventional rock bolt under similar load conditions, which illustrates that the inner additional anchor can reduce the shear stress at bolt-grout interface effectively.

The performance of the conventional bolt and the new bolt subjected to fracture opening is tested. Results show that the load and strain concentration could result in premature failure of conventional rock bolt, as it is strongly bonded to the grout. However, the smooth segment of TCC Yielding bolt can easily detach from the grout under pull loading and provide a large deformation to accommodate rock dilations. The stress dispersion structure makes the load of rough rod lower than the load of smooth rod, therefore the premature failure of steel rod at inner and outer anchoring segment is prevented. A simple method is developed to predict the deformation ability of the new

bolt. The bolt elongation will be 386~754mm for 2500~5000mm long bolt, which is enough for high stress rock masses.

Shear tests are performed to examine the performance of the new rock bolt and the conventional rock bolt subjected to fracture sliding. The conventional bolt specimen exerts a remarkable shear failure, while the new bolt specimen exerts a remarkable tension failure. The stress and strain concentration of the conventional bolt specimen at the fracture is quite serious. While, the smooth section of the new bolt specimen can deform freely to accommodate the sliding of fracture. The maximum shear displacement of the new bolt specimen is much larger than the conventional bolt specimen, which is promising a better ability to accommodate the large displacement sliding of fracture in the engineering practice. The increasing of shear stress for the new bolt specimen is owing to the shear resistance of bolt itself and the contribution of normal stress on the fracture.

Compared with structural components sliding type bolts, the new bolt not only has a larger load capacity which is equal to the tensile strength of steel material, but also has a simpler structure which will inherently reduce the cost. Compared with other steel deformation type bolts, the anchor structure of the new bolt is promising to have more stable load bearing capacity. Meanwhile, the good performance of the new bolt is independent of the prevailing installation and interface conditions.

The rock bolts are loaded in situ either statically by time-dependent rock dilation, or dynamically by rock burst. In the case of rock bursting, the bolt would be loaded in a more complicated manner than static loading condition. The dynamic tests should be done to examine the shock-resistant performance and energy absorption capacity of the new bolt subjected to dynamic loading in the future.

References

Amusin B (1998) Ground control and design of deep mine openings. Int J Rock Mech Min Sci 35: 1365-1609

Ansell A (2005) Laboratory testing of a new type of energy absorbing rock bolt. Tunn Undergr Sp Technol 20: 291-300

Aziz N, Craig P, Mirzaghorbanali A, Nemcik J (2016) Factors influencing the quality of encapsulation in rock bolting. Rock Mech Rock Eng 49: 3189-3203

Chantale D, Benoit V (2012) Technical information data shifts. Natural Resources, Canada, Version, 05-29

Chen Y, Li C (2015) Performance of fully encapsulated rebar bolts and D-Bolts under combined pull-and-shear loading. Tunn Undergr Sp Technol 45: 99-106

Cook N, Ortlepp W (1968) A yielding rock bolt. Chamber of Mines of South Africa. Research Organization Bulletin, no. 14

Gillerstedt P (1999) Full scale pull and shear laboratory test of yielding rock bolts. Proceedings, Rock Mechanics Meeting in Stockholm 1: 105-119

Grasselli G (2005) 3D Behaviour of bolted rock joints: experimental and numerical study. Int J Rock Mech Min Sci 42: 13-24

He M, Gong W, Wang J, Qi P, Tao Z, Du S, Peng Y (2014) Development of a novel energy-absorbing bolt with extraordinarily large elongation and constant resistance. Int J Rock Mech Min Sci 67: 29-42

Hoek E (1995) Support of underground excavation in hard rock. Balkema, Rotterdam 1-10

Hoek E (2007) Practical rock engineering, Chapter 1, The development of rock engineering, Available on line at: http://www.rocscience.com/hoek/Hoek.asp, 2012.10.20

Huang X, Ma L, Chen S, Kong Y (2014) Distribution characteristics and time-space effects of internal force of prestressed anchor rod. Chin J Rock Mech Eng 36(8): 1521-1525 (in Chinese)

Jager A (1992) Two new support units for the control of rockburst damage. Rock support in mining and underground construction 621-631

Jalalifar H, Aziz N, Hadi M (2006) The effect of surface profile, rock strength and pretension load on bending behaviour of fully grouted bolts. Int J Geotech Geol Eng 24: 1203-1227

Li C (2010) A new energy-absorbing bolt for rock support in high stress rock masses. Int J Rock Mech Min Sci 47: 396-404

Li C (2012) Performance of D-bolts under static loading. Rock Mech Rock Eng 45(2): 183-192

Li L, Hagan P, Saydam S, Hebblewhite B, Li Y (2016) Parametric study of rockbolt shear behaviour by double shear test. Rock Mech Rock Eng DOI 10.1007/s00603-016-1063-4

Li S et al. (2011) Experimental study of anchoring effect of discontinuous jointed rock mass under uniaxial tension. Chin J Rock Mech Eng 30(8): 1579–1587 (in

Chinese)

Li S et al. (2012) Comparative field test study of pressure relief anchor box beam support system in deep thick top coal roadway. Chin J Rock Mech Eng 31(4): 656–666 (in Chinese)

Li X, Aziz N, Mirzaghorbanali A, Nemcik J (2016) Behavior of fiber glass bolts, rock bolts and cable bolts in shear. Rock Mech Rock Eng 49:2723-2735

Ortlepp W (2000) Observation of mining-induced faults in an intact rock mass at depth. Int J Rock Mech Mining Sci 37: 423-436

Ortlepp W (2001) The behaviour of tunnels at great depth under large static and dynamic pressures. Tunn Undergr Sp Technol 16: 41-48

Salzburg (2009) In-Situ pull testing of a yieldable rock bolt, Roofex. Controlling Seismic Hazard and Sustainable Development of Deep Mines 1081-1090

Stillborg B (1994) Professional users handbook for rock bolting, 2nd ed. Trans Tech Pub

Srivastava LP, Singh M (2015) Effect of fully grouted passive bolts on joint shear strength parameters in a blocky mass. Rock Mech Rock Eng 48: 1197-1206

Wang G, Wu X, Jiang Y, Huang N, Wang S (2013) Quasi-static laboratory testing of a new rock bolt for energy-absorbing applications. Tunn Undergr Sp Technol 38: 122-128

Windsor C, Thompson A (1992) A new friction stabilizer assembly for rock and soil reinforcement applications. Rock support in mining and underground construction, Rotterdam 523–529

Zhang A, Hu Y (2009) Anchoring effect of pressure-type anchor rods on anchored section, Chin J Rock Mech Eng 31(2): 271-275 (in Chinese)

Zhang J, Tang B (2002) Hyperbolic function model to analyze load transfer mechanism on bolts, Chin J Rock Mech Eng 24(2): 188-192 (in Chinese)

5 Influence of the joint roughness on the shear behaviour of fully encapsulated rock bolt

5.1 Introduction

Rock mass stabilization by bolting is an effective and economical means, which has been used for more than a century in mining and tunnelling. Rock bolts develop their strength during the convergence of rock mass, especially in the jointed rock mass (Srivastava and Singh, 2015). Bolted joints can be subjected to two categories of movements, either to opening in a direction perpendicular to the plane or to shear displacements occurring in the plane (Li and Hagan, 2016a). Generally, much more attention is paid to the pull-out capacity of rock bolt to prevent the opening of rock joint. The shear resistance of rock bolt is always not considered in the support designing. However, a case study by McHugh and Signer (1999) indicated that shear loading contributed significantly to the failure of anchoring systems. A high proportion of rock bolts have been found to fail duo to the shearing of high stress rock masses (Li, 2010).

The shear performance of rock bolt is just as significant as tensile performance. Many experiments have been performed to study the mechanical behaviour of rock bolts in resisting the shear force. Some factors that can influence the shear behaviour were studied systematically, including bolt type (Haas, 1976; Grasselli, 2005; Chen and Li, 2015b; Li and Aziz, 2016), bolt diameter (Spang and Egger, 1990; Grasselli, 2005), bolt surface profile (Jalalifar et al. 2006; Jalalifar et al. 2010a), bolt material (Dight, 1982; Ferrero, 1995), bolt inclination (Bjurstrom, 1974; Haas, 1976; Spang and Egger, 1990; Grasselli, 2005; Chen and Li, 2015a), bolt pretension (Bjurstrom, 1974; Haas, 1976; Ferrero, 1995; Jalalifar et al. 2006; Jalalifar et al. 2010a; Li and Aziz, 2016), rock strength (Spang and Egger, 1990; Ferrero, 1995; Jalalifar et al. 2006; Chen and Li, 2015a) and normal pressure (Haas, 1976; Spang and Egger, 1990). Analytical studies and numerical simulation were also conducted to describe the behaviour of rock bolts inserted in rock joint (Spang and Egger, 1990; Ferrero, 1995; Marence and Swoboda, 1995; Pellet and Egger, 1996; Jalalifar et al. 2010a; Jalalifar et al. 2010b; Song et al. 2010; Deb and Das, 2014; Lin et al. 2014; Li and Nemcik, 2015; Li and Hagan, 2016).

Through a systematic variation of the bolting parameters, their influence on the shear resistance of rock joints has been quantified. Formulas have been developed for

the evaluation of the bearing capacity of rock bolts. However, almost all the tests introduced above, except Spang and Egger (1990), were conducted on smooth rock joints, which is not exactly inconsistent with the field engineering practice. In nature, joints without any geometric irregularities are very rare. Joint roughness is one of the most important factors for understanding and estimating the shear behavior of a rock joint (Tse and Cruden DM, 1979; Lee et al. 2001; Wang et al. 2016). The strength and deformability of joints are closely related to the surface roughness. It is unacceptable to ignore the influence of joint roughness on the support effect of rock bolt.

To study the influence of joint roughness, Spang and Egger (1990) carried out a test with symmetrically indented shear surface. He found that the shear surfaces with a considerable angle of dilatancy show a stiffer response to shear displacements than smoother ones. This work is of great significance, but it was limited in the symmetrically indented shear surface, which is also different with the natural rough joints. Only one case about the roughness was conducted in their tests, namely the symmetrically indented shear surface with a dip angle of 17°. Despite these studies, the influence law of surface roughness on the shear resistance and shear displacement of rock bolt is still not completely revealed. The understanding of shear behaviour of rock bolt inserted in rough joint is still in its infancy and yet to be fully explored.

The aim of this paper was to contribute to a better understanding of the influence of joint roughness on the support effect of rock bolt in resisting shear displacement. Eighteen direct shear tests were performed on rough rock joints with and without rock bolt. The effectiveness of rock bolts along preexisting fracture surfaces was determined, and a mathematical model was proposed to predict the shear behaviour of rock bolt in different roughness conditions.

5.2 Test arrangement

Laboratory shear tests were carried out to study the shear behaviour of fully bonded rock bolt under various surface roughness conditions. The parameter of joint roughness coefficient (JRC) is used to express the roughness of joints (Barton and Choubey, 1977). The influence of JRC on the shear resistance and shear displacement will be evaluated.

In the present study of rock bolt shear behaviour, the shear resistance is considered as the most important index. However, the shear displacement of rock joint before bolt failure is more important in high stress conditions, where the large deformation is

inevitable. Therefore, both shear resistance and shear displacement were studied in-depth in these tests.

5.2.1. Testing method

There are two methods of shear testing, single and double shear tests. The double shear testing used a three piece concrete block double shear apparatus to simulate shear behaviour of rock bolts in rock (Grasselli, 2005; Jalalifar et al. 2006; Li and Aziz, 2016). This method can test the shear strength of rock bolt conveniently for large-size rock bolt under smooth joints condition. However, the interaction between the two shear interfaces may cause errors for the rough joints.

The single shear testing method (Haas, 1976; Spang and Egger, 1990; Chen and Li, 2015a) using two piece blocks to simulate shear behaviour of rock bolts inserted in rock joints was adopted in this study. The arrangement of the test is shown in Fig. 1. The fully encapsulated rebar bolt specimen is installed in a block with a rough joint in the middle. The tests were performed using a shear machine under constant normal load (CNL) conditions. The upper part of the block was fixed, and a shear force was applied to the lower part. The shear displacement, shear force, shear stress and normal displacement are recorded during testing.

As the rock mass is in compression state for most case, a normal load is necessary in the shear test. However, the normal load was always not considered in the shear tests of bolted rock joint. It is because the existence of rock bolt make it difficult to apply a precise controlled normal load. In this study, two steel plates with a thickness of 5mm and a 20mm diameter hole in the center was placed on both sides of the block to protect the bolt when a normal load is applied at the top of the block. The steel plates will not affect the shear performance of bolt specimen, as they cannot contact the rock bolt. During the test, a normal stress of 1MPa was applied, which is approximately 2.5% of the UCS for the rock-like material. The samples are loaded at a shear speed of 1.0mm per minute.

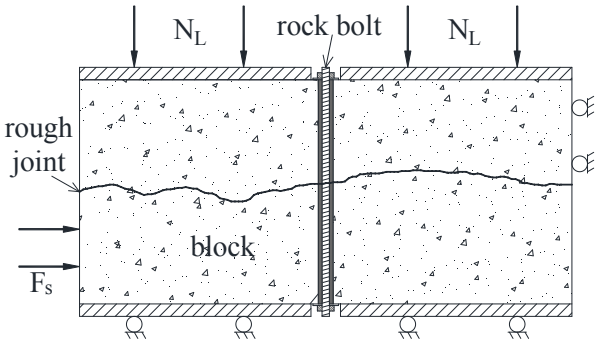

Fig. 1. Arrangement of the shear test

In order to enable comparisons among test results obtained with different bolt diameters or steel qualities, the following dimensionless values defined by Spang and Egger (1990) are used:

$$f_T = (T\text{-}T_N)/P \quad (1)$$

$$f_s = s/d_b \quad (2)$$

where T = shear force obtained in the test, T_N = shear strength of the natural unbolted joint, P = maximum tension load of the bolt, s = shear displacement obtained in the test and d_b = bolt diameter.

5.2.2. Bolt and rock specimens

To conduct experimental studies on rough rock joints, it is necessary to prepare identical samples using a molding method. As shown in Fig. 2, six standard roughness profiles developed by Barton and Choubey (1977) were selected for the artificial rock joints. As a comparison, two tests were also conducted on the smooth joints. Small samples had to be used due to the space limitation of the shear testing machine and the difficulty in manufacturing large-size rough joints. It is acceptable as the aim of this work is to study the influence law of surface roughness on the shear performance of rock bolt. According to the laboratory and field shear tests carried out with bolt diameters of 8, 10, and 40 mm by Spang (1990), the dimensionless values of the shear force and shear displacement do not depend on the bolt diameter.

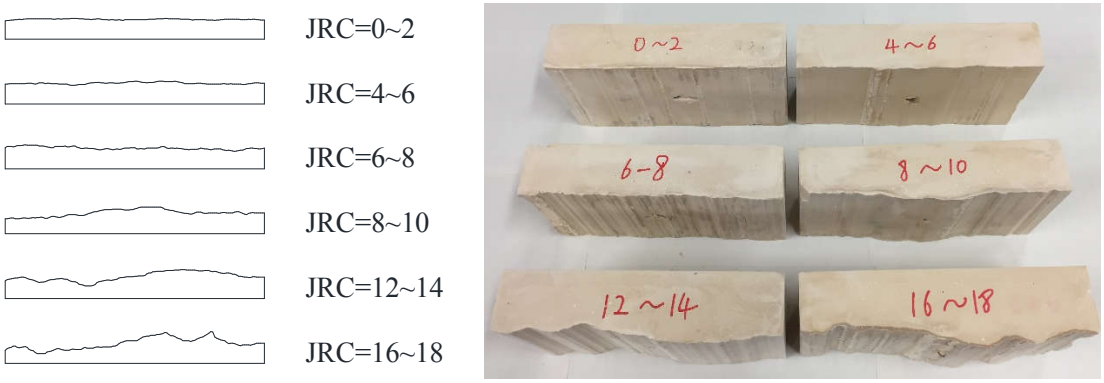

Fig. 2. Standard JRC profiles (from Barton and Choubey, 1977) and part of the specimens used in the tests

All specimens used in the shear tests are 100 mm in width, 200 mm in length and 90 mm in height and made of mixtures of plaster, water and retardant with weight ratios of 1: 0.2: 0.005. Table 1 shows the physical properties of these rock-like specimens. The fully encapsulated rebar bolt is simulated by a thread bar made of S45C steel. The total length of the bolt specimen is 100 mm, with 5mm exposed at both ends. The bolt diameter is 3 mm with an ultimate tensile strength of 6.25kN. A borehole with a diameter of 5mm is drilled to install the bolt specimen. The grout is also made of mixtures of plaster, water and retardant, while the weight ratios is 1:0.32:0.01 to improve the fluidity. Two shear tests was conducted for every standard roughness profile, namely with and without rock bolt. The effect of the rock bolts lies in the difference of shear strength between them.

Table 1 Physico-mechanical properties of specimens

Physico-mechanical properties	Index	Unit	Value
Density	ρ	g/cm^3	2.066
Compressive strength	σ_c	MPa	38.5
Modulus of elasticity	E_s	MPa	28,700
Poisson's ratio	v	-	0.23
Tensile strength	σ_t	MPa	2.5
Cohesion	c	MPa	5.3
Internal friction angle	φ	°	60

5.3 Test results and discussion

With the increasing of shear displacement, the evolution of shear stress and normal displacement of rock joints with standard roughness profiles are shown in Figs. 3a-8a. The suddenly drops in the shear stress-displacement curves implied that the rock bolts were broken at these positions. The relation of dimensionless values shear force f_T and shear displacement f_s for different standard roughness profiles are shown in Figs. 3b-8b. The shear behavior of smooth joints is shown in Fig. 9 for comparison.

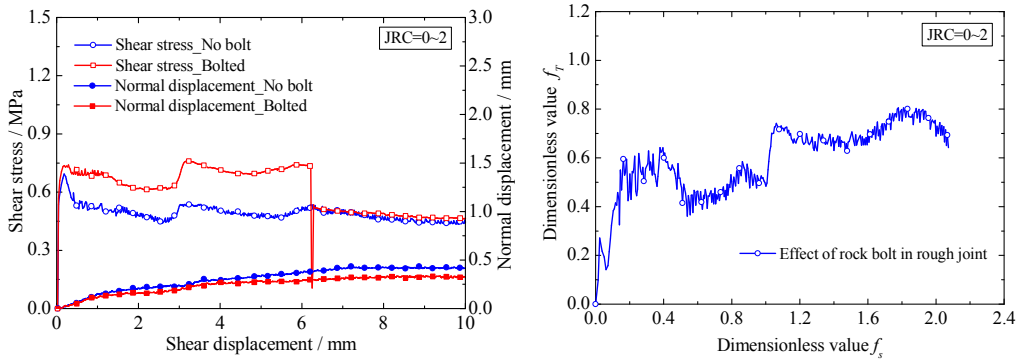

Fig. 3. Shear behavior of standard rough joints for JRC=0~2: (a) shear stress and normal displacement vs. shear displacement; (b) effect of rock bolt

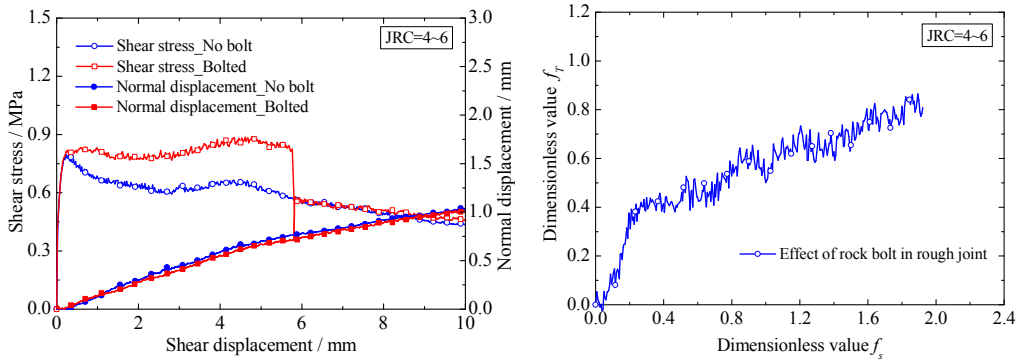

Fig. 4. Shear behavior of standard rough joints for JRC=4~6: (a) shear stress and normal displacement vs. shear displacement; (b) effect of rock bolt

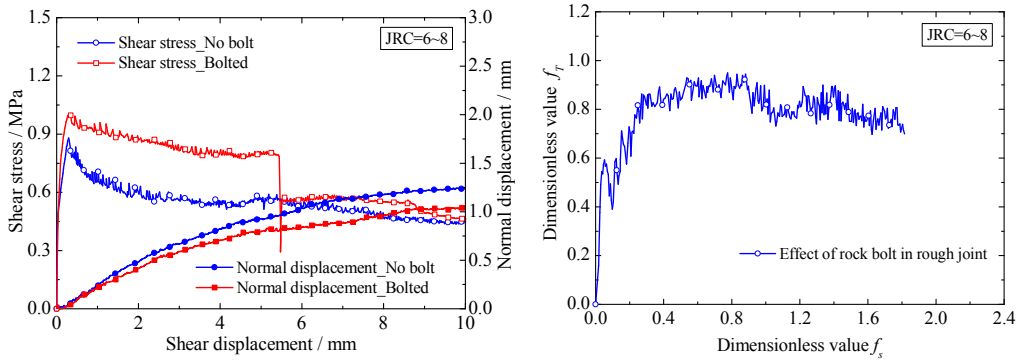

Fig. 5. Shear behavior of standard rough joints for JRC=6~8: (a) shear stress and normal displacement vs. shear displacement; (b) effect of rock bolt

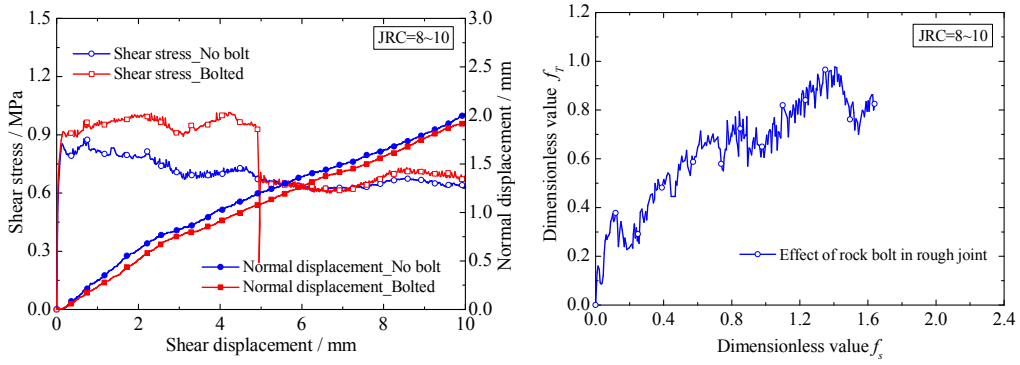

Fig. 6. Shear behavior of standard rough joints for JRC=8~10: (a) shear stress and normal displacement vs. shear displacement; (b) effect of rock bolt

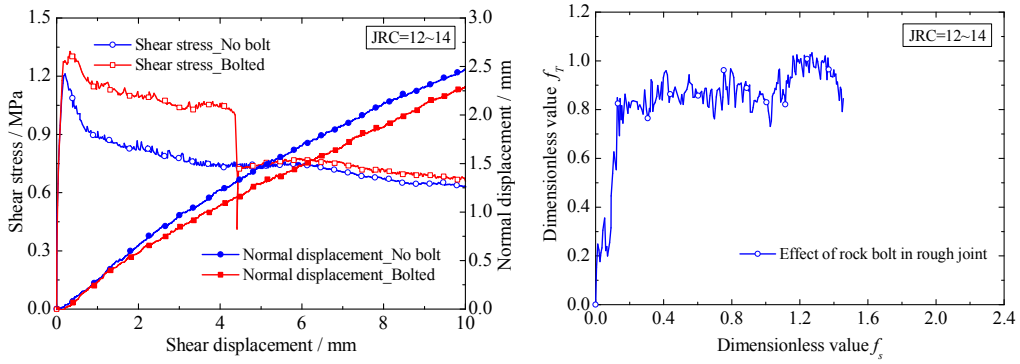

Fig. 7. Shear behavior of standard rough joints for JRC=12~14: (a) shear stress and normal displacement vs. shear displacement; (b) effect of rock bolt

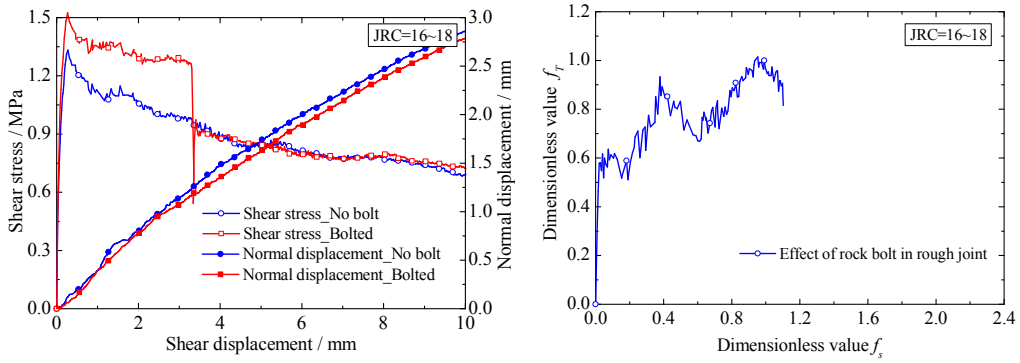

Fig. 8. Shear behavior of standard rough joints for JRC=16~18: (a) shear stress and normal displacement vs. shear displacement; (b) effect of rock bolt

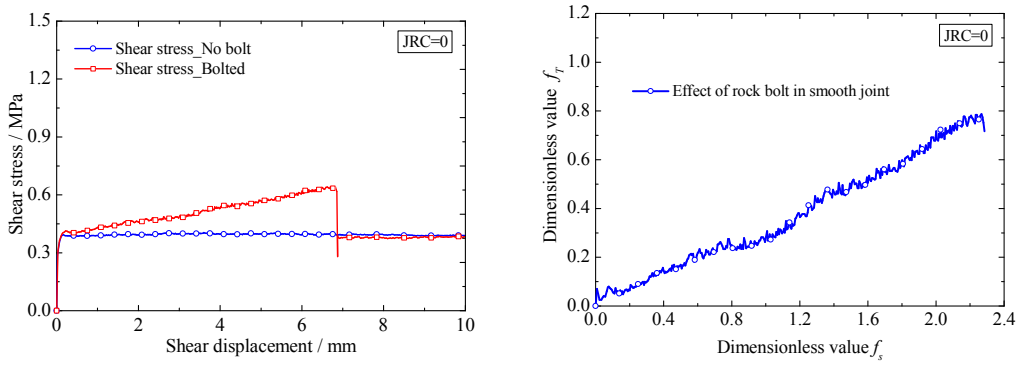

Fig. 9. Shear behavior of smooth joints: (a) shear stress vs. shear displacement; (b) effect of rock bolt

The results indicated that the shear behaviour of rock bolt was strongly influenced by the joint roughness, and quite different with the smooth joints. The shear resistance of rock bolt increased gradually with the increasing of shear displacement for the smooth rock joint. However, the shear resistance reaches to a large value in the early stage for most case of rough joints. The shear stiffness of rock bolt inserted in the rough joints is random for different JRC condition but larger than the smooth rock joints case. After that, the shear resistance of rock bolt showed significant volatility. The peak shear resistance of rock bolt was not always located at the end stage. After the failure of rock bolts, the shear resistance of the rock joints dropped to the same level of no bolt cases, while, no significant change was found in the normal displacement.

As shown in Figs. 3a-8a, the shear dilatancy (normal displacement) of the rough joints increases with the increasing of JRC, which is also influenced by the rock bolts. The shear dilatancy of bolted rock joints was smaller than the ones without rock bolts for the same JRC condition. The differences mainly generate before the failure of the rock bolts. The decrement of shear dilatancy was different in these cases. However, no significant law was found, as the decrement of shear dilatancy caused by the rock bolt was larger for JRC=6~8 and 12~14, smaller for JRC=4~6, and moderate for other cases.

The evolution of maximum shear resistance (dimensionless value f_T) of rock bolt with the joint roughness is shown in Fig. 10. The evolution of maximum shear displacement (dimensionless value f_s) is shown in Fig. 11. The intermediate value of joint roughness coefficient (JRC) for each standard roughness profiles is adopted to construct a mathematical model.

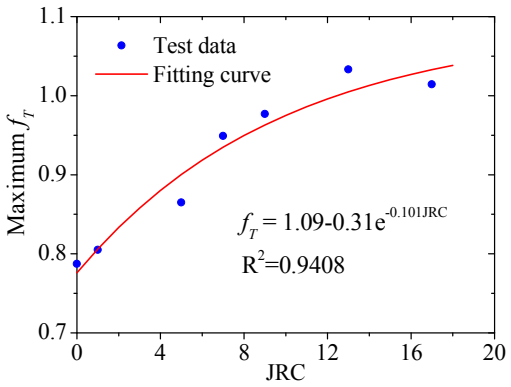

Fig. 10. Relationship between maximum f_T and JRC

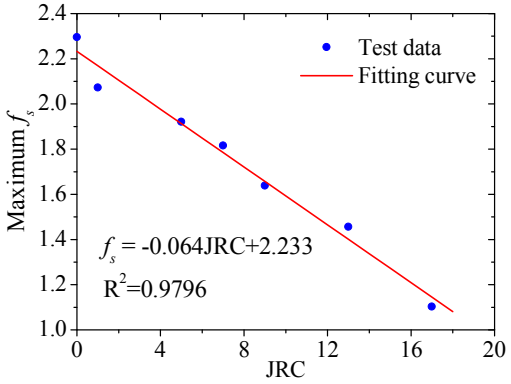

Fig. 11. Relationship between maximum f_s and JRC

As shown in Figs. 10 and 11, the contribution of rock bolt on the shear resistance has a nonlinear relationship with the joint roughness, whereas the maximum shear displacement exhibits good linearity with a high correlation coefficient. The rising of shear resistance of the rock joints is owing to two aspects. The first is the direct shear resistance of bolt itself. The other reason is that the axial force of the bolt specimen is applied on the rock block, which increased the normal stress of the fracture, and then increased the friction force. Obviously, the shear resistance of the rock bolt increase nonlinearly with JRC, but the increase is unsustainable. The maximum shear resistance of rock bolt f_T was evaluate as a negative exponential function of joint roughness coefficient (JRC).

$$f_T = a - b*e^{-c*JRC} \qquad (0 \leqslant JRC \leqslant 20) \tag{3}$$

where the values of a, b, and c were identified as 1.09, 0.31 and 0.101 respectively. The correlation coefficient for this analyses was 0.9408, which implied the correlation quite strong.

The maximum shear displacement of rock bolt decreased linearly with the increasing of JRC. This is because the rock bolt failed in the dual role of shear displacement and normal displacement. A larger JRC value always results in a larger normal displacement, which can be seen in Figs. 3a-8a. The maximum shear displacement of rock bolt (dimensionless value f_s) was evaluate as a linear function of joint roughness coefficient (JRC).

$$f_s = m*JRC+n \qquad (0 \leqslant JRC \leqslant 20) \tag{4}$$

where the values of m, and n were identified as -0.064 and 2.233 respectively. The correlation coefficient for this analyses was 0.9796. The results indicated that the dimensionless mathematical model above can be used to predict the shear behaviour of rock bolt inserted in the rough joint and to estimate the difference with the results of smooth joints normally adopted in other laboratory tests.

5.4 Application in the natural rough joints

Two replicas of natural rough joints were made from the granite planes to verify the applicability of proposed mathematical model for the natural rough joints. The roughness profiles were measured using a laser profilometer. Based on the measured profile lines, the JRC values of natural rough joints are evaluated via the comparison of measured profiles against the standard JRC profiles produced by Barton and Choubey (1977). The mean JRC values were identified as 3.6 and 10.6, respectively, as shown in Fig. 12.

The arrangement of the tests on the natural rough joints is the same with the test of the standard JRC profiles joints. With the increasing of shear displacement, the evolution of shear stress and normal displacement of rock joints with natural roughness profiles are shown in Figs. 13a-14a. The relation of dimensionless values shear force f_T and shear displacement f_s for different specimens are shown in Figs. 13b-14b.

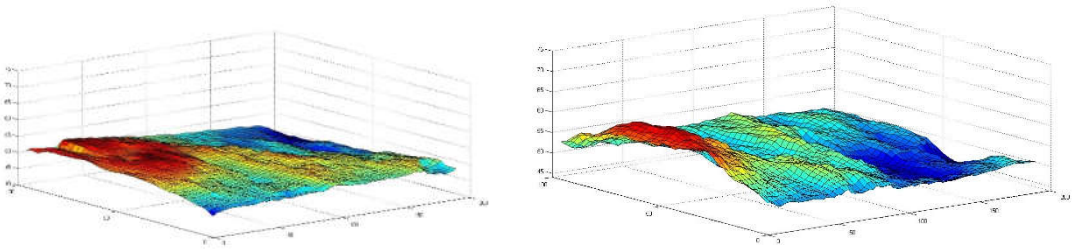

N1 (JRC=3.6) N2 (JRC=10.6)

Fig. 12. Scanning graphs of two natural rough joints

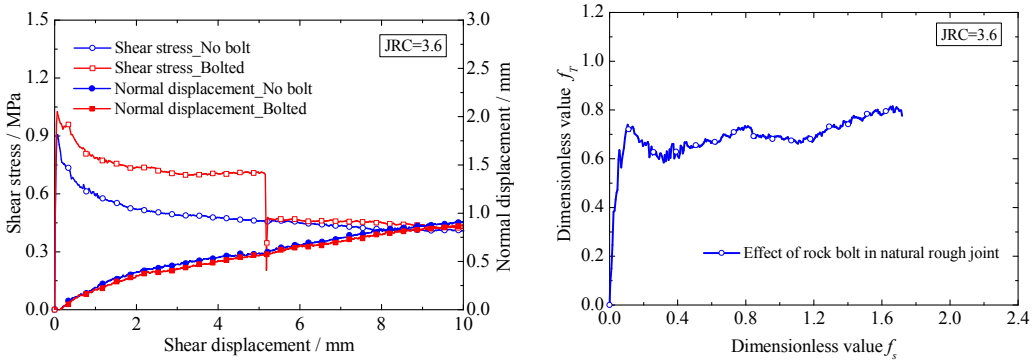

Fig. 13. Shear behavior of natural rough joints for specimens N1 (JRC=3.6): (a) shear stress and normal displacement vs. shear displacement; (b) effect of rock bolt

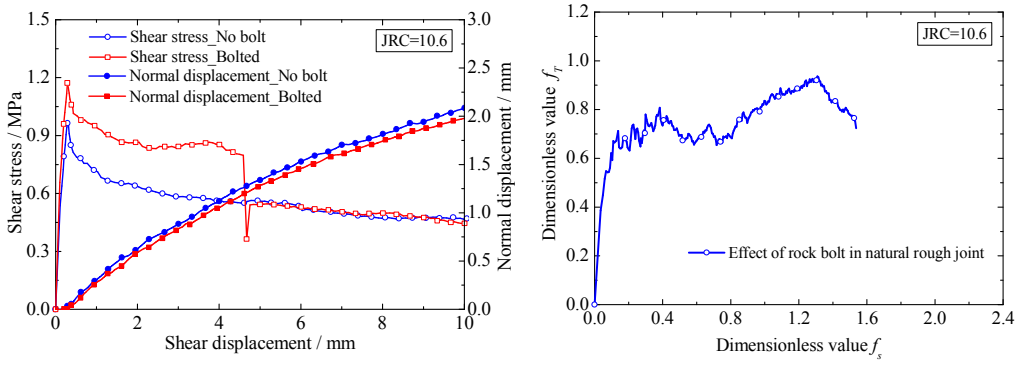

Fig. 14. Shear behavior of natural rough joints for specimen N2 (JRC=10.6): (a) shear stress and normal displacement vs. shear displacement; (b) effect of rock bolt

The shear behaviour of rock bolts inserted in natural rough joints is similar with the ones in the two-dimension standard JRC profiles joints. A summary of the test results and predicted values for two natural rough joints were shown in Table 2. The predicted values using Eq. (3) and (4) indicated good agreement with the test results with an average estimation error of 9.1%. The proposed model is capable of providing an accurate evaluation for the shear strength and shear displacement of rock bolt inserted in rough joints.

Table 2 Summary of the test results and predicted values for natural rough joints.

Specimen	Index	Test results	Predicted values	Error/%
N1	Maximum f_T	0.82	0.87	7.1
	Maximum f_s	1.70	2.00	17.6
N2	Maximum f_T	0.94	0.98	11.0
	Maximum f_s	1.54	1.55	0.6

5.5 Conclusions

The shear behavior of rock bolt inserted in the rough joints, with the JRC ranging from 0 to 18, was investigated with a series of single shear tests under CNL condition. In order to enable comparisons among test results obtained with different bolt diameters or steel qualities the dimensionless values of shear resistance and shear displacement were used.

The results indicated that the shear behaviour of rock bolt was strongly influenced by the joint roughness, and quite different with the smooth joints. The shear resistance of rock bolt increased gradually with the increasing of shear displacement for the smooth rock joint. However, the shear resistance reached to a large value in the early stage for most case of rough joints. The shear stiffness of rock bolt inserted in the rough joints was random for different JRC conditions but larger than the smooth rock joints case. The peak shear resistance of rock bolt was not always located at the end stage. The shear dilatancy of bolted rock joints was smaller than the ones without rock bolt for the same JRC condition.

A dimensionless mathematical model was established to predict the shear behaviour of rock bolt inserted in different roughness conditions. As the contribution of rock bolt on the shear resistance had a nonlinear relationship with the joint roughness, whereas the maximum shear displacement exhibited good linearity with a high correlation coefficient. The maximum shear resistance of rock bolt f_T was evaluate as a negative exponential function of JRC with a correlation coefficient of 0.9408. The maximum shear displacement of rock bolt f_s was evaluate as a linear function of JRC with a correlation coefficient of 0.9796.

Two tests with natural rough joints were conducted to verify the applicability of proposed mathematical model for the natural rough joints. The roughness profiles were measured using a laser profilometer. The shear behaviour of rock bolt inserted in natural rough joints was similar with the ones in the two-dimension standard JRC profiles joints. The predicted values of f_T and f_s by the new model indicated good agreement with the test results with an average estimation error of 9.1%. The proposed model is capable of providing an accurate evaluation for the shear strength and shear displacement of rock bolt inserted in rough joints.

References

Barton N, Choubey V (1977) The shear strength of rock joints in theory and practice. Rock Mech. 10: 1-54

Bjurstrom, S. (1974) Shear strength of hard rock joints reinforced by grouted untensioned bolts. In: Proceedings of the 3rd ISRM Congress, Denver, 1194-1199

Chen Y, Li CC. (2015a) Influences of Loading Condition and Rock Strength to the Performance of Rock Bolts, Geotechnical Testing Journal, 38(2): 208-218

Chen Y, Li CC. (2015b) Performance of fully encapsulated rebar bolts and D-Bolts under combined pull-and-shear loading Tunnelling and Underground Space Technology, 45: 99-106

Deb Debasis, Das Kamal C. (2014) A new doubly enriched finite element for modelling grouted bolt crossed by rock joint. 70: 47-58

Dight, PM. (1982) Improvement to the Stability of Rock Walls in Open Pit Mines. Ph. D. Thesis, Monash University, Australia.

Ferrero, A. (1995) The shear strength of reinforced rock joints. Int. J. Rock Mech. Mining Sci. Geomech. Abstracts 32 (6): 595-605

Grasselli, G. (2005) 3D Behaviour of bolted rock joints: experimental and numerical study. Int. J. Rock Mech. Min. Sci. 42: 13-24

Haas, C.J. (1976) Shear resistance of rock bolts. Soc. Min. Eng. 260: 32-41

Jalalifar H., Aziz N., Hadi M. (2006) The effect of surface profile, rock strength and pretension load on bending behaviour of fully grouted bolts. Geotech. Geol. Eng. 24: 1203-1227

Jalalifar H., Aziz N (2010a) Experimental and 3D Numerical Simulation of Reinforced Shear Joints. Rock Mech Rock Eng. 43:95-103

Jalalifar H., Aziz, N (2010b). Analytical behaviour of bolt-joint intersection under lateral loading conditions. Rock Mech. Rock Eng. 43: 89-94

Lee HS, Park YJ, Cho TF, et al. (2001) Influence of asperity degradation on the mechanical behavior of rough rock joints under cyclic shear loading. Int J Rock Mech Min Sci. 38(7): 967-980

Li, C. (2010) Field observations of rock bolts in high stress rock masses. Rock Mech. Rock Eng. 43 (4): 491-496

Li L., Hagan P.C., Saydam S., Hebblewhite B (2016a) Shear resistance contribution of support systems in double shear test. Tunnelling and Underground Space

Technology 56: 168-175

Li L., Hagan P. C., Saydam S., Hebblewhite B., Li Y (2016b) Parametric Study of Rockbolt Shear Behaviour by Double Shear Test. Rock Mech Rock Eng, DOI 10.1007/s00603-016-1063-4

Lin Hang, Xiong Zheyi, Liu Taoying, Cao Rihong, Cao Ping (2014) Numerical simulations of the effect of bolt inclination on the shear strength of rock joints. Int. J. Rock Mech. Min. Sci 66: 49-56

Li Xuwei, Nemcik Jan, Mirzaghorbanali Ali, Aziz Naj, Rasekh Haleh (2015) Analytical model of shear behaviour of a fully grouted cable bolt subjected to shearing. Int. J. Rock Mech. Min. Sci 80: 31-39

Li Xuwei, Aziz Naj, Mirzaghorbanali Ali, Nemcik Jan. (2016) Behavior of Fiber Glass Bolts, Rock Bolts and Cable Bolts in Shear. Rock Mech Rock Eng 49: 2723-2735

Marence M. and Swoboda G. (1995) Numerical Model for Rock Bolts with Consideration of Rock Joint Movements. Rock Mech. Rock Eng. 28 (3): 145-165

McHugh, E., Signer, S.D. (1999) Roof bolt response to shear stress: laboratory analysis. In: Proceedings 18th International Conference on Ground Control in Mining, Morgantown, WV, pp. 232-238

Pellet, F. and Egger, P. (1996) Analytical model for the mechanical behaviour of bolted rock joints subjected to shearing, Rock Mech. Rock Eng. 29(2): 73-97

Spang, K., Egger, P. (1990) Action of fully-grouted bolts in jointed rock and factors of influence. Rock Mech. Rock Eng. 23: 201-229

Song H, Duan Y, Yang J. (2010) Numerical simulation on bolted rock joint shearing performance. Mining science and technology. 20: 460-465

Srivastava L.P., Singh M. (2015) Effect of Fully Grouted Passive Bolts on Joint Shear Strength Parameters in a Blocky Mass Rock Mech Rock Eng. 48: 1197-1206

Tse R, Cruden DM (1979) Estimating joint roughness coefficients. Int J Rock Mech Min Sci Geomech Abstr. 16: 303-307

Wang G, Zhang X, Jiang Y, Wu X, Wang S (2016) Rate-dependent mechanical behavior of rough rock joints. Int. J. Rock Mech. Min. Sci. 83: 231-240

6 Estimating the support effect of the energy-absorbing rock bolt based on the mechanical work transfer ability

6.1 Introduction

High stress in surrounding rock mass can cause severe stability problems, such as massive squeezing and rock burst (Cantieni et al. 2009; Zhang et al. 2012; Zhao et al. 2014; Chen et al. 2015). It has been observed that numerous conventional rock bolts failed when experiencing large displacement of rock mass (Li, 2007; He et al. 2015). This phenomenon implies that they are too stiff to sustain large deformation and dynamic conditions (Stillborg 1994; Hoek et al. 1995). The energy-absorbing bolt, which is also called the yielding rock bolt, has been widely used for rock reinforcement in mining and civil engineering under the aforementioned conditions (Neugebauer 2008).

According to Windsor (1992), the types of rock bolts can be classified as: (1) continuously mechanically coupled (CMC), (2) continuously frictionally coupled (CFC), and (3) discretely mechanically or frictionally coupled (DMFC). Several analytical models have been proposed, such as those presented by Li and Stillborg (1999), Cai et al. (2004; 2015), Guan et al. (2007), Carranza-Torres. (2009), Tan C. (2016), and Farmer (1975). Most of them focused on the CMC and CFC rock bolts; however, the majority of the existing energy-absorbing rock bolts are of the DMFC bolt type (Jager 1992; Ansell 2005; Salzburg 2009; Li 2010; Wang 2013; He 2014).

For the DMFC bolt, solutions are only obtained by treating the contribution of the rock bolt as two uniformly compressive distributed loads applied at both ends of the bolts (Carranza-T 2009). However, the assumption of the smeared contribution of the rock bolt is acceptable only under the premise of small bolt spacing (Bobet 2011). The errors increase as the rock-bolt spacing increases. On the other hand, the sudden jump in radial stress of rock mass that appears at the distal end of the bolt will probably not occur in practice.

The mechanism of the interaction between the energy-absorbing rock bolt and the rock mass is substantially complex because of the yielding deformation of the rock bolt (Bobet 2011). The supporting design that employs the energy-absorbing rock bolt is still empirical or semi-empirical, and it is difficult to evaluate its performance quantitatively.

The mechanical work that the energy-absorbing rock bolt can transfer on the rock mass is an important ability, which can be used to estimate its support effect. However, there is no published research work that is focused on this topic. Therefore, it is imperative to develop a reasonable model to predict the mechanical work transfer ability of energy-absorbing rock bolts in practical engineering and to quantify their performance in the context of the supporting design.

This study is focused on estimating the quasi-static reinforcement effect of energy-absorbing rock bolts according to their mechanical work transfer ability using an analytical method. After a brief review of the mainstream energy-absorbing rock bolts, a coupling model will be proposed to describe the interaction between the energy-absorbing rock bolt and the rock mass, as well as the influence of the bolt and rock properties on the reinforcement effect; the mechanical work transfer ability will be highlighted through parameter studies.

6.2 Reinforcement mechanism of the energy-absorbing rock bolt

6.2.1 Generalized model of the energy-absorbing rock bolt

Regardless of their different types, most energy-absorbing rock bolts can be represented through a generalized model. As shown in Fig. 1, the interaction mechanism between the energy-absorbing rock bolt and the rock mass is concisely illustrated. The total length of the bolt can be divided into three segments: the outer anchoring segment, the free-elongating segment, and the inner anchoring segment (Wu 2016).

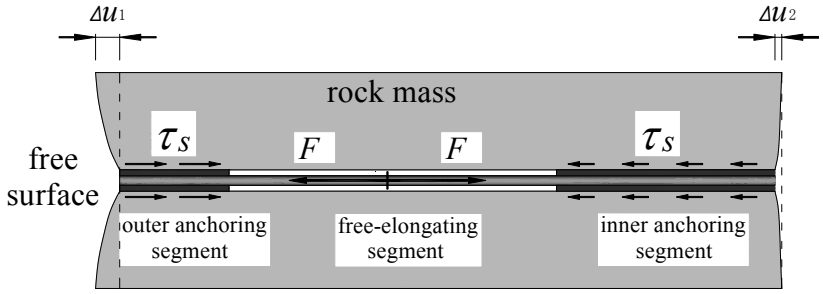

Fig. 1. The interaction mechanism between the energy-absorbing rock bolt and the rock mass.

After excavation, the surrounding rock mass will deform toward the excavation space. The outer anchoring segment of the energy-absorbing rock bolt will exert a stress on the rock mass to prevent its outward movement and transfer a positive work. In contrast, the stress of the inner anchoring segment points to the free surface, which

results in a negative work.

With the increasing rock mass displacement, the axial force of the rock bolt will increase at an early stage. Once the pre-set sliding load is reached, the free-elongating segment starts to function and the bolt load will remain constant, thus preventing the self-destruction of the energy-absorbing rock bolt, whereas the work transferred by the rock bolt will increase continuously.

6.2.2 The conventional spring-slider model

According to the pullout tests for passive bolts, the failure of the fully grouted bolts typically occurs at the bolt–grout interface, the grout–rock interface, the grout itself, and the rock matrix (Kilic et al. 2003). These four failure modes are generalized into conventional spring-slider model. The conventional spring–slider model can simulate the properties of CMC and CFC bolts, however, it not very suitable for energy-absorbing rock bolts, which are of the DMFC bolt type. On the other hand, there is no slider element in the bolt itself in the conventional model; therefore, the large deformation properties of energy-absorbing rock bolts cannot be expressed.

6.2.3 Interaction model of energy-absorbing rock bolt and rock mass

The energy-absorbing rock bolt is characterized by its large deformation properties, which means that the bolt can elongate to limit the axial load, and transfer more work on the rock mass. According to the characteristics of the energy-absorbing rock bolt, an interaction model is proposed, as shown in Fig. 2(a). The spring between the bolt and the anchor hole, which controls the interaction between the rock mass and the rock bolt, represents the shear stiffness of the anchoring agent. Its characteristic curve is shown in Fig. 2 (b). Endpoint A signifies that the relative displacement and the shear stress between the rock mass and the rock bolt will cease to increase, as the free-elongating segment starts to elongate. The slider and spring at the middle of the model represent the free-elongating segment, and the deformation characteristic curve is shown in Fig. 2 (c), where dF/dr is the shear force per unit length, and F is the axial force of bolt; u_s is the relative shear displacement of the bolt and rock mass; u_b is the relative displacement of the outer anchoring segment and the inner anchoring segment. The elongation characteristic of the energy-absorbing rock bolt is controlled by the slider. The elastic elongation characteristic of the bolt itself, namely the axial stiffness of the bolt material, is controlled by the spring at the axial direction. In this model, the function of the bolt

plate is replaced by the shear stress between the rock bolt and the rock mass at the outer end of the rock bolt; therefore, the shear failure of grout in the outer anchoring segment will not be considered. The free segment of the energy-absorbing rock bolt will start to elongate when the shear stress at the inner anchoring segment is excessively large, thus preventing shear failure between the rock bolt and the rock mass in this segment. Therefore, the slider unit between the rock bolt and the rock mass in the classic spring-slider model has been removed in the new model.

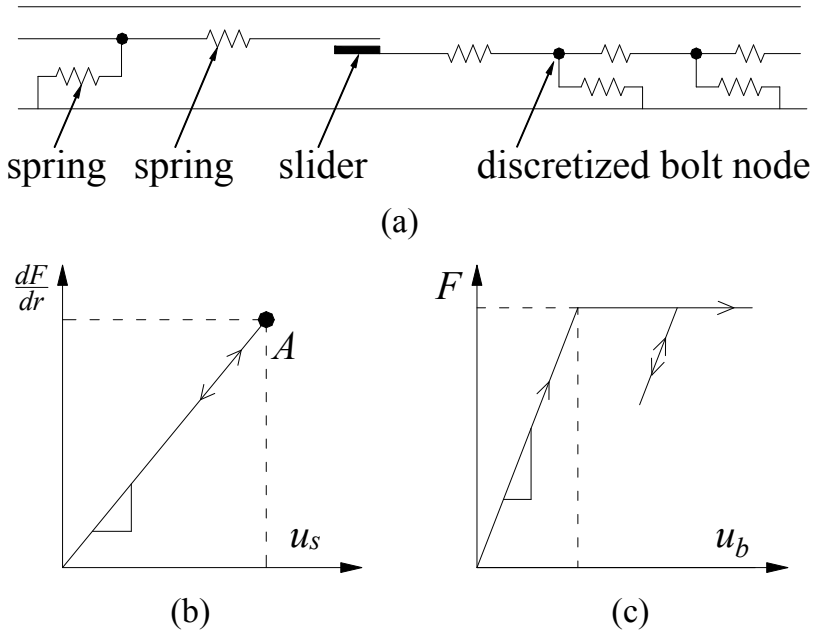

Fig. 2. The coupling model of yielding bolt and rockmass: (a) the structure model of yielding bolt; (b) the shear force per unit length versus relative shear displacement; (c) the axial force versus displacement of free-segment.

The shear stress between the rock bolt and the rock mass per unit length is controlled by a shear spring that is characterized by its shear stiffness, K_s, and the relative shear displacement, u_s. The relationship between shear force per unit length, dF/dr, and the relative shear displacement, u_s, is illustrated in Fig. 2(b). The shear force per unit length is proportionally mobilized by the relative shear displacement, as expressed in Eq. (1):

$$dF / dr = K_s u_s \ . \tag{1}$$

Dividing the shear force per unit length by the bolt perimeter πD_s, the shear stress around the bolt, τ_s, can be formulated as Eq. (2).

$$\tau_s = \frac{dF}{\pi D_s\, dr} = \frac{K_s u_s}{\pi D_s} \quad (\tau_s \le \tau_s^{set}) \tag{2}$$

Integrating the shear force per unit length along the bolt axis, the axial force of the bolt can be obtained via Eq. (3).

$$F = \int K_s u_s dr \quad (F \le F^{\text{set}}) \tag{3}$$

Here, F^{set} is the pre-set sliding load of the energy-absorbing rock bolt, and τ_s^{set} is the corresponding maximum shear stress around the bolt.

According to the balance equation of the bolt itself, the axial forces caused by the inner and outer anchoring sections are equal, and are lower than the maximum pre-set load capacity of energy-absorbing rock bolt. Assuming that a and b are the outer and inner boundaries of the free section, and that the stiffness of the outer anchor and inner anchor are K_{s1} and K_{s2}, respectively, we can then obtain the following equation:

$$\int_0^{\text{a}} K_{s1} u_s dr = -\int_b^{L_b} K_{s2} u_s dr\,. \tag{4}$$

With the unloading of the in-situ stress from initial stress to the final one after a tunnel excavation, the displacement of the surrounding rock mass increases gradually, and the shear force of the rock bolt continuously transfers work on the rock mass. The work done by the shear force at a length of dr, after an instant relative shear displacement du_s at a certain stage can be formulated as:

$$d^2W = dF du_s = K_s u_s dr du_s\,. \tag{5}$$

Integrating d^2W along the bolt axis, the work of the rock bolt at this stage can be obtained via Eq. (6).

$$dW = \int dF du_s = \int K_s u_s du_s dr\,. \tag{6}$$

Integrating dW along the unloading pass of the in-situ stress from P_0 to the final pressure, the total work of the rock bolt can be obtained via Eq. (7).

$$W = \iint K_s u_s dr du_s\,. \tag{7}$$

The most important properties involved in this model, the K_s, can be evaluated from the conventional pullout tests (Cao 2014). The rest of the properties of the rock bolt can be obtained directly from the specifications of the manufacturer.

6.3. Equilibrium equations for anchored rock mass around a circular tunnel

6.3.1 Strain-softening behavior of rock mass

In this study, the rock mass is assumed to satisfy the Mohr–Coulomb failure criterion and exhibit strain-softening behavior. The dilation factors in the strain-softening region and the plastic-flow region are considered identical, for the sake of simplicity. The major principal plastic strain, ε_1^p, is employed as the softening parameter. Therefore, the failure criterion, f, and the plastic potential, g, can be formulated as follows:

$$f = \sigma_1 - K_p \sigma_3 - \sigma_c = 0, \tag{8}$$

$$g = \sigma_1 - K_\psi \sigma_3 = 0, \tag{9}$$

with

$$\sigma_c = \begin{cases} \sigma_c^1 - \dfrac{(\sigma_c^1 - \sigma_c^2)\varepsilon_1^{\,p}}{\alpha} & (0 \le \varepsilon_1^{\,p} \le \alpha) \\ \sigma_c^2 & (\varepsilon_1^{\,p} \ge \alpha) \end{cases}, \quad K_p = \frac{1+\sin\phi}{1-\sin\phi}, \quad K_\psi = \frac{1+\sin\psi}{1-\sin\psi}.$$

Here, σ_1 and σ_3 are the major and minor principal stresses of the rock mass, respectively; ε_1^p is the major principal plastic strain, and serves as the softening parameter; K_p and $K\psi$ are the passive coefficient and the dilation factor of the rock mass, respectively, which are regarded as constants within the complete plastic region; σ_c is the compression strength, and transits gradually from σ_c^1 to σ_c^2, according to the evolution of the major principal plastic strain, ε_1^p; α is a shift point of the softening parameter that distinguishes the strain-softening region from the residual region.

The excavation of a long deep tunnel with a circular cross section under hydrostatic in-situ stress conditions can be considered as an axial-symmetry plane-strain problem, while neglecting the influence of gravity and restricting the out-of-plane principal stress as an intermediate stress. After a tunnel excavation, the surrounding rock mass will experience elastic, softening, and residual regions sequentially, according to different fictitious inner pressure exerted by the tunnel face and the support (Guan et al. 2007).

6.3.2 Equilibrium equations for anchored rock mass

The solution is based on the following assumptions: (1) the tunnel is deep; (2) the cross section is circular; (3) the problem is axisymmetric; (4) the ground is homogeneous and isotropic. The anchored zone contains the rock mass corresponding to

the outer anchoring segment and the inner anchoring segment of the energy-absorbing rock bolt. The free zone includes the rock mass of the free-elongating segment and the rock mass without the bolt. The equilibrium equations for the rock mass in the anchored zone and the free zone will be established separately, as shown in Fig. 3.

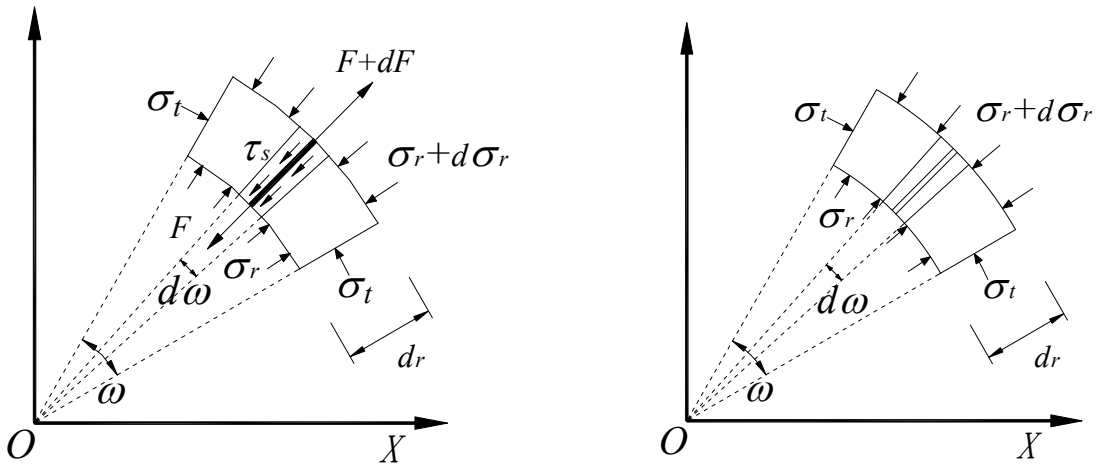

(a) (b)

Fig. 3. The equilibrium condition for the anchored matrix mass: (a) the anchored-segment; (b) the free-segment.

For the anchored zone, consider an infinitesimal volume in the radial direction, as illustrated in Fig. 3(a). The rock mass is subjected to radial stress σ_r, tangential stress σ_t, and shear stress τ_s caused by the energy-absorbing rock bolt. The increment of the bolt axial force caused by shear stress is defined as dF, and the axial force is defined as F. According to the research of Li et al. (1999), Cai et al. (2004) and Guan et al. (2007) on conventional bolts, the axial force, F, can be distributed evenly, around its tributary area. The static equilibrium condition of the infinitesimal rock-mass volume can be formulated as:

$$(\sigma_r - \frac{F}{r\omega L_z})rd\omega L_z + 2\sigma_t dr L_z \sin\frac{d\omega}{2} = (\sigma_r + d\sigma_r - \frac{F+dF}{(r+dr)\omega L_z})(r+dr)d\omega L_z . \tag{10}$$

Meanwhile, considering the interaction at the bolt–rock interface, dF can be expressed as:

$$dF = \tau_s \pi D_s \, dr . \tag{11}$$

Associating Eq. (10) with Eq. (11), noticing that $\sin(\frac{d\omega}{2})$ approximately equals to $\frac{d\omega}{2}$ because $d\omega$ is infinitesimal, the equilibrium equation can be deduced:

$$\frac{d\sigma_r}{dr} = \frac{\sigma_t - \sigma_r + N_0\tau_s}{r} \quad \text{with} \quad N_0 = \frac{\pi D_s}{\omega L_z}. \tag{12}$$

In the present work, the constant N_0 is referred to as the geometry coefficient because it is entirely determined by the geometrical properties of the bolts.

For the free zone shown in Fig. 3(b), the shear stress between the bolt and the rock mass is zero. The equilibrium equation can be formulated as:

$$\frac{d\sigma_r}{dr} = \frac{\sigma_t - \sigma_r}{r}. \tag{13}$$

The above equation can be seen as equal to the equilibrium equation, Eq. (9), when N_0 is set to zero. Therefore, Eq. (12) can be regarded as a uniform equation, regardless of the different zones.

6.3.3 Displacement compatibility equations for the rock mass

Based on the plane-strain axial symmetry assumption, the relationships of strain and displacement for the rock mass can be simplified as:

$$\frac{du}{dr} = \varepsilon_r \quad \frac{u}{r} = \varepsilon_t, \tag{14}$$

where ε_r is the strain in the radial direction, and ε_t is the strain in the tangential direction.

According to Hook's law, the tangential strain of the rock mass can be evaluated from its stress state in the elastic region, as formulated as in Eq. (15).

$$\varepsilon_t = (\frac{\sigma_t}{E} - \nu\frac{\sigma_r}{E} - \nu\frac{2P_0\nu}{E}) - (\frac{P_0}{E} - \nu\frac{P_0}{E} - \nu\frac{2P_0\nu}{E}) \tag{15}$$

Here, E and ν are the Young's modulus and the Poisson's ratio of the rock mass, respectively. It should be noted that only the strain caused by the tunnel excavation is considered, which means the initial strain owing to the in-situ stresses has been removed. Then, associating Eq. (14) with Eq. (15) and considering the hydrostatic in-situ stress condition, the displacement compatibility equation for the elastic region can be formulated as in Eq. (16).

$$u = r\varepsilon_t = \frac{P_0 - \sigma_r}{E}(1+\nu)r \tag{16}$$

For the plastic region, the loading path in this problem refers to a monotonic decrease in the fictitious inner pressure, corresponding to the advancing of the tunnel face. Consequently, the rates of all mechanical variables can be evaluated through their first-order derivatives with respect to P_i. The incremental theory of plasticity assumes that the total strain rate consists of both an elastic part and a plastic part, as shown in Eq. (17) (Carranza-T 1999). The elastic part is controlled by Hooke's law and the plastic part by the potential flow rule, as formulated in Eq. (18) and Eq. (19), respectively. The relationship between the strain rate and the displacement velocity is simplified by virtue of axial symmetry, and is described by Eq. (20):

$$\dot{\varepsilon}_r = \dot{\varepsilon}_r^{\,e} + \dot{\varepsilon}_r^{\,p}, \qquad \dot{\varepsilon}_\theta = \dot{\varepsilon}_\theta^{\,e} + \dot{\varepsilon}_\theta^{\,p}; \tag{17}$$

$$\dot{\varepsilon}_r^{\,e} = \frac{1-\nu}{2G}\dot{\sigma}_r - \frac{\nu}{2G}\dot{\sigma}_\theta, \quad \dot{\varepsilon}_\theta^{\,e} = \frac{1-\nu}{2G}\dot{\sigma}_\theta - \frac{\nu}{2G}\dot{\sigma}_r; \tag{18}$$

$$\dot{\varepsilon}_r^{\,p} = \lambda\frac{\partial g}{\partial \sigma_r} = \lambda, \quad \dot{\varepsilon}_\theta^{\,p} = \lambda\frac{\partial g}{\partial \sigma_\theta} = -\lambda K_\psi; \tag{19}$$

$$\dot{\varepsilon}_r = \frac{\partial \dot{u}}{\partial r}, \quad \dot{\varepsilon}_\theta = \frac{\dot{u}}{r}. \tag{20}$$

Here, g is the plastic potential that has been defined in Eq. (9). The rates of all mechanical variables (denoted by a dot mark) are expressed via their first-order derivatives with respect to P_i. Then, associating Eqs. (17) through (20), and by eliminating the multiplier λ, the displacement compatibility equation for the plastic region can be expressed as:

$$\frac{\partial \dot{u}}{\partial r} + K_\psi\frac{\dot{u}}{r} = \frac{(1-\nu-\nu K_\psi)}{2G}\dot{\sigma}_r - \frac{(\nu K_\psi - K_\psi + \nu)}{2G}\dot{\sigma}_\theta \tag{21}$$

6.4 Semi-analytical solutions for the equilibrium equations

Estimation of the support system required to stabilize a tunnel opening is a four-dimensional problem, which not only concerns with three spatial dimensions but also the temporal dimension. The unexcavated rock mass in front of working face plays an important role in stabilizing the tunnel opening, which can be seen as an artificial inner pressure applied at the surface of surrounding rock mass. The artificial inner pressure, P_i, decreases from the in-situ stress, P_0, to the final pressure from the tunnel lining, thus corresponding to the advancing process of the tunnel face.

6.4.1 Process of the solution

The equilibrium equations, the displacement compatibility equations, and the bolt-rock interaction equations presented above can only be solved numerically. A two-dimensional finite difference algorithm (i.e., along the unloading path and along the radial direction) was employed. All variables describing the mechanical state of the surrounding rock mass have two indices: the first (k) indicates a certain stage in the unloading path, and the second (i) indicates a certain position in the radial direction. Assuming that at a former stage (e.g., the $(k\text{-}1)^{\text{th}}$ stage, where $P_i = P_i^{(k\text{-}1)}$), all the mechanical states of the rock mass are known, the objective is to evaluate all the mechanical states at the current stage (i.e., the k^{th} stage, where $P_i = P_i^{(k)}$) according to their known counterparts at the former stage; the evaluation process includes the following three steps along the length direction of the rock bolt: stress evaluation, displacement evaluation, and bolt responses evaluation. After the completion of one iteration, these known mechanical states at the current stage can be used for the evaluation of the mechanical states at the next stage (i.e., the $(k+1)^{\text{th}}$ stage, where $P_i = P_i^{(k+1)}$), by following the same three steps. This type of iteration is repeated until the final stage, where $P_i = P_{i\_final}$. The effect of the support time is illustrated through the value of the artificial inner pressure, $P_{i\_install}$, when the energy-absorbing rock bolt is installed.

6.4.2 Stress evaluation of the rock mass

At the current stage, the radial stress at the tunnel wall, $\sigma_r(k, R_a)$, is known and equals to $P_i^{(k)}$, which serves as the boundary condition of the equilibrium equations. According to Eq. (12) and the failure criterion, the radial and tangential stresses can be obtained from the Runge–Kutta method (Schilling R 2000). When the radial stress increases up to the critical inner pressure P_i^{cri}, the position should be recorded as the radius of the elastoplastic interface R_e; then, the stress state of the elastic region should be evaluated. According to the research of Carranza-Torres (1999), σ_{re} is a constant that only depends on the properties of the rock mass itself, and is independent of the position of the elastoplastic interface. The critical inner pressure can be calculated via the following formula.

$$P_i^{cri} = \sigma_{re} = \frac{2P_0 - \sigma_c^1}{K_p + 1} \tag{22}$$

The bolt-rock shear stress and the transitional strength of the rock mass at the former stage are required during this step; the radial and tangential stresses at the current stage can be determined after the stress evaluation process.

6.4.3 Displacement evaluation of the rock mass

For the elastic region, the radial displacement of the rock mass at the current stage can be evaluated directly via the radial stress of the rock mass at the current stage, according to Eq. (16). For the plastic region, the fourth-order Runge–Kutta method is utilized again for the evaluation of the deformation rate at each consecutive calculation point (inward radial direction), according to the compatibility equations (21). Finally, the displacement at the current stage can be obtained by accumulating the displacement increment at the current stage to its counterpart at the former stage. After the displacement evaluation, the major principle plastic strain ε_t^p at the current stage, which here serves as the softening parameter, can be obtained. Then the transitional strength, $\sigma_c(k, r)$, at the current stage can also be computed via Eq. (8).

The displacements $u(k\text{-}1, r)$ and the stresses $\sigma_r(k\text{-}1, r)$, $\sigma_t(k\text{-}1, r)$ at the former stage, as well as the stresses at the current stage, are required in this step. The displacement, $u(k, r)$, and the transitional strength, $\sigma_c(k, r)$, at the current stage can be determined after the displacement evaluation process.

6.4.4 Interaction between the energy-absorbing rock bolt and the rock mass

Let us assume that the bolts are mounted at the j^{th} stage, where $P_i = P_i\_install$. The displacement of the rock mass at every point, u_{mob}, should be first computed.

The displacement of the rock mass is larger than that of the rock bolt at the surface of the tunnel, whereas the opposite occurs at the bottom end of the energy-absorbing rock bolt. Hence, a point must exist where the displacement of the rock mass is same as that of the rock bolt, and it is referred to as the nominal neutral point to distinguish it from the actual neutral point in the conventional rock bolt. Owing to the fact that the forces aroused from the outer anchoring segment and the inner anchoring segment are equal, the position of the nominal neutral point can be calculated via a numerical iterative method.

Assuming position ρ for the nominal neutral point, the relative shear displacement, u, at the current stage can be computed via Eq. (23).

$$\left.\begin{array}{ll} u(k,r) = u_{mob}(k,r) - u_{mob}(k,\rho) + u_e(k,r) & (r > \rho) \\ u(k,r) = u_{mob}(k,r) - u_{mob}(k,\rho) - u_e(k,r) & (r < \rho) \end{array}\right\}, \tag{23}$$

where $u_{mob}(k, \rho)$ denotes the mobilizing displacement at the neutral point, and $u_e(r)$ represents the elastic elongation of the bolt itself in relation to the nominal neutral point at different position. Then, using the assumed u, the bolt responses, $\tau_s(k, r)$ and $F_n(k, r)$, can be evaluated via Eq. (2) and Eq. (3). The total work of the rock bolt transferred on the rock mass can be evaluated via Eq. (7).

With the increase in the rock mass deformation, the bolt axial force will gradually increase. When the axial force reaches the pre-set sliding load, the free section of the energy-absorbing rock bolt starts to elongate, and the maximum axial force of the rock bolt will cease to change. In this case, the relative shear displacement between the rock bolt and the rock mass can be computed through Eq. (24).

$$\left.\begin{array}{ll} u(k,r) = u_{mob}(k,r) - u_{mob}(k,\rho) + u_e(k,r) + u_{slide}(k) & (r > \rho) \\ u(k,r) = u_{mob}(k,r) - u_{mob}(k,\rho) - u_e(k,r) - u_{slide}(k) & (r < \rho) \end{array}\right\}, \tag{24}$$

where, $u_{slide}(k)$ represents the elongation of the bolt-free segment after yielding, and it can be obtained through numerical iterative calculation based on the fact that the maximum bolt axial force will not change.

The relative displacements at this stage and the bolt installation stage are required in this step. The proper bolt responses and the total work of the rock bolt transferred on the rock mass can be determined after the evaluation process of the bolt responses.

After these three steps, all the mechanical states at the current stage (including the stress and the displacement distribution of the rock mass, the shear stress, the axial force, and the work transferred of rock bolt) are known, and can be used at the next stage (i.e., the $(k+1)^{th}$ stage, where $P_i = P_i^{(k+1)}$).

6.5 Application and verification through an illustrative case study

The proposed method was programmed in a Visual Basic (VB) environment, and was verified through numerical simulations. In this section, an illustrative case study will be presented to demonstrate the reinforcement mechanics of the energy-absorbing rock bolt in tunneling.

6.5.1 An illustrative case study

We assumed that a circular tunnel with a design radius of 5 m is excavated under a

hydrostatic in-situ stress of 10 MPa. The Young's modulus and Poisson's ratio of the rock mass is 1.0e^9 Pa and 0.25, respectively. The peak strength and residual strength of the rock mass is 5 MPa and 3 MPa, respectively. The passive coefficient, K_p, and the dilation factor, K_ψ, of the rock mass is 3.0 and 1.33, respectively, and they are constant within the entire plastic region. The softening parameter, α, is 0.0025.

The total length of the bolt is 3 m; the outer anchoring segment is 0.5 m, the free-elongating segment is 1.8 m, and the inner anchoring segment is 0.7 m. The diameter of the rock bolt is 20 mm, with a yielding strength of 300 kN. The Young's modulus of the rock bolt is 2.1e^{11} Pa. The shear stiffness of grout, K_s, is 35 MPa. The axial spacing along the tunnel is 1.0 m, and the circumferential spacing is 0.224 rad (1.12 m). The energy-absorbing rock bolt should be mounted at the stage when $P_i^{(j)} = P_0$*37.5%, which is equal to the critical inner pressure for the rock mass in the present case.

The ground and bolt responses are shown in Figs. 4 through 7 (represented by solid lines). To highlight the reinforcement effect of the energy-absorbing rock bolt, the ground responses at the same stage —without bolt reinforcement—are also depicted in the aforementioned figures (represented by dashed lines).

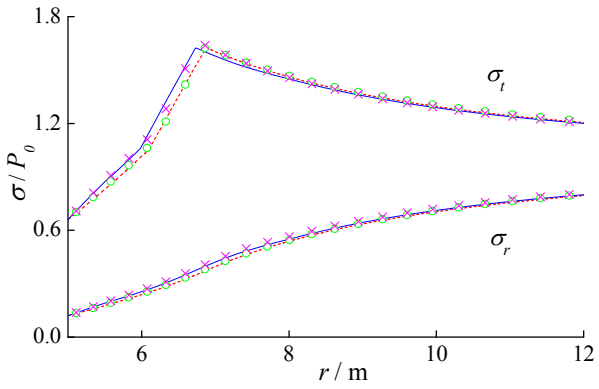

(a)

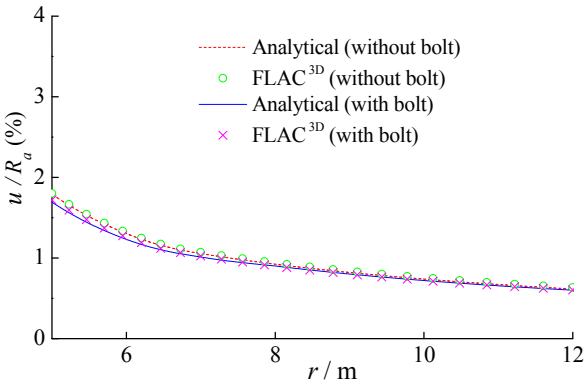

(b)

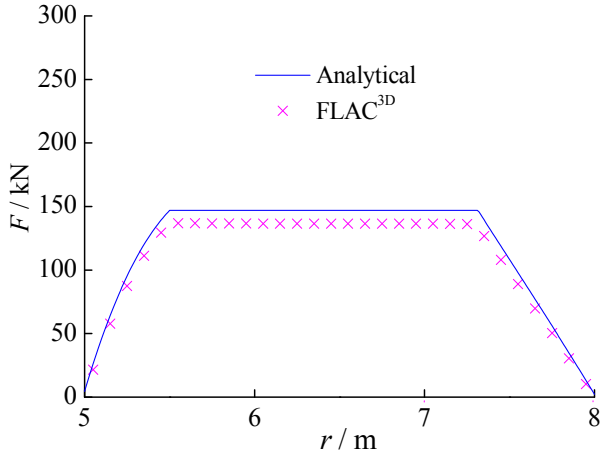

(c)

Fig. 4. The ground and bolt responses at Pi=1.2MPa stage: (a) the stress distribution along the radial direction; (b) the displacement distribution along the radial direction; (c) the distribution of axial force along the bolt length.

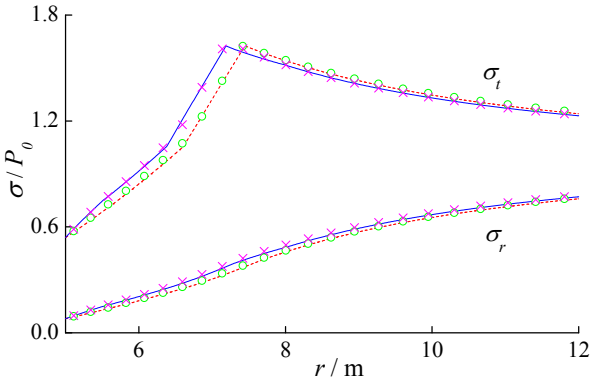

(a)

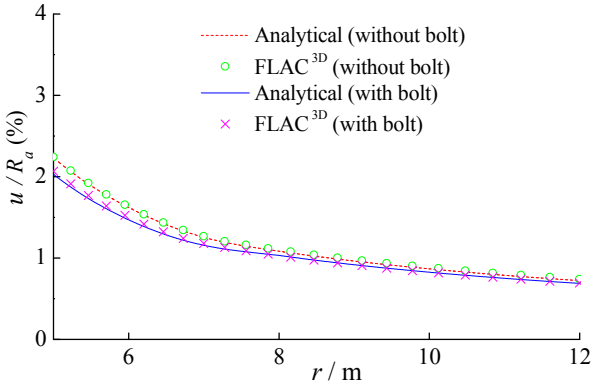

(b)

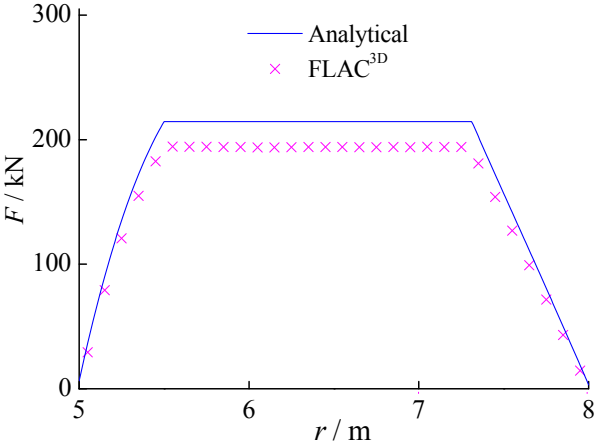

(c)

Fig. 5. The ground and bolt responses at Pi=0.8MPa stage: (a) the stress distribution along the radial direction; (b) the displacement distribution along the radial direction; (c) the distribution of axial force along the bolt length.

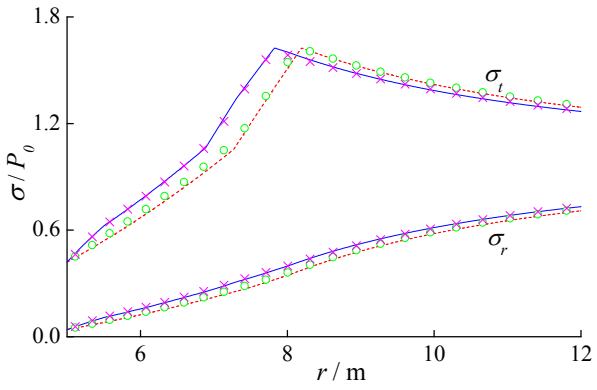

(a)

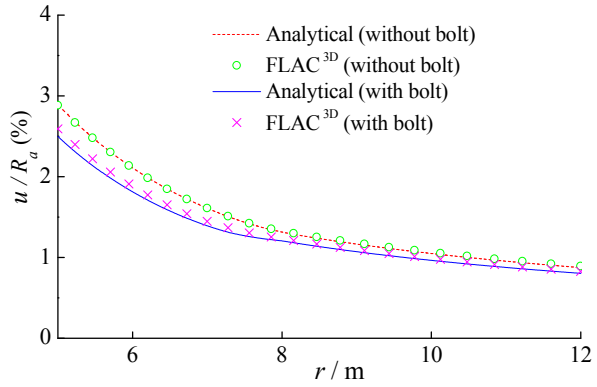

(b)

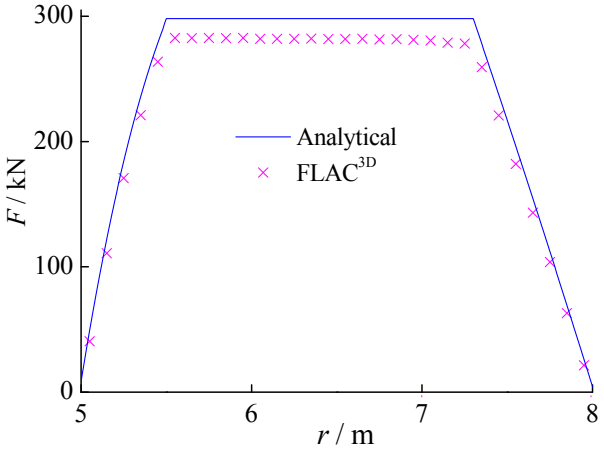

(c)

Fig. 6. The ground and bolt responses at Pi=0.4MPa stage: (a) the stress distribution along the radial direction; (b) the displacement distribution along the radial direction; (c) the distribution of axial force along the bolt length.

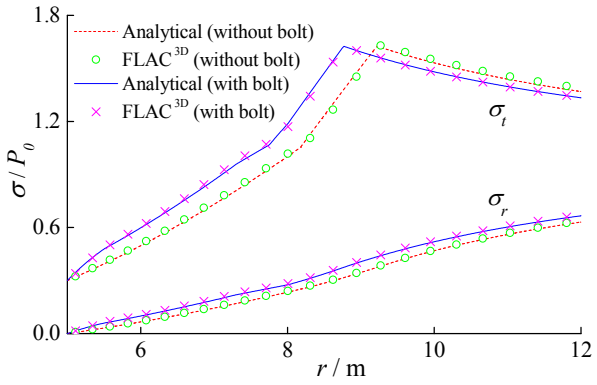

(a)

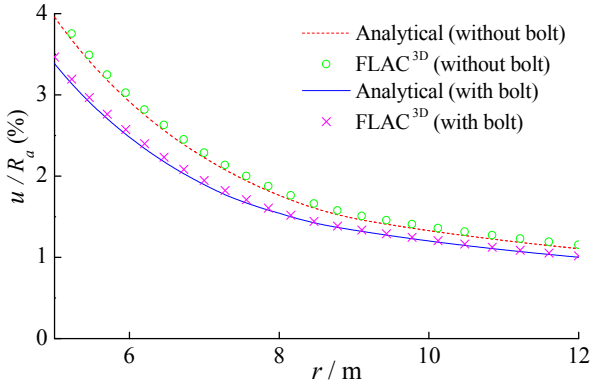

(b)

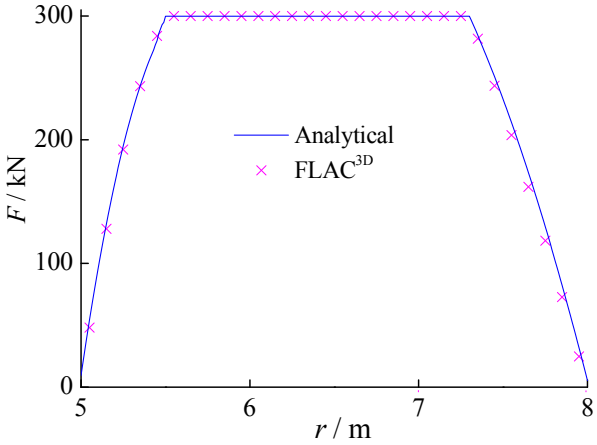

(c)

Fig. 7. The ground and bolt responses at Pi=0.0MPa stage: (a) the stress distribution along the radial direction; (b) the displacement distribution along the radial direction; (c) the distribution of axial force along the bolt length.

With the decrease in the inner pressure for the rock mass, the displacement released by the rock mass increases, and the energy-absorbing rock bolts exert their effect gradually. At the $P_i^{(k)}$ = 1.2 MPa stage, the reinforcement effect is not significant in relation to the displacement of the rock mass, and the maximum axial force along the energy-absorbing rock bolt is 145 kN. At the $P_i^{(k)}$ = 0.8 MPa stage, the maximum axial force is 215 kN, and the reinforcement effect increases gradually. At the $P_i^{(k)}$ = 0.4 MPa stage, the maximum axial force reaches 300 kN, indicating that the bolt is yielding and starts to elongate. At the $P_i^{(k)}$ = 0.0 MPa stage (i.e., no lining is supported after the tunnel face has advanced), the energy-absorbing rock bolts help constrain the convergence of the tunnel opening from 4.0% to 3.4%. The analytical results show that the maximum axial force of the bolt is always 300 kN after yielding, indicating that the large-deformation characteristic of the energy-absorbing rock bolt in this new model is well expressed.

The convergence confinement method is usually adopted in the support system design in conventional tunneling (Carranza-T C, 2000; Oreste, 2003). Using the proposed method, the ground reaction curve (GRC) without bolt reinforcement, the bolted ground reaction curve (BGRC), and the bolt reaction curve (BRC) can be constructed by recording the displacement released at the tunnel wall, u_a, and the maximum axial force in the bolt, F^{max}, at each unloading stage. The GRC, the BGRC, and the BRC in the illustrative case are depicted in Fig. 8.

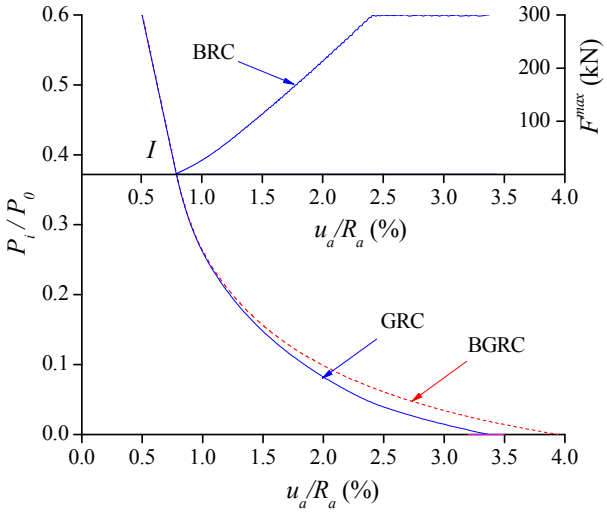

Fig. 8. The reinforced ground reaction curve and the bolt reaction curve.

The evolution of the total work of the energy-absorbing rock bolt with the increase in the rock mass displacement is shown in Fig. 9. The work transferred by the outer anchoring segment and inner anchoring segment are also depicted. As the outer anchoring segment applies a stress to prevent the rock-mass outward movement, it therefore transfers a positive work. The stress of the inner anchoring segment points toward the free surface, which will transfer a negative work. The total work of the energy-absorbing rock bolt is positive and gradually increases with the increase in rock-mass displacement.

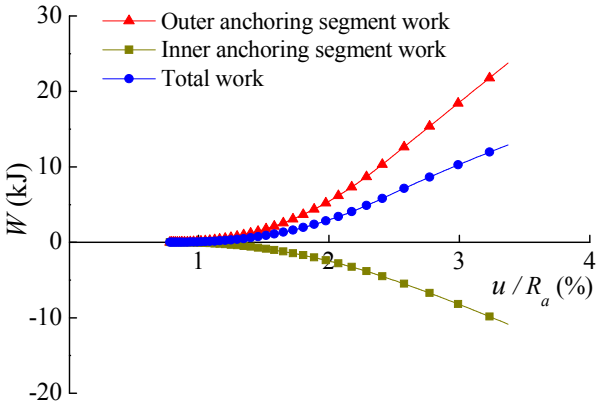

Fig. 9. The evolution of the total work of the energy-absorbing rock bolt with the increase in the rock mass displacement.

6.5.2 Verification through numerical simulations

The validity of the proposed method was verified through numerical simulations (FLAC^{3D} software). The strain-softening constitutive laws in FLAC^{3D} are characterized by six parameters: the bulk modulus K, the shear modulus G, the friction angle ϕ, the cohesion c, the dilation angle ψ, and the softening parameter η. They were evaluated based on their counterparts that were employed in the analytical method.

The results from the numerical simulations are also depicted in Figs. 4 through 7, and are depicted as cross or dot marks. As shown in these figures, the ground and bolt responses computed through the proposed method and the numerical simulations are in excellent agreement, indicating that the semi-analytical solutions for the energy-absorbing rock bolt around the circular tunnel is valid. The proposed method can rationally elucidate the reinforcement mechanics of the energy-absorbing rock bolt in tunneling.

6.6 Parameter analysis based on the new model

Based on the proposed model, the influence of different parameters, including the stress condition, strength of rock mass, bolt space, bolt length, and the reinforcing time, on the reinforcement effect was quantitatively estimated. Considering the illustrative case as a standard case, and by varying every single parameter from 0% to 200% of its initial value, the relative significance of different parameters on the reinforcement effect can be illustrated.

In this study, the difference in the maximum tunnel convergence with and without the rock bolt Δu_x^{max}, together with the maximum bolt axial force, F_x^{max}, and the maximum bolt work, W_x^{max}, were selected as the estimation indexes. The difference in the maximum tunnel convergence with and without the rock bolt highlights the reinforcement effect of the energy-absorbing rock bolt. The maximum bolt axial force and the maximum bolt work are the two self-indexes of the bolt working state. The indexes were divided by the values of (Δu_s^{max}, F_s^{max}, W_s^{max}) that were obtained in the illustrative case in order to obtain dimensionless values. The dimensionless values can better illustrate the sensitivity of the parameters and enable the comparisons among results that were obtained under different conditions.

6.6.1 Influence of in-situ stress

The in-situ stress of the rock mass was selected for the study of the influence of the application environment on the supporting effect of the rock bolt. The in-situ stress was varied from 0% to 200% of its initial value (10 MPa). Meanwhile, the other parameters were the same as those in the illustrative case. Fig. 10 presents the evolution of the tunnel convergence difference, the bolt axial force, and the bolt work as the in-situ stress increases. The results show that all three indexes are significantly low, when P_0 = 5 MPa (50%). The maximum axial force is 72 kN (0.24*F_s^{max}), whereas the tunnel convergence difference and the bolt work on the rock mass are both approximately equal to zero. With the increase in the in-situ stress, the tunnel convergence increases significantly; similar observation can be made for the bolt axial force and the bolt work. When the in-situ stress is greater than 10 MPa, the bolt axial force reaches the yielding strength of 300 kN and remains constant, whereas the bolt work continuously increases, together with the tunnel convergence difference. In the case of higher in-situ stress, the support effect of the energy-absorbing rock bolt is considerably improved, and the bolt

absorbs more energy.

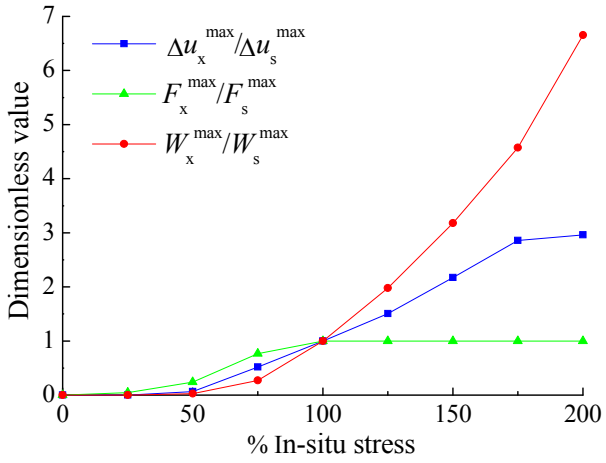

Fig. 10. The evolution of the tunnel convergence difference, the bolt axial force, and the bolt work as the in-situ stress increases.

6.6.2 Influence of rock strength

In the present section, the influence of rock strength will be studied. The peak strength and residual strength of the rock mass were varied from 25% to 200% of their initial value (5 MPa and 3 MPa, respectively), whereas the other parameters were the same as those in the illustrative case. Fig. 11 illustrates the evolution of the tunnel convergence difference, the bolt axial force, and the bolt work as rock strength increases.

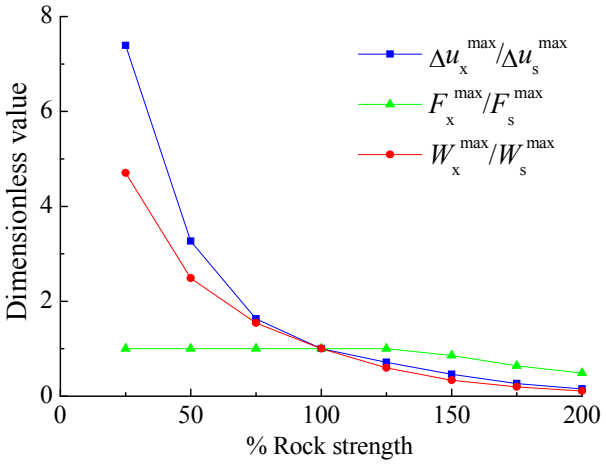

Fig. 11. The evolution of the tunnel convergence difference, the bolt axial force, and the bolt work as rock strength increases.

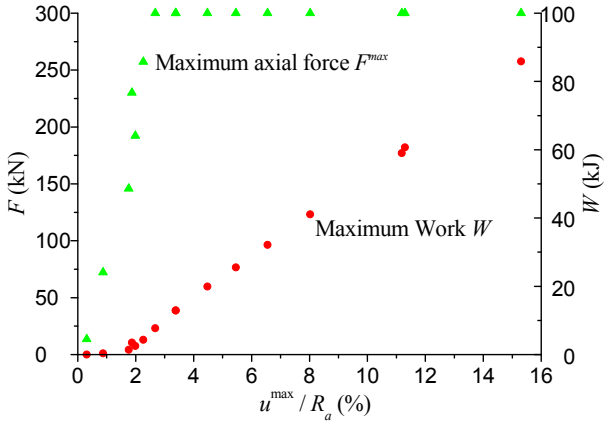

Fig. 12. The evolution of the bolt axial force and the bolt work as the maximum tunnel convergence increases.

According to this figure, the influence of the rock strength on the supporting effect is similar to that of the rock stress. The typical characteristic is that the tunnel convergence difference, the maximum axial force, and the bolt work decrease with the increase in rock strength. In the case of lower rock strength, the support effect has significantly improved, and the bolt absorbs more energy.

In Figs. 10 and 11, it is obvious that the bolt work has a better correspondence with tunnel convergence difference than the bolt axial force. This phenomenon indicates that the bolt work transferred on the rock mass is a more effective estimation index of the supporting effect than the bolt maximum axial force. To further study this behavior, the evolution of the bolt axial force and the bolt work as the maximum tunnel convergence increases are shown in Fig. 12. The results show that the axial force of the energy-absorbing rock bolt increases rapidly and almost linearly with the increase in the maximum tunnel convergence before reaching the yielding strength of 300 kN. In the meanwhile, the bolt work transferred on the rock mass is quite small. When the maximum tunnel convergence exceeds 2% of the tunnel radius and the energy-absorbing rock bolt is in yielding state, the work starts to increase rapidly and linearly with the increase in tunnel convergence.

The deformation characteristics of the energy-absorbing rock bolt play a highly important role in rock reinforcement. The performance of the energy-absorbing rock bolt is very satisfactory and absorbs a substantial amount of energy from the rock mass, even when the maximum tunnel convergence reached 16% of the tunnel radius. However, under this condition, the conventional rock bolt would be damaged, which

indicates that the yielding support is necessary for a high-stress or low-strength rock mass. The satisfactory performance of the energy-absorbing rock bolt highlighted the advantages of the large-deformation supporting.

6.6.3 Influence of the bolt space

In this section, the influence of the bolt installation space, namely the bolt density, will be studied. The bolt space, including the longitudinal space and the circumferential space were varied from 50% to 200% of their initial value (1 m and 1.12 m), whereas the other parameters were the same as the ones of the illustrative case. Fig. 13 illustrates the evolution of the tunnel convergence difference, the bolt axial force, and the bolt work as the bolt space increases.

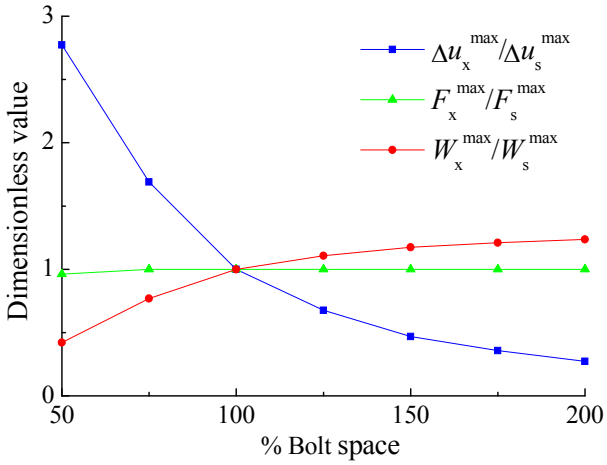

Fig. 13. The evolution of the tunnel convergence difference, the bolt axial force, and the bolt work as the bolt space increases.

The results show that decreasing the longitudinal spacing and the circumferential spacing (i.e., increasing the bolt installation density) may always be helpful in the stabilization of the surrounding rock mass. However, a high bolt density would be unnecessary and the bolt would not be fully utilized because the bolt work would be relative small, even when the maximum axial forces under different conditions are almost unchanged.

6.6.4 Influence of the bolt length

In the present study, the total bolt length was varied from 50% to 200% of its initial value (3 m). The length of the outer anchoring segment (0.5 m) and the inner anchoring

segment (0.7 m) remained unchanged, and the length of the free-elongating segment was changed accordingly. Fig. 14 presents the evolution of the tunnel convergence difference, the bolt axial force, and the bolt work as the bolt length increases.

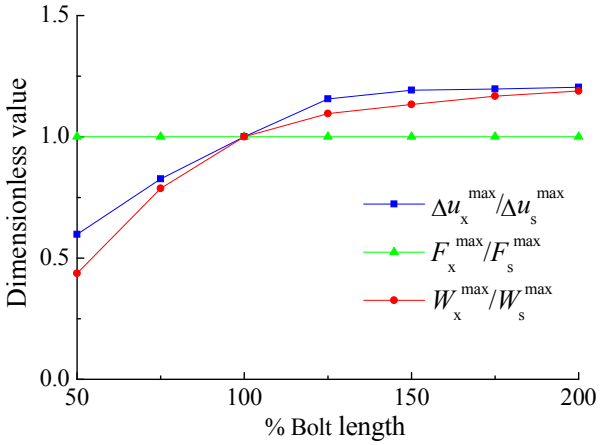

Fig. 14. The evolution of the tunnel convergence difference, the bolt axial force, and the bolt work as the bolt length increases.

When the bolt length is less than 4.5 m, the tunnel convergence decreases significantly, as the bolt length increases. On the other hand, when the bolt length is longer than 4.5 m, the supporting effect cannot be improved, even when the bolt is very long. This is because the radius of the plastic area is 4.23 m for the unsupported conditions, as shown in Fig. 10. Additional rock-bolt length would hardly affect the ground reinforcement, because the bolt section embedded in the elastic region of the rock mass would barely help to constrain the elastic displacement release (under the scope of continuous deformation media). Therefore, it is unnecessary to excessively extend the bolt beyond the range of the plastic region. The rock bolts of different bolt lengths have similar maximum axial forces; however, they present different reinforcement effects. The correlation of the bolt work and the reinforcement effect once again illustrates that the bolt work is a more effective estimation index.

6.6.5 Influence of reinforcing time

According to the convergence–confinement method, the influence of the reinforcing time could be studied by changing the mounted stage (artificial inner pressure P_i) of the rock bolt. In this study, the bolt-installation stage was varied from 25% (installed later) to 200% (installed earlier) of its initial value (P_0*37.5%). The evolution of the tunnel convergence difference, the bolt axial force, and the bolt work

are shown in Fig. 15.

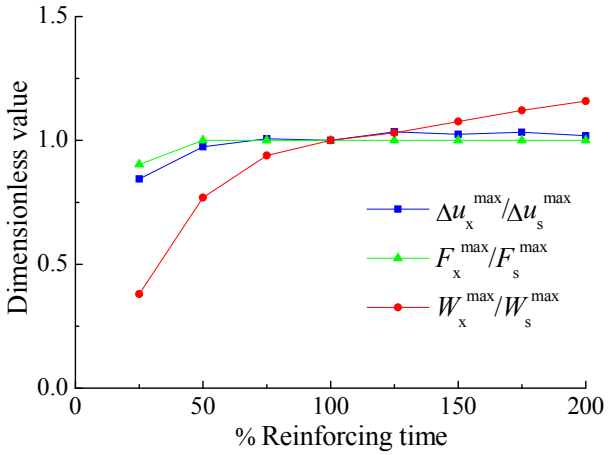

Fig. 15. The evolution of the tunnel convergence difference, the bolt axial force, and the bolt work as the bolt reinforcing time increases.

The rock bolt is mounted at the stage when $P_i^{(j)} = P_0$*37.5% in the illustrative case, and it equals to the critical inner pressure of the rock mass. When the reinforcing time is earlier than that of the illustrative case, no significant contribution can be observed in the tunnel convergence difference, and the increase in bolt work is fairly minor. If the energy-absorbing rock bolt is installed later than when it was installed in the illustrative case, the tunnel convergence difference and the bolt work would both significantly decrease, thus illustrating that the capacity of the energy-absorbing rock bolt is not fully utilized. It is recommended that the bolt should be installed no later than the stage of critical inner pressure, namely when the plastic region occurs.

6.7 Conclusions

The mechanical and deformation mechanism of the energy-absorbing rock bolts were reviewed. Then, a coupling model was proposed to describe the interaction between the energy-absorbing rock bolt and the rock mass. Based on the plane-strain axial symmetry assumption and the incremental theory of plasticity, equilibrium equations and compatibility equations of the matrix mass, as well as the response of the energy-absorbing rock bolt were theoretically deduced.

The proposed method was programmed in the VB development environment, and a semi-analytical solution for the coupling model was achieved. The reinforcement mechanism of the energy-absorbing rock bolt in conventional tunneling was clearly demonstrated through an illustrative case study. In addition, the validity of the proposed

method was verified through numerical simulations.

Based on the proposed model, the influence of the stress conditions, the strength of the rock mass, the bolt density, the bolt length, and the reinforcing time were quantitatively estimated, and the evolution of the maximum axial force and the bolt work transferred on the rock mass were presented. The results revealed that the performance of the energy-absorbing rock bolt is significantly improved in high-stress and low-strength rock conditions. The bolt could significantly reduce the deformation of the plastic zone, whereas the control effect of the elastic zone is not particularly obvious. Therefore, it is unnecessary to excessively extend the bolt beyond the range of the plastic region. On the contrary, increasing the bolt installation density could always help to reinforce and stabilize the surrounding rock mass. The tunnel convergence is significantly influenced by the reinforcing time; earlier installation is preferred for the energy-absorbing rock bolt. The bolt work transferred on the rock mass is a more effective estimation index than the bolt maximum axial force.

This study was focused on the quasi-static mechanical work transfer ability of the energy-absorbing rock bolt. In the future, it is imperative that the reinforcement effect of the energy-absorbing rock bolt under impact conditions be studied, according to its mechanical work transfer ability in practical engineering.

References

Ansell, A (2005) Laboratory testing of a new type of energy absorbing rock bolt. Tunn Undergr Space Technol 20: 291-300

Bobet A, Einstein H (2011) Tunnel reinforcement with rockbolts. Tunn Undergr Space Technol 26(1): 100-123

Cai Y, Esaki T, Jiang Y (2004) A rock bolt and rock mass interaction model. Int J Rock Mech Min Sci 41(7): 1055-1067

Cai Y, Jiang Y, Djamaluddin I, Iura T, Esaki T. An analytical model considering interaction behavior of grouted rock bolts for convergence–confinement method in tunneling design. Int J Rock Mech Min Sci 2015; 76: 112–126.

Cantieni L, Anagnostou G (2009) The interaction between yielding supports and squeezing ground. Tunn Undergr Space Technol 24: 309-322

Cao C, Ren T, Cook C, Cao Y. Analytical approach in optimising selection of rebar bolts in preventing rock bolting failure. Int J Rock Mech Min Sci 2014; 72: 16–25.

Carranza-T C, Fairhurst C (1999) The elasto-plastic response of underground

excavations in rock masses that satisfy the Hoek-Brown failure criterion. Int J Rock Mech Min Sci 36 (6): 777-809

Carranza-T C, Fairhurst C. Application of convergence-confinement method of tunnel design to rock masses that satisfy the Hoek-Brown failure criterion. Tunnelling and Underground Space Technology, 2000, 15 (2), pp. 187-213

Carranza-T. C (2009) Analytical and numerical study of the mechanics of rockbolt reinforcement around tunnels in rock masses. Rock Mech Rock Eng 42(2): 175-228

Chen B, Feng X, Li Q, et al (2015) Rock Burst Intensity Classification Based on the Radiated Energy with Damage Intensity at Jinping II Hydropower Station, China. Rock Mech Rock Eng 48: 289-303

Cook, N., Ortlepp, W (1968) A energy-absorbing rock bolt. Chamber of Mines of South Africa. Research Organization Bulletin, no. 14

Farmer I W. Stress distribution along a resin grouted rock anchor. Int. J. Rock Mech. Min. Sci. Geomech. Abstr 1975; 12: 347-351.

Guan, Z., Jiang, Y., Tanabasi, Y (2007) Reinforcement mechanics of passive bolts in conventional tunnelling. Int J Rock Mech Min Sci 44(4): 625-636

Guan, Z., Jiang, Y., Tanabasi, Y (2007) Ground reaction analyses in conventional tunneling excavation. Tunn Undergr Space Technol 22 (2): 230-237

Hoek, E., et al (1995) Support of underground excavation in hard rock. Balkema, Rotterdam: 1-10

He, M, Gong, W, Wang, J, et al (2014). Development of a novel energy-absorbing bolt with extraordinarily large elongation and constant resistance. Int J Rock Mech Min Sci 67: 29-42

He M, Zhao F, Cai M, Du S (2015)A Novel Experimental Technique to Simulate Pillar Burst in Laboratory. Rock Mech Rock Eng, DOI 10.1007/s00603-014-0687-5

Jager, A (1992) Two new support units for the control of rockburst damage. Rock support in mining and underground construction: 621-631

Kilic A, Ysar E, Atis C (2003) Effect of bar shape on the pullout capability of fully-grouted rock bolts. Tunn Undergr Space Technol 18(1): 1-6

LI C, STILLBORG B (1999) Analytical models for rock bolts. Int J Rock Mech Min Sci 36 (8): 1013-1029

Li C (2010) A new energy-absorbing bolt for rock support in high stress rock masses.

Int. J. Rock Mech. Mining Sci. 47: 396-404

Li C. C. A Practical Problem with Threaded Rebar Bolts in Reinforcing Largely Deformed Rock Masses Rock Mech. Rock Engng. (2007) 40 (5), 519–524

Oreste P. Analysis of structural interaction in tunnels using the convergence–confinement approach. Tunnelling and Underground Space Technology, 2003, 18 (4), pp. 347-363.

Neugebauer E (2008) A New Way to tackle Safety in Underground Operations. Mining and Construction. 3(08): 24-25

Salzburg (2009) In-Situ pull testing of a yieldable rock bolt, Roofex. Controlling Seismic Hazard and Sustainable Development of Deep Mines: 1081-1090

Stillborg B (1994) Professional users handbook for rock bolting, 2nd ed. Trans Tech Pub

Schilling R, Harris S (2000) Ordinary difference equations. In: Applied numerical methods for engineers using MATLAB and C. Thomson Learning Inc: 361-421

Tan C. Difference solution of passive bolts reinforcement around a circular opening in elastoplastic rock mass. Int J Rock Mech Min Sci 2016; 81: 28–38.

Wang G, Wu X, Jiang Y, et al (2013) Quasi-static laboratory testing of a new rock bolt for energy-absorbing applications. Tunn Undergr Space Technol 38: 122-128

Windsor C, Thompson A (1992) A New Friction Stabilizer Assembly for Rock and Soil Reinforcement Applications. Rock Support in Mining and Underground Construction, Rotterdam: 523-529

Wu X, Jiang Y, Wang G, Li B. Analysis on the reinforcement effect of yielding rock bolt. Chinese Journal of Geotechnical Engineering, 2016, 38(2): 245-252.

Zhang C, Feng X, et al (2012) A Top Pilot Tunnel Preconditioning Method for the Prevention of Extremely Intense Rockbursts in Deep Tunnels Excavated by TBMs. Rock Mech Rock Eng 45: 289-309

Zhao X, Wang J, Cai M, et al (2014) Influence of Unloading Rate on the Strainburst Characteristics of Beishan Granite Under True-Triaxial Unloading Conditions. Rock Mech Rock Eng 47: 467-483

Part III

Health assessment of mountain tunnels in soft rock

7 A new health assessment index of tunnel lining based on the digital inspection of surface cracks

7.1 Introduction

A large number of tunnels have been in service for the past decades all over the world. The tunnels were mainly supported by concrete lining (Soheyli 2016; Yan 2017). The type of concrete lining can be divided into three categories, including shotcrete, prefab and cast-in-place lining. The cast-in-place concrete lining was the most commonly used one and it was studied in this paper. The persistent ageing and seismic activity lead to many problems to the cast-in-place concrete lining, such as cracking, corrosion and leakage (Aktan 2000; Malmgren 2005; Li 2017). The damage of tunnel lining will decrease its integrity and subsequently increase the risk of tunnel lining collapse (Bhalla 2005). In order to deal with this situation, there is an urgent requirement for accurate tunnel lining health assessment methods (Gao 2014; Gao 2016; Jiang 2016; Wang 2017).

Generally, the stability of aged cast-in-place tunnel lining was mainly evaluated based on the visual inspection (Hayashi 2004). But the evaluation standard was qualitative, and the results depended on the experience of different engineers. As a solution of this problem, the Tunnel-lining Crack Index (TCI) was proposed to quantitatively evaluate the severity of tunnel lining cracks (Shigeta 2006). It has been widely applied for the inspecting of surface defects of tunnels in Japan. The stability assessment based on TCI is reasonable to some extent because the mechanical stability of a tunnel is greatly influenced by the severity of cracks in the lining (Yamada 2009). However, the intersection and distribution of cracks, which could greatly influence the stability of tunnel lining, was not considered in TCI. The uncertainty relationship between TCI and the instability of tunnel lining called for more alternative assessment methods and health indexes.

As the distribution of cracks in tunnel lining is quite complex, it is difficult to make a precise description through conventional mathematical methods. Fortunately, fractal theory is used to analyze the distribution of complex graphics. It has been widely used in art, astronomy, geography, biology, fluid dynamics, probability theory, chaos theory, and pure mathematics in the past few decades (Briggs 1992; Bisoi 2001; Harte 2001; Bolliger 2003; Wang 2015; Wang 2016). In recent years, the fractal theory was used to describe the propagation of cracks in rock or concrete specimens in laboratory (Xie 1995; Xie 2001; Yu 2016; Tian 2016; Xue 2016; Alves 2016). These studies confirmed that the cracks in concrete have fractal properties. Therefore, it is possible to describe the

distribution of cracks and evaluate the states of tunnel lining by fractal theory. Moreover, the development of machine vision-based method makes it possible to collect the images of tunnel lining and to calculate the dimensions of the cracks efficiently (Zhang 2014; Huang 2017).

In this study, the fractal dimension of cracks in tunnel lining was taken as a new health assessment index. A series of comparative tests and field tests were conducted to evaluate the validity of this new method. In addition, the quantitative correlation between fractal dimension and TCI of cracks in tunnel lining was studied.

7.2 Theoretical background

7.2.1 Concept of Tunnel-lining Crack Index

The conceptual diagram of TCI (Shigeta 2006) was shown in Fig. 1. One span of the tunnel shown in the left side of the figure was spread out to a flat surface as shown in the right side. The basic formula of TCI is shown in equation (1):

$$F_{ij} = \frac{1}{A}\sum_{k=1}^{n}\left(t^{(k)}\right)^{\alpha}\left(l^{(k)}\right)^{\beta}\cos\theta_i^{(k)}\cos\theta_j^{(k)}. \tag{1}$$

where A is the total area of the lining; n is the number of cracks; t is the width of crack, k; l is the length of crack, k; θ_i and θ_j donate the angles formed by the normal vector of the crack with the x_i axis and x_j axis; and β donate the weighting coefficients of crack width and length.

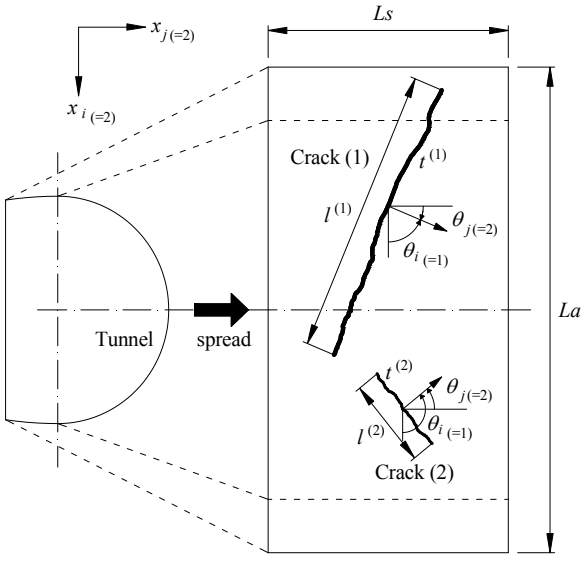

Fig. 1 The conceptual diagram of TCI

F_{11} and F_{22} obtained by the equation (1) indicated the longitudinal component and the transverse components of the TCI, respectively. The crack index F_0 was expressed as

the sum of longitudinal and transverse components as shown in equation (2). Associating equation (1) with equation (2), the crack index F_0 can be derived as equation (3).

$$F_0 = F_{11} + F_{22}. \tag{2}$$

$$F_0 = \frac{1}{A}\sum_{k=1}^{n}\left(t^{(k)}\right)^{\alpha}\left(l^{(k)}\right)^{\beta}. \tag{3}$$

It is an objective evaluation method without depending on the technical force of the inspection engineer. The width, length, direction of cracks were considered. This method has been widely used in the soundness evaluation of tunnel lining in Japan.

However, the relevance of tunnel lining stability and the cracks density in the lining was questionable. On the one hand, the intersection and distribution of cracks were not considered in TCI. On the other hand, some approximations have to be used in the calculation of crack index. For example, the creaks were always not straight lines, but they were divided into small segments and considered as straight lines to simplify the calculation. In addition, the calculation of TCI based on the statistical methods is extremely time consuming.

7.2.2 Concept of fractal dimension

The essential idea of fractional has a long history in mathematics that can be traced back to the 1600s. It was originally used to describe objects that have self-similarity features. The terms of fractal and fractal dimension were coined by mathematician Benoit Mandelbrot in 1975 (Mandelbrot 1967; Mandelbrot 1983). It was used to extend the concept of theoretical fractional dimensions to geometric patterns in nature. For example, the fractal dimension of a coastline quantifies how the number of scaled measuring sticks required to measure the coastline changes with the scale applied to the stick.

In fractal geometry, the fractal dimension is a ratio providing a statistical index of complexity comparing how detail in a fractal pattern changes with the scale at which it is measured. Moreover, it has been characterized as a measure of the space-filling capacity of a pattern that tells how a fractal scales differently from the space it is embedded in.

According to the definition, the fractal dimension could describe the density and complexity of the cracks in tunnel lining. In this case, it is a promising method to estimate the stability of tunnel lining according to the fractal dimension of cracks. The fractal dimension of cracks in a plane could be explained intuitively thinking of them as an object too detailed to be one-dimensional, but too simple to be two-dimensional. Therefore its dimension might best be described not by its usual topological dimension but by its fractal dimension, which in this case is a number between one and two.

7.2.3 Calculation method of fractal dimension

There are several formal mathematical definitions of fractal dimension that build on the basic concept of change in detail with change in scale (Falconer 1990). The box-counting dimension is the most widely used one (Larry 1998). In fractal geometry, the box-counting dimension, also known as Minkowski dimension, is a way of determining the fractal dimension of a set S in a Euclidean space R^n, or more generally in a metric space (X, d).

To calculate the dimension for a fractal S, imagine this fractal lying on an evenly spaced grid, and count how many boxes are required to cover the set. The box-counting dimension is calculated by seeing how this number changes as we make the grid finer by applying a box-counting algorithm. Suppose that $N(\varepsilon)$ is the number of boxes of side length ε required to cover the set. Then the box-counting dimension is defined as:

$$D = \lim_{\varepsilon \to 0} \frac{\log N(\varepsilon)}{\log(1/\varepsilon)} \tag{4}$$

Roughly speaking, the fractal dimension is the slope of the fitting line obtained by fitting a set of points ($\log N(\varepsilon)$, $\log \varepsilon$) (Chen 2005). In practical, the differential equation is used to estimate fractal dimension as shown in equation (5). This calculation is easy to achieve through a MATLAB program.

$$D \approx -\frac{d \log N(\varepsilon)}{d \log \varepsilon} \tag{5}$$

If the above limit does not exist, one may still take the limit superior and limit inferior, which respectively define the upper box dimension and lower box dimension.

7.3 Feasibility analysis of fractal dimension as a new health assessment index

To confirm the feasibility of fractal dimension as a new health assessment index, the influence factors, such as the density, the width, and the intersection of cracks, on the fractal dimension of tunnel lining cracks was studied in this part.

7.3.1 Influence of crack density on the fractal dimension

The fractal dimension of cracks shown in Fig. 2 was calculated according to the method described above. In Fig. 2, two cracks were extracted from a tunnel lining in the field, and the number of cracks was increased by copying these two cracks. As there are usually several to dozens of cracks in one span of tunnel lining, the crack number was set to be 4, 8, 16, 32, 48, and 64 in the six figures, and their fractal dimensions were determined to be 1.2745, 1.3062, 1.3690, 1.4504, 1.5291, and 1.5899, respectively. The relationship of fractal dimension and the number of cracks was shown in Fig. 3. According to the results, a linear relationship was found between fractal dimension and

number of cracks. The results illustrated that the fractal dimension could characterize the density of the cracks in case of regular distributed cracks.

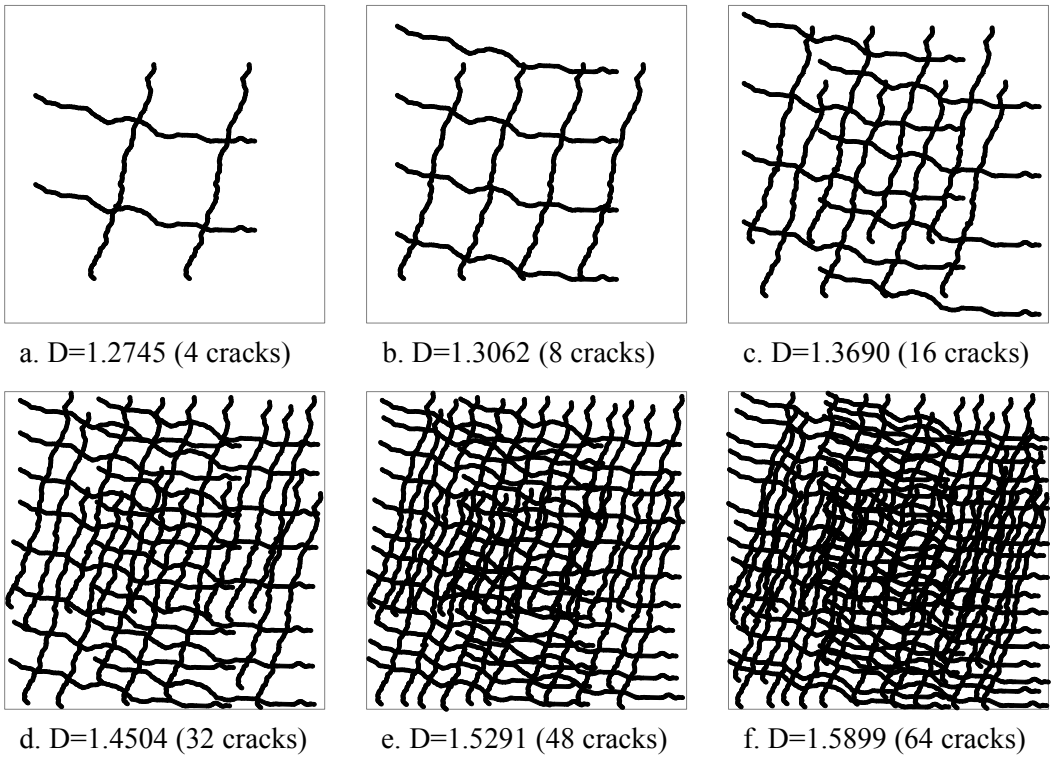

a. D=1.2745 (4 cracks) b. D=1.3062 (8 cracks) c. D=1.3690 (16 cracks)

d. D=1.4504 (32 cracks) e. D=1.5291 (48 cracks) f. D=1.5899 (64 cracks)

Fig. 2 The fractal dimension of different number of cracks

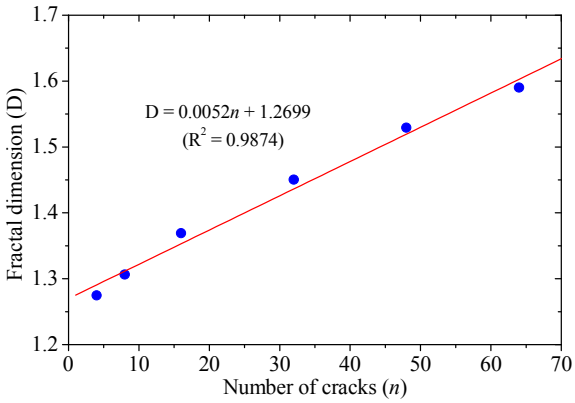

Fig. 3 The relationship of fractal dimension and the number of cracks

7.3.2 Influence of crack width on the fractal dimension

The fractal dimension of different width cracks was calculated and shown in Fig. 4. As the width of most cracks in tunnel lining distributed between 0.2 mm and 2.0 mm, the crack width is set to be 0.2mm, 0.5mm, 0.7mm, 1.0mm, 1.4mm and 2.0mm, respectively. The fractal dimensions were determined to be 1.0338, 1.1598, 1.2455, 1.2745, 1.3555,

and 1.3857, respectively. The relationship of fractal dimension and the width of cracks was shown in Fig. 5. There was a roughly linear relationship in fractal dimension and width of cracks. The results illustrated that the fractal dimension can also characterize the width of the cracks. Moreover, it was found that the slope of the fitting curve in Fig. 5 was much larger than the one in Fig. 3. The results certificated that the influence of crack width is larger than the crack density.

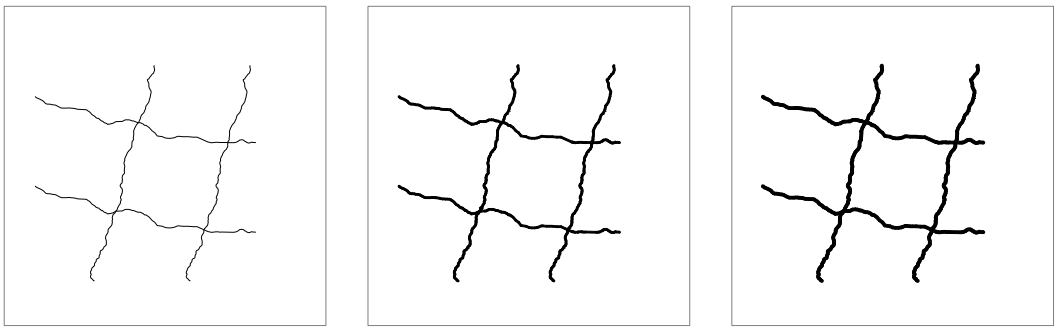

a. D=1.0338 (0.2mm) b. D=1.1598 (0.5mm) c. D=1.2455 (0.7mm)

d. D=1.2745 (1.0mm) e. D=1.3555 (1.4mm) f. D=1.3857 (2.0mm)

Fig. 4 The fractal dimension of different width cracks

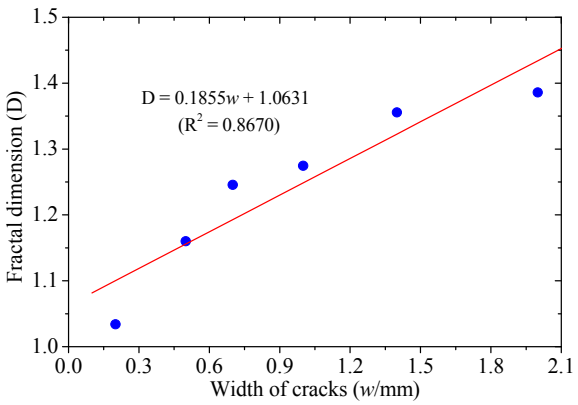

Fig. 5 The relationship of fractal dimension and the width of cracks

7.3.3 Influence of crack distribution on the fractal dimension

In this part, a comparative study was conducted to compare the advantages and disadvantages of TCI and fractal dimension. As shown in Fig. 6, four cracks were extracted from the tunnel lining in the field, and their locations were redistributed. In these six figures, the number of intersection points increased gradually.

Since the area of the cracks is the same, the TCI is a constant value for all these figures. However, the risk of cracks for different distribution is completely different. Generally, the risk of independent cracks is relatively small. However, the risk of tunnel lining collapse would be increased greatly when these cracks interconnect with each other. This is obviously a severe shortcoming of TCI, as the cracks distribution cannot be taken into account.

The fractal dimensions of these six figures were determined to be 1.2467, 1.2685, 1.2705, 1.2874, 1.3145, and 1.3376, respectively. The relationship of fractal dimension and the number of intersection points was shown in Fig. 7. The results illustrated that the fractal dimension increased with the number of intersection points in case of the same cracks. It is reasonable as the intersecting of different cracks makes the crack graphic more complex. The results showed that the fractal dimension can characterize the distribution of cracks, and especially identify the intersection of different cracks, which is closely related with the health condition of tunnel lining.

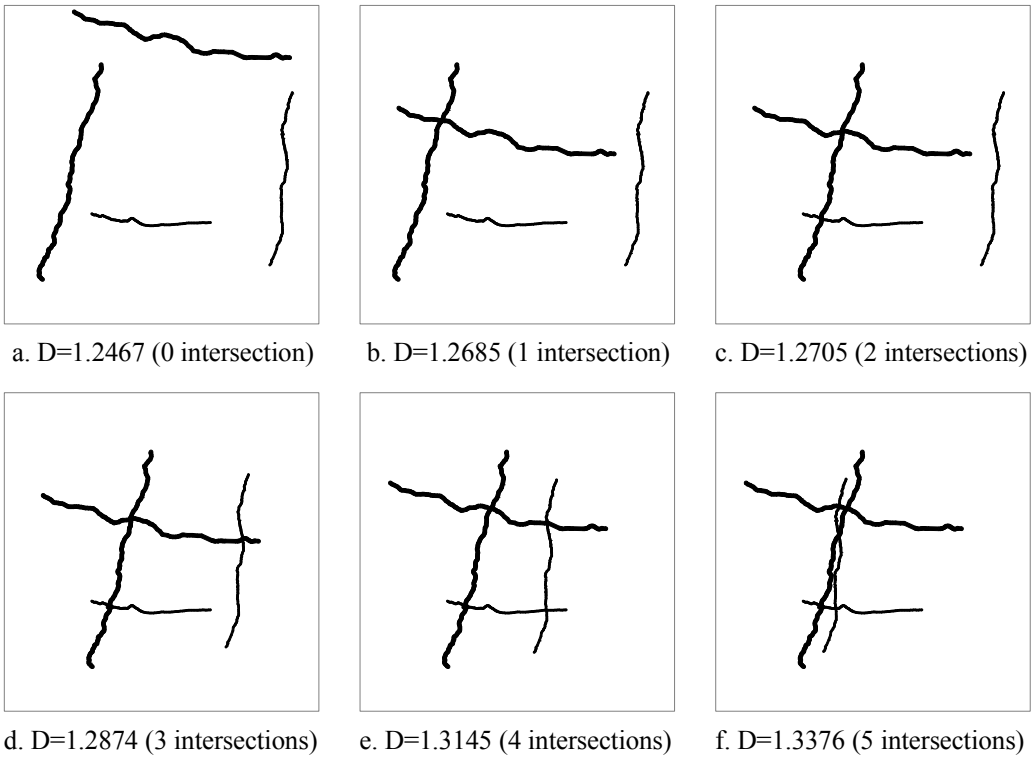

a. D=1.2467 (0 intersection) b. D=1.2685 (1 intersection) c. D=1.2705 (2 intersections)

d. D=1.2874 (3 intersections) e. D=1.3145 (4 intersections) f. D=1.3376 (5 intersections)

Fig. 6 The fractal dimension of different distributed cracks

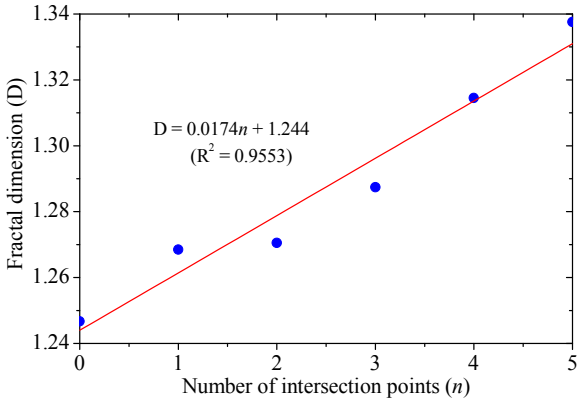

Fig. 7 Fractal dimension of different distributed cracks

7.4 A Case Study of Hidake Tunnel in Japan

To evaluate the validity of this new health assessment index and to study the quantitative correlation between the fractal dimension and the TCI of lining cracks, a field test was conducted at Hidake Tunnel located in Nagasaki Prefecture, Japan.

7.4.1. Basic condition of Hidake Tunnel

The Hidake tunnel (as shown in Fig. 8) was constructed in 1982 with the poling-board method. The tunnel length is 780m, with a total of 65 spans. The maximum depth is 25m. The thickness of the concrete lining is 0.7m at a part of the tunnel, and 0.55m at the other part. The materials of the concrete lining is C20 concrete. No surface prep was conducted on the concrete lining. No special anchorage between the tunnel and its lining was used. The surrounding rocks are sandstone, sand tuff, lapilli tuff, basalt, tuff breccia and lapilli tuff in different segments.

Due to the alteration of geological conditions and the deterioration of lining concrete, some defects such as cracks and seepages began appearing in the concrete lining after twenty years of service. The tunnel was also affected by the Kumamoto earthquakes, including a magnitude 7.0 main shock, on April 16, 2016.

Fig. 8 The Hidake Tunnel in Japan

7.4.2. Digital inspection test

To prevent the possible collapse of tunnel lining, digital inspection test was conducted to assess the extent of damage in different segments of the tunnel. The tunnel lining images were obtain by a photographing vehicle equipped with line sensor cameras. It is a non-contact detection technology that can track the information of the tunnel surface in a very short time [26, 27]. The process of extracting cracks was shown in Fig. 9. The round surface was automatically spread out to a flat surface as shown in Figs. 9a and 9b. The cracks were extracted from the image as shown in Figs. 9c and 9d by a crack identification program. The cameras was fixed on a car, and it can detect cracks with 0.2-mm resolution at a speed of 70 km/h. The cracks were extracted for all the 65 spans in Hidake Tunnel, and the results of 12 typical spans were shown in Fig. 10. The basic condition of the 12 typical spans were shown in Table 1.

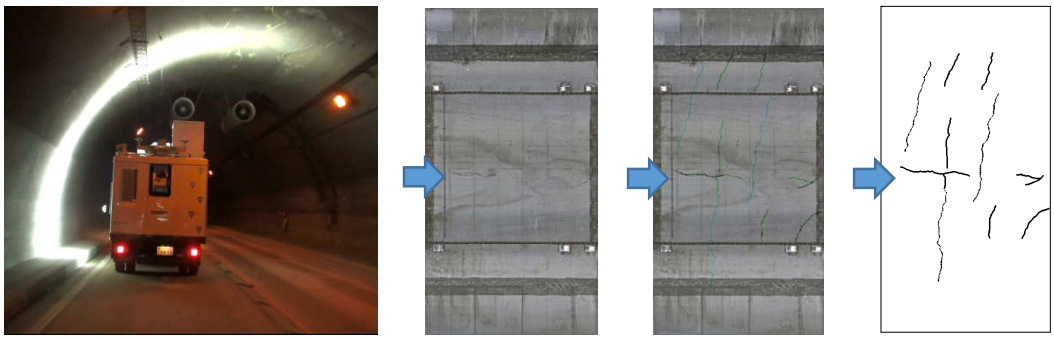

(a) **(b)** **(c)** **(d)**

Fig. 9 Extraction of cracks on tunnel lining surface: a, field test; b, unfolded crack image; c, identification of cracks; d, extraction of cracks

Table 1 The basic condition of the 12 typical spans

Span No.	Lining thickness	Inverted arch	Buried depth	Surrounding rock type	Surface prep	Concrete type	Construction method
16	0.55m	No	25m	sand tuff	No	C20	cast-in-place
18	0.55m	No	25m	sand tuff	No	C20	cast-in-place
34	0.70m	No	23m	basalt	No	C20	cast-in-place
36	0.70m	No	23m	basalt	No	C20	cast-in-place
42	0.55m	No	23m	basalt	No	C20	cast-in-place
46	0.55m	No	23m	tuff breccia	No	C20	cast-in-place
47	0.55m	No	23m	tuff breccia	No	C20	cast-in-place
50	0.55m	No	23m	tuff breccia	No	C20	cast-in-place
53	0.70m	No	23m	lapilli tuff	No	C20	cast-in-place
57	0.70m	No	23m	lapilli tuff	No	C20	cast-in-place
63	0.70m	No	2m	lapilli tuff	No	C20	cast-in-place
65	0.70m	Yes	0m	lapilli tuff	No	C20	cast-in-place

A large number of cracks were found in spans 46, 47, 50, 53, and 57, including some wide cracks, which would increase the risk of tunnel lining collapse greatly. There were a large number of small cracks in span 65, but no wide cracks were found. Few cracks were found in spans 16 and 18, which may mean a smaller risk of lining collapse. Moderate degree of cracks were found in spans 34, 36, 42, and 63.

The causes of cracking in Hidake Tunnel include: tectonic stress, earthquakes and concrete deterioration. The tectonic stress could result in a large number of axial cracks as shown in spans 47, 50, 53, 57, and 63. The earthquake, namely the Kumamoto earthquakes in 2016, could result in ring cracks as shown in spans 46, 47, 50, 53, and 57. The small cracks in spans 18, 34, 42, and 65 were mainly caused by the deterioration of concrete. Moreover, the cracking was influenced by the surrounding rock types. All the heavily cracked spans, including spans 46, 47, 50, 53, and 57, were located in tuff breccia or lapilli tuff, which belong to soft rock. In general, the actual cracking was affected by multiple factors.

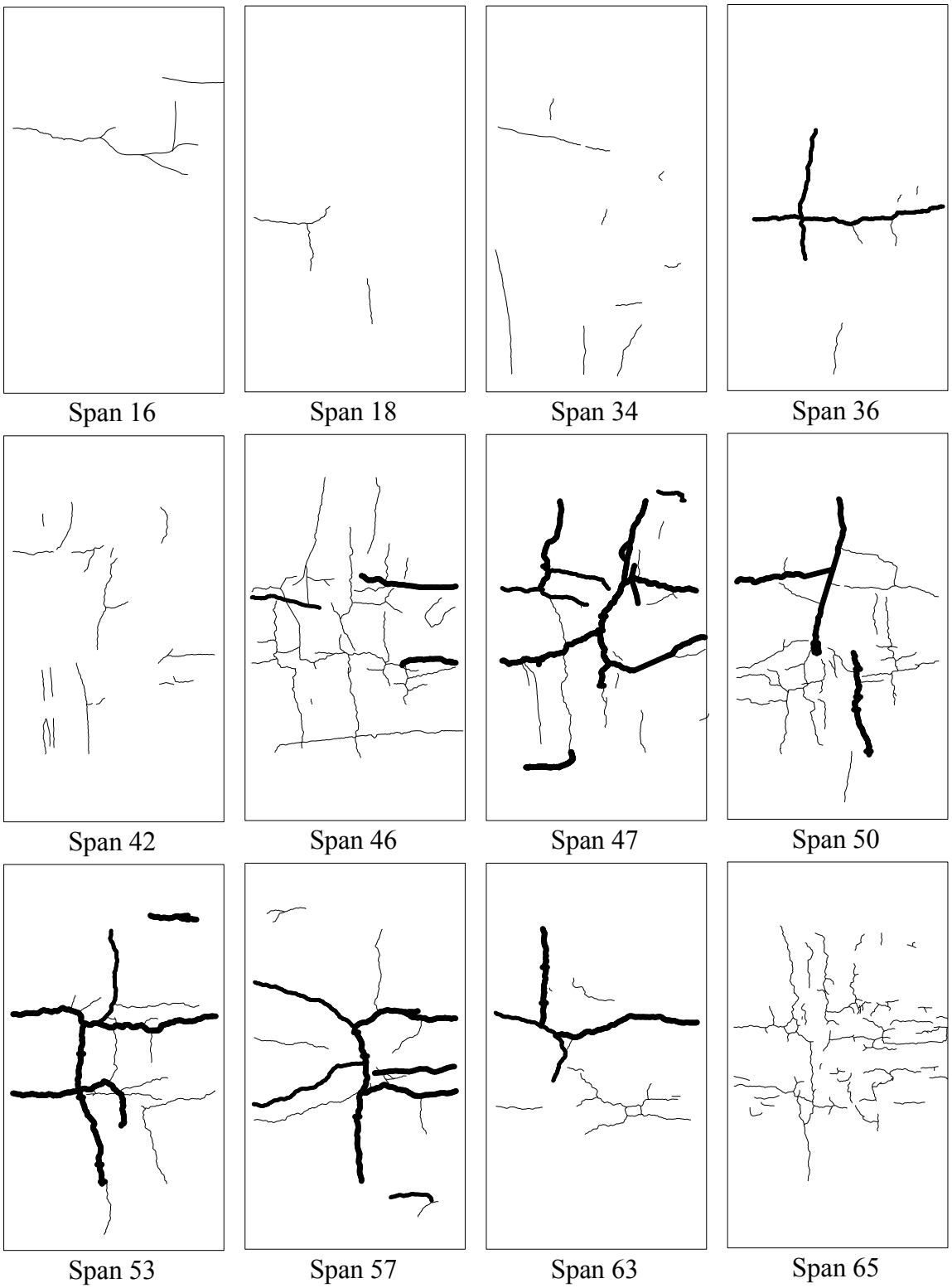

Fig. 10 The distribution of cracks in tunnel lining for twelve typical spans

7.4.3. Results and discussions

According to the methods described above, the fractal dimensions for all the 65 spans of Hidake Tunnel were calculated and shown in Table 2. The TCIs of all the 65 spans were also calculated through the statistical method. According to the fractal dimension and TCI shown in Table 2, their correlation was presented in Fig. 11. In addition, the results of 12 typical spans were marked in this figure.

Table 2 The results of TCI and fractal dimension for all the 65 spans of Hidake Tunnel

Span No.	TCI (10^{-5})	D	Span No.	TCI (10^{-5})	D	Span No.	TCI (10^{-5})	D
1	17.3533	1.2608	23	16.6357	1.2532	45	18.9605	1.2220
2	10.5798	1.1497	24	23.4324	1.2334	46	39.33	1.2527
3	9.5022	1.1395	25	18.5511	1.2783	47	65.3763	1.4182
4	9.2307	1.1630	26	15.5637	1.2665	48	32.1322	1.3375
5	9.0364	1.1102	27	18.6519	1.2487	49	40.2816	1.2906
6	0.9478	1.0031	28	22.1968	1.2994	50	44.3911	1.3006
7	13.9902	1.1786	29	3.9063	1.0679	51	19.656	1.2832
8	13.0135	1.2480	30	4.3127	1.1104	52	30.887	1.3173
9	12.0686	1.1608	31	4.2689	1.0844	53	51.8286	1.4087
10	16.0665	1.2386	32	6.5845	1.1474	54	32.2713	1.2633
11	7.7153	1.1560	33	3.3352	1.0306	55	32.0025	1.3007
12	3.9326	1.0665	34	4.5	1.0191	56	24.6288	1.2537
13	1.7505	1.0279	35	1.8892	1.0072	57	42.2909	1.3788
14	1.5339	1.0396	36	11.5899	1.2431	58	30.6416	1.2838
15	5.7424	1.1120	37	3.8941	1.0950	59	32.5696	1.2968
16	2.0397	1.1210	38	0.7143	1.0244	60	23.9007	1.2542
17	2.0151	1.0570	39	2.5996	1.0343	61	20.0143	1.2237
18	2.6453	1.0454	40	1.9042	1.0286	62	18.2604	1.1819
19	0.3402	1.0068	41	17.5861	1.1876	63	27.706	1.3257
20	4.163	1.0663	42	10.0495	1.0961	64	11.8213	1.1860
21	5.9599	1.0823	43	16.2336	1.1936	65	26.1172	1.2229
22	8.4668	1.1521	44	27.0087	1.2482			

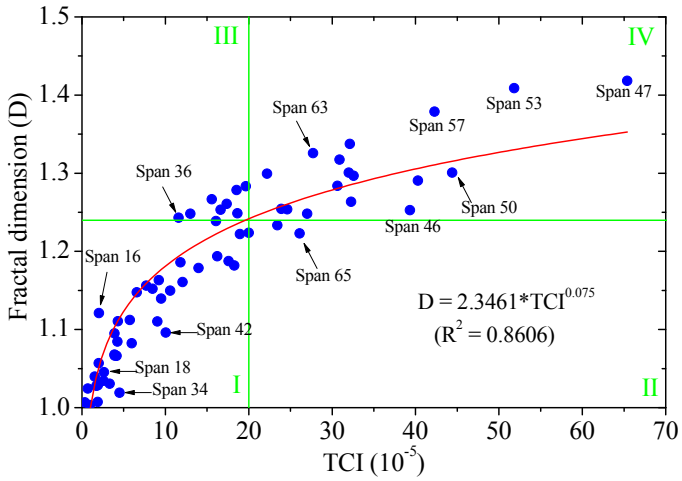

Fig. 11 The correlation between the TCI and the fractal dimension in field test

The results by two different methods can be fitted as a power function with a correlation coefficient of 0.8606. For most of the test spans, the results by the two different methods were consistent with each other. Obviously, there is a certain correlation between TCI and the new proposed index. However, for some points, the degree of risk is significantly different according to the two evaluation indices.

For span 18, there are only three small cracks, and both the TCI and the fractal dimension are in quite small states. Obviously, it is in a safe state. For span 16, there are several cracks and no wide crack is found. Therefore, the calculated TCI is quite small. Since these cracks have almost penetrate the entire lining, it is clear that the risk is underestimated. As the cracks are connected together, the calculated fractal dimension is significantly larger. This behavior indicated that the result by the new index is more consistent with the actual risk of the tunnel lining. Similar phenomenon is found in the results of spans 36 and 63, where the risk is also underestimated by the TCI. While, some wide cracks were found in the two spans, and their risk is relatively large by both methods.

For spans 34 and 42, the results were located below the fitting curve, which suggested that their risk was small according to the new index and large by the index of TCI. Since there are only some small and independent cracks in the two spans, the actual damage in the tunnel lining is not so serious. Therefore, the results by the new health assessment index are closer to the actual risk of the tunnel lining. For spans 46, 47, 50, 53, and 57, the risk of lining collapses is quite large by both health assessment indexes, which suggested that proper maintenance is extremely necessary.

The above results suggested that the current method, which evaluate the health status of tunnel lining only by the index of TCI, is far from perfect. It is necessary to use a different method in which the distribution of cracks can be considered. The significance

of the new evaluation index is that it can identify some unusual spans of tunnel lining and provide a basis for further internal testing. In addition, the calculation of fractal dimension is very simple and takes only a few minutes for one span. Meanwhile, a lot of time and work are need to get the TCI.

In engineering practice, the purpose of visual testing is to identify the areas where there is a need for further internal testing and to monitor the development of concrete lining damage. Generally, when TCI is larger than $20*10^{-5}$, further internal testing is required (Wu 2017). According to the fitting formula shown in Fig. 11, the corresponding fractal dimension was identified as 1.2386. The two thresholds divided Figure 11 into four parts: I, healthy according to both indexes; II, unhealthy according to TCI but healthy according to D; III, healthy according to TCI but unhealthy according to D; IV, unhealthy according to both indexes. Combining these two indexes, more damaged spans could be determined (part III), and the distribution of cracks could be considered. In particular, it is possible to find the unhealthy spans that the cracks almost penetrate the entire lining or the cracks are connected together. Moreover, if the TCI or D increased rapidly in a short period of time, further internal testing is required for these spans.

The fractal dimension of the cracks is a promising method in the health assessment of tunnel lining as shown in these tests. However, the impact factor of different elements, including the density, width, and distribution of cracks, were not fully determined. More field test data and comparative study were need to interpretation the results of the fractal dimension. Nevertheless, the new health assessment method of tunnel lining is a good complement to the conventional visual inspection method.

7.5 Conclusions

A new method was proposed for the health assessment of tunnel lining, which evaluate the lining states according to the fractal dimension of cracks. Based on the machine vision-based method, the crack image could be extracted efficiently. The fractal dimension of lining cracks in one span could be obtained in a few minutes, while the calculation of TCI based on the statistical methods was quite time consuming.

A series of comparative tests were conducted to evaluate the validity of this new method. The comparative tests confirmed that fractal dimension can characterize the density, width, and distribution of cracks. The results also certificated that the influence of crack width was larger than the crack density. The intersection of cracks, which will increase the risk of lining collapse, can also increase the fractal dimension, whereas the TCI keep constant.

The fractal dimensions of tunnel lining cracks were obtained according to the digital inspection test of Hidake Tunnel in Japan for all the 65 spans. In addition, the TCI was obtained through statistical methods. The correlation between the fractal dimension and

the TCI of tunnel lining was studied. The significance of the new evaluation index is that it can identify some unusual spans of tunnel lining and provide a basis for further internal testing. As a complement to the conventional visual inspection method, the fractal dimension of the cracks is a promising health assessment index.

References

Aktan, A. E.; Catbas, F. N.; Grimmelsman, K. A.; C. J. Tsikos, Issues in infrastructure health monitoring for management, Journal of Engineering Mechanics, ASCE, 2000, 126, 711–724.

Alves, L. M.; Chinelatto, A.L.; Grzebielucka, E.C.; Prestes, E.; Lacerda, L.A. Analytical fractal model for rugged fracture surface of brittle materials. Engineering Fracture Mechanics 2016, 162, 232–255.

Bhalla, B. S.; Yang, Y. W.; Zhao, J.; Soh, C. K. Structural health monitoring of underground facilities–Technological issues and challenges, Tunnelling and underground space technology, 2005, 20, 487–500.

Bisoi, A. K., & Mishra, J. On calculation of fractal dimension of images. Pattern Recognition Letters 2001, 22(6-7), 631–637.

Bolliger, J., Sprott, J. C., Mladenoff, D. J. Self-organization and complexity in historical landscape patterns. Oikos 2003, 100(3), 541–553.

Briggs, John (1992). Fractals: The Patterns of Chaos. London: Thames and Hudson. p. 148. ISBN 0-500-27693-5.

Chen, Y.Q., Lu, A.S., Hu, H.P. Summary of image analysis method based on fractal, Computer Engineering and Design 2005, 26(7), 1781–1784.

Falconer, K.J. Fractal Geometry: Mathematical Foundations and Applications, Wiley, Chichester, 1990.

Gao,Y.; Jiang Y. J.; Li, B. Estimation of effect of voids on frequency response of mountain tunnel lining based on microtremor method, Tunnelling and Underground Space Technology 2014, 42, 184–194.

Gao,Y.; Jiang Y. J.; Li, B. Voids delineation behind tunnel lining based on the vibration intensity of microtremors, Tunnelling and Underground Space Technology 2016, 51, 338–345.

Harte, David (2001). Multifractals. London: Chapman & Hall. pp. 3–4. ISBN 978-1-58488-154-4.

Hayashi, Y.; Imai, J. M. Yoshiduka, M. Suzuki, Y. Shigeta, K. Nakagawa, “Restoration

measures of tunnel experienced large deformation due to natural disaster, Doboku Gakkai Ronbunshu 2004, 756, 61–74.

Huang, H.; Sun, Y.; Xue, Y.; Wang, F. Inspection equipment study for subway tunnel defects by grey-scale image processing. Advanced Engineering Informatics 2017, 32, 188–201.

Jiang Y. J.; Gao,Y.; X. Wu. The nature frequency identification of tunnel lining based on the microtremor method, Underground Space 2016, 1, 108–113.

Larry S. Liebovitch. Tibor Toth. A fast algorithm to determine fractal dimensions by box counting. Physics Letters A 1989, 141(8–9), 386–390.

Li, W.; Xu, C.; Ho, S. C. M; Wang, B.; Song, G. Monitoring Concrete Deterioration Due to Reinforcement Corrosion by Integrating Acoustic Emission and FBG Strain Measurements. Sensors 2017, 17(3), 657.

Malmgren, L.; Nordlund, E.; Rolund, S. Adhesion strength and shrinkage of shotcrete, Tunnelling and underground space technology, 2005, 20(1), 33–48.

Mandelbrot, B. How long is the coast of Britain? Statistical self-similarity and fractional dimension. Science 1967. 156 (3775): 636–638.

Mandelbrot, B. The fractal geometry of nature. Macmillan. 1983. ISBN 978-0-7167-1186-5.

Shigeta, Y.; Tobita, T.; Kamemura, K.; Shinji, M.; Yoshitake, I., Nakagawa, K. Propose of tunnel crack index (TCI) as an evaluation method for lining concrete, Doboku Gakkai Ronbunshuu 2006, 62(4), 628–632.

Soheyli, M. R.; Akhaveissy, A. H.; Mirhosseini, S. M. Large-Scale Experimental and Numerical Study of Blast Acceleration Created by Close-In Buried Explosion on Underground Tunnel Lining, Shock and Vibration, 2016, Vol. 2016, Article ID 8918050, 9 pages.

Tian, W.; Han, N. Evaluation of damage in concrete suffered freeze-thaw cycles by CT technique. Journal of Advanced Concrete Technology 2016, 14(11), 679–690.

Wang, B.; Mo C.; He C.; Yan Q. Fuzzy Synthetic Evaluation of the Long-Term Health of Tunnel Structures. Appl. Sci. 2017, 7(2), 203.

Wang, J.; Ogawa, S. Effects of meteorological conditions on PM2.5 concentrations in Nagasaki, Japan, International Journal of Environmental Research and Public Health 2015, 12(8), 9089–9101.

Wang, J.; Ogawa, S. Analysis of dynamic changes in land cover based on landscape

metrics in Nagasaki, Japan, J. Appl. Remote Sens 2016,11(1), 016–022.

Wu, X., Jiang Y., Masaya K., Taniguchi T., and Yamato T. Study on the Correlation of Vibration Properties and Crack Index in the Health Assessment of Tunnel Lining. Shock and Vibration. 2017, 2017, 1-9.

Xie, H.; Sanderson, D. J. Fractal kinematics of crack propagation in geomaterials. Engineering Fracture Mechanics 1995, 50(4), 529–536.

Xie, H.; Sun, H.; Ju, Y.; Feng, Z. Study on generation of rock fracture surfaces by using fractal interpolation. International Journal of Solids and Structures 2001, 38(32-33), 5765–5787.

Xue, D. J.; Zhou, H. W.; Ren, W. G.; Zhao, B. Multi-fractal characteristics of joint geometric distribution of granite in Beishan. Rock and Soil Mechanics 2016, 37(10), 2937–2944

Yamada, T.; Sano, N.; Baba, K.; Shigeta,Y.; Yoshitake, I.; Nishimura, K. Evaluation method for soundness of lining concrete by tunnel-lining crack index, Doboku Gakkai Ronbunshuu 2009, 65(1), 11–16.

Yan, Q.; Zhang, C.; Lin, G.; Wang, B. Field monitoring of deformations and internal forces of surrounding rocks and lining structures in the construction of the Gangkou double-arched tunnel—a case study. Appl. Sci 2017, 7(2), 169.

Yu, B., Zhao, J., Fang, K., Tan, Y., Ning, J. Rock strength evaluation during progressive failure process based on fractural characterization. Marine Georesources and Geotechnology 2016, 34(8), 759–763.

Zhang, W.; Zhang, Z.; Qi, D.; Liu, Y. Automatic Crack Detection and Classification Method for Subway Tunnel Safety Monitoring. Sensors 2014, 14(10), 19307–19328.

8 Study on the correlation of vibration properties and crack index in the health assessment of tunnel lining

8.1. Introduction

The tunnels play an important role in the transportation projects. A large number of tunnels have been in service for decades all over the world, and they were mainly supported by concrete lining (Soheyli 2016). The persistent ageing and earthquake cause many problems to the concrete lining, such as cracking, corrosion and seepage (Aktan 2000; Malmgren 2005). The deterioration and damage of concrete lining decrease the integrity of tunnels and subsequently affect the safety of vehicle and pedestrian (Bhalla 2005).

The mechanical stability of a tunnel is influenced greatly by the cracks in the lining. Generally, stability assessment of tunnel lining is performed by visual inspection of the cracks (Hayashi 2004). However, it is questionable to predict tunnel lining failure only by the crack at the lining surface. The uncertainty relationship between the crack characteristics and the instability of tunnel lining require more alternative assessment methods. Some different methods, such as the magnetic method, ultrasonic method and ground penetrating radar method, were proposed (Jiles 1990; Poranski 1996). However, only local information of the structure can be measured in these techniques. A lot of time and cost are required to estimate the overall tunnel (Park 2008).

Recently, evaluating the structural condition according to the vibration properties of tunnel lining has attracted the attention of many researchers (Li 2008; Gao 2014; Dai 2015; Yu 2015; Lai 2016). However, these attempts have encountered great difficulties as the forced vibration test was adopted. The forced vibration test is not suitable for the damage detection of large-scale structures, where the huge reaction mass shakers are necessary (Peeters 2001). A more effective approach was proposed by the authors (Gao 2016), which evaluated condition of tunnel lining the by ambient vibration test. This method was proposed based on the basic physical principle: the stability of the tunnel lining is closely related with its strength and stiffness, and the strength and stiffness is closely related with the vibration properties. The damage of the tunnel lining will cause changes in the strength and stiffness, and subsequently affecting the vibration characteristics.

The vibration measurements by seismometer is a promising way to evaluate the global stability of tunnel lining. However, the field test data was limited. Especially, the data that can be compared with the conventional test method was not available. To evaluate the stability of tunnel lining more precisely and to evaluate the validity of this new method, it is meaningful to study the quantitative correlation between the crack index and the vibration characteristics.

However, the relevance of tunnel lining stability and the visible cracks on the surface of the lining was questionable. The stability of tunnel lining was also influenced by the voids and the cracks that were invisible. In addition, some approximations have to be used in the calculation of crack index. For example, the creaks were always not straight lines, but they were divided into small segments and considered as straight lines to simplify the calculation. The uncertainty relevance of TCI and tunnel lining state called for a different method to estimate the stability of tunnel lining.

8.2 Health Assessment of Tunnel Lining Based on the Ambient Vibration Test

As one type of ambient vibration, microtremor has attracted more and more attentions in the health assessment of concrete structures recently (Tuladhar 2004; Chatelain 2012). Microtremor is low amplitude ambient vibration of the ground caused by natural phenomena such as wind, ocean waves and volcano; as well as human activates such as movement of machinery in factories and motor cars.

Actually, all the objects are in vibration all the time. According to the basic vibration model, the natural frequency was basically expressed as equation (1). The damage of the objects always result in a localized reduction of the stiffness. Through analyzing the microtremor data, some useful properties of a structure, such as the amplitude and natural frequency, can be obtained.

$$\omega^2 = \frac{k}{M} \tag{1}$$

The ambient vibration test has been successfully used in many types of structures, including buildings and bridges (Júlio 2008; Michel 2008; Magalhas 2009). However, few attentions have been focused on the damage identification of tunnel linings, as they were embedded in rock mass and the vibration behavior was very complex. The vibration behavior of tunnel lining was influenced not only by its overall stiffness, but also by the interaction of surrounding rock mass and structure.

The tunnel lining can be treated as a cylindrical shell of which the thickness is

much smaller than the other dimensions. The thin shell theory can be used for the analysis of tunnel lining vibration. The vibration properties of thin elastic shell has been studied by many researchers (Cremer 1975; Soedel 1981). The Donnell-Mushtari shell theory is relatively simple and adopted to analyze the vibration characters of tunnel lining. The contacts of rock mass and concrete lining was considered as an elastic boundary which can be represented by the distributed springs as shown in Fig. 2.

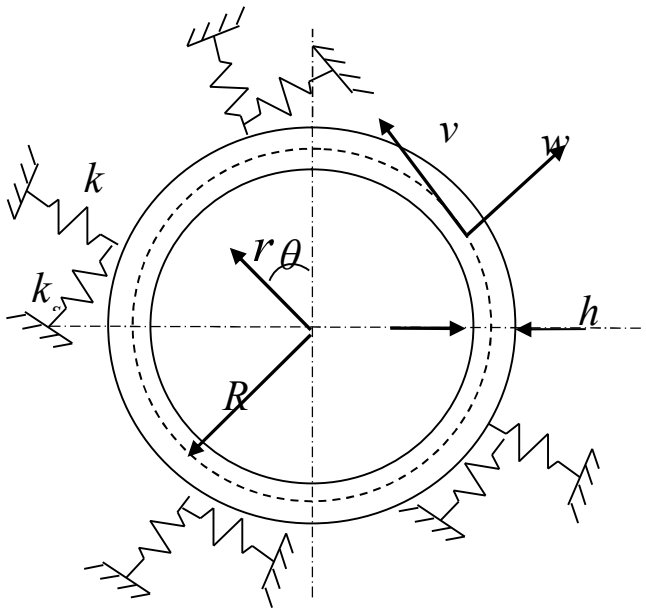

Fig. 2 The schematic of a circular cylindrical shell

The deformations mainly exist in the cross section. Meanwhile, the boundary condition is considered as the same along the axial direction. The displacement functions illustrated in Fig. 2 can be represented as follows:

$$u=0 \tag{2a}$$

$$v=v(\theta) \tag{2b}$$

$$w=w(\theta) \tag{2c}$$

The equations governing the vibrations in a plane strain model were expressed as (Jiang 2016):

$$\frac{\partial^2 v}{\partial \theta^2}+\frac{\partial w}{\partial \theta}+b\left(\frac{\partial^2 v}{\partial \theta^2}-\frac{\partial^3 w}{\partial \theta^3}\right)-\frac{R^2 k_s v}{K}=\frac{R^2}{K}\left(\rho h\frac{\partial^2 v}{\partial t^2}\right) \tag{3a}$$

$$\frac{\partial v}{\partial \theta}+w-b\left(\frac{\partial^3 v}{\partial \theta^3}-\frac{\partial^4 w}{\partial \theta^4}\right)+\frac{R^2 k_n w}{K}=\frac{R^2}{K}\left(-\rho h\frac{\partial^2 w}{\partial t^2}\right) \tag{3b}$$

Where $K = E\,h\,/\,(1 - \mu^2)$, E is Young's modulus of elasticity, μ is Poisson's ratio; b =

$h^2/12R^2$, h is the shell's thickness and R is the radius of the middle surface of the shell; v and w are the orthogonal components of displacement of the shell; ρ is density of the shell; k_n and k_s are the normal stiffness and shear stiffness of the concrete-rock interfaces. Using the Laplace transformation, the frequency factor of tunnel lining can be obtained:

$$\frac{\rho h R^2}{K}\omega^2 = 1 + \frac{R^2}{K}k_n \qquad \text{(n=0)} \qquad \text{(4a)}$$

$$\frac{\rho h R^2}{K}\omega^2 = \frac{1}{2}\left(1 + \frac{R^2}{K}k_n + \frac{R^2}{K}k_s + n^2 + bn^4\right) \pm \frac{1}{2}\sqrt{\left(1 + \frac{R^2}{K}k_n + \frac{R^2}{K}k_s + n^2 + bn^4\right)^2 + 4n^2 - 4\left(n^2 + \frac{R^2}{K}k_s\right)\left(1 + b^4 + \frac{R^2}{K}k_n\right)} \qquad \text{(n≠0)} \qquad \text{(4b)}$$

These theoretical studies laid the foundation for tunnel lining health assessment based on vibration properties. The main factors that affect the vibration of the tunnel lining include the Young's modulus, the Poisson's ratio, the thickness, the radius, the density of the lining. The normal stiffness and shear stiffness of the concrete-rock interfaces will also affect the tunnel vibration characteristics.

8.3 A Case Study of Hidake Tunnel in Japan

To evaluate the validity of this new method and to make a comparative analysis with the visual inspection test results, a series of field tests were conducted at Hidake Tunnel in Japan.

8.3.1. Basic condition of Hidake Tunnel

The Hidake tunnel (as shown in Fig. 3) located in Nagasaki Prefecture, Japan was taken as an example to study the quantitative correlation between the crack characteristics and the vibration characteristics. The tunnel was constructed in 1982 with the poling-board method. The tunnel length is 780m, and the maximum depth is 25m. The thickness of the concrete lining is 0.7m at a part of the tunnel, and 0.55m at the other part. The surrounding rocks are sandstone, sand tuff, lapilli tuff, basalt, tuff breccia and lapilli tuff in different segments.

Some defects such as cracks and seepages began appearing in the concrete lining

after twenty years of service, due to the alteration of geological conditions and the deterioration of lining concrete. The tunnel inspection was carried out in detail in 2013 and some defects in the tunnel lining were confirmed. The tunnel was affected by the Kumamoto earthquakes, including a magnitude 7.0 main shock, on April 16, 2016. The government decided to carry out a large-scale renovation to prevent the possible collapse of tunnel lining. The digital **visual inspection** and ambient vibration test were conducted before the renovation to assess the extent of damage to the tunnel. There are a total of 65 spans in Hidake Tunnel, and ten typical spans were selected in this study. The basic condition of the ten studied spans were shown in Table 1.

Fig. 3 Ambient vibration test of Hidake Tunnel in Japan

Table 1 The basic conditions of the concreate lining for ten studied spans

Span No.	Lining thickness	Inverted arch	Buried depth	Surrounding rock type
1	0.70m	Yes	3m	sandstone
12	0.55m	No	25m	sand tuff
16	0.55m	No	25m	sand tuff
18	0.55m	No	25m	sand tuff
20	0.55m	No	25m	lapilli tuff
35	0.70m	No	23m	basalt
42	0.55m	No	23m	basalt
49	0.55m	No	23m	tuff breccia
58	0.70m	No	23m	lapilli tuff
65	0.70m	Yes	0m	lapilli tuff

8.3.2. Digital visual inspection test

The Tunnel-lining Crack Index was calculated to evaluate the distribution density of the cracks on the lining surface. The process of extracting cracks was shown in Fig. 4. The continuous crack images as shown in Fig. 4a were obtain by a photographing vehicle equipped with line sensor camera. The round surface was automatically spread out to a flat surface. The cracks were extracted from the images as shown in Figs. 4b and 4c by a crack identification program. The cracks on tunnel lining surface were extracted for all the 65 spans in Hidake Tunnel, and the results of ten studied spans were shown in Fig. 5. In Fig. 5, the width of the cracks was shown through different colors. The black line means the cracks width is less than 0.5mm. The light blue line means the cracks width is between 0.5mm and 1mm. The green line means the cracks width is between 1mm and 2mm. The red line means the cracks width is large than 2mm.

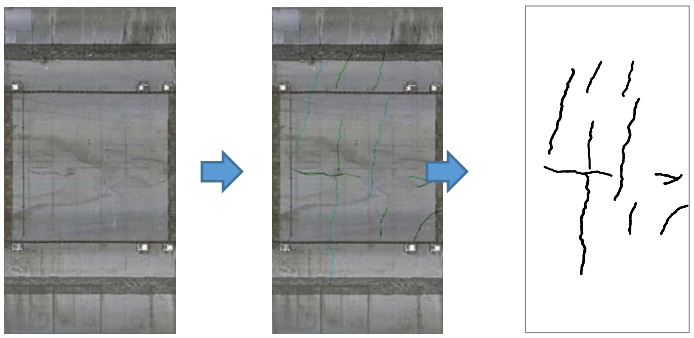

a **b** **c**

Fig. 4 Extraction of cracks on tunnel lining surface: a, unfolded crack image; b, identification of cracks; c, extraction of cracks

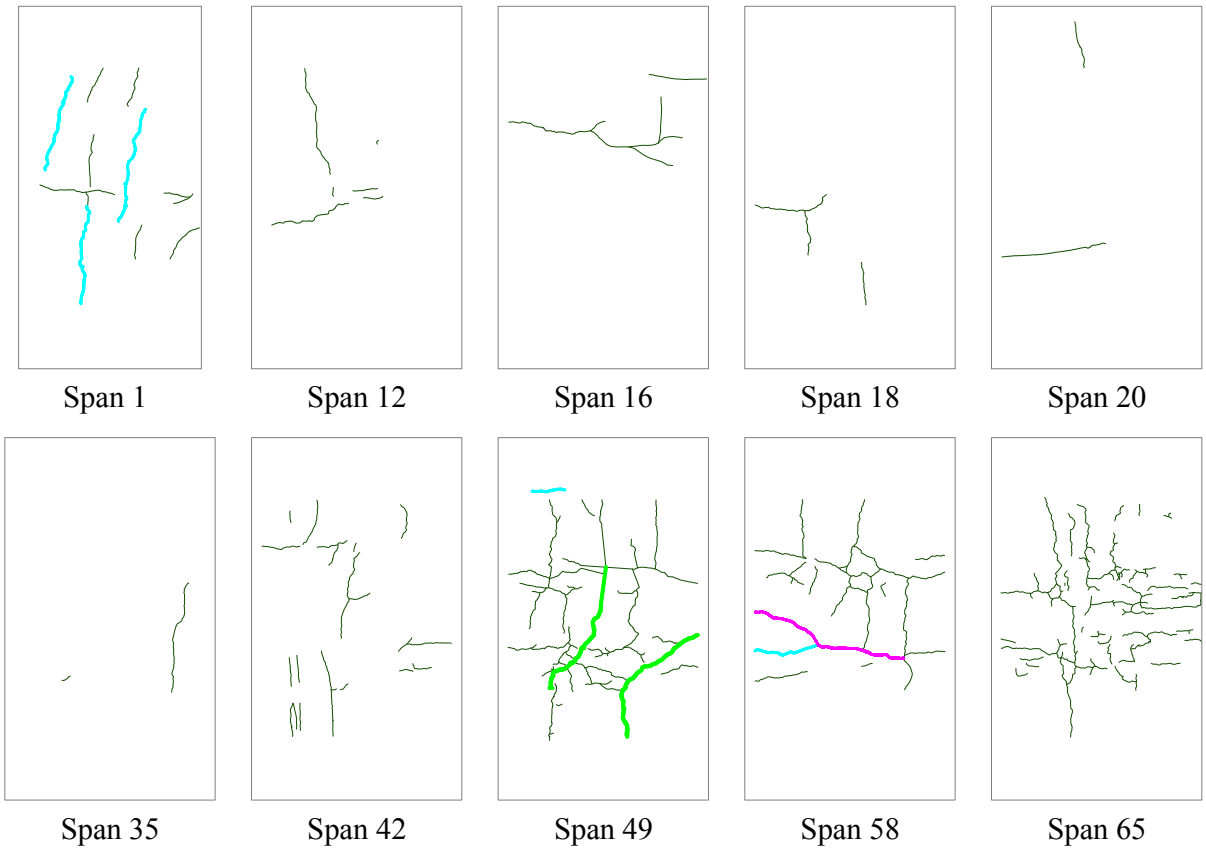

Fig. 5 Cracks **distribution on tunnel lining surface for ten studied spans**

The TCI for different spans was calculated and shown in Table 2. Many cracks were found in spans 1, 42, 49, 58, and 65. Especially in spans 49 and 58, some wide cracks were found, which would increase the risk of tunnel lining collapse greatly. There were a large number of small cracks in span 65, but no wide cracks were found. Few cracks were found in spans 12, 16, 18, 20, and 35, which may mean a smaller risk of lining collapse.

Table 2 Tunnel-lining Crack Index of the ten studied spans

Span No.	F_{11} (10^{-5})	F_{22} (10^{-5})	F_0 (10^{-5})
1	4.644	12.709	17.353
12	1.964	1.969	3.933
16	1.837	0.203	2.040
18	1.179	1.466	2.645
20	3.885	0.278	4.163
35	0.321	1.569	1.890
42	3.470	6.580	10.050

49	19.000	21.281	40.281
58	20.937	9.705	30.642
65	13.995	12.122	26.117

As described above, the relevance of tunnel lining stability and the visible cracks on the surface of the lining was questionable. So, the ambient vibration test was conducted to check the vibration properties of tunnel lining.

8.3.3. The vibration properties by ambient vibration test

(1) Measurement system

The microtremors were measured at the ten studied spans of Hidake Tunnel. As the vibration amplitude of the tunnel lining mainly caused by traffic is fairly small, usually about hundreds of mgals (cm/s^2), high accuracy accelerometers with a resolution of 1 mgal were utilized in microtremor measurements. The measurement system consists of three servo accelerometers, controller, data recorder and computer as shown in Fig. 6.

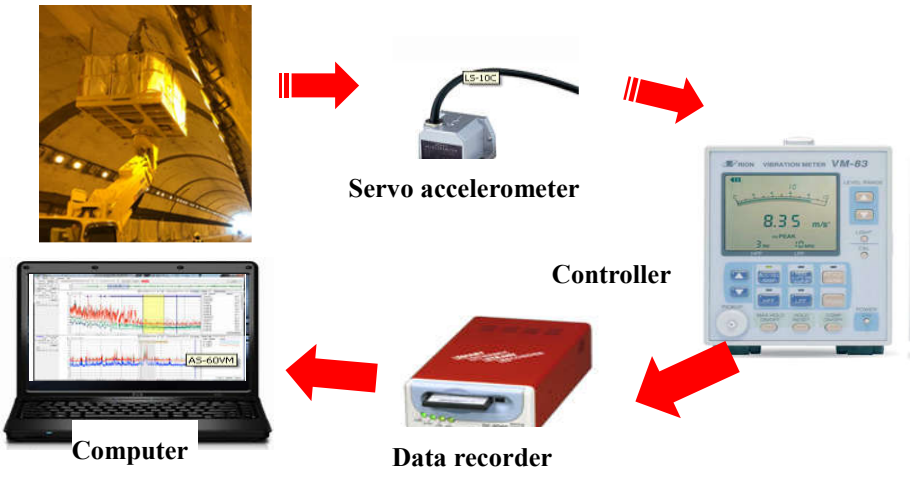

Fig. 6 The microtremor measurement system of tunnel lining

As the vibration properties of tunnel lining can reflect its overall stiffness, only one measuring point on the arch was selected for one span during the limited measuring time. The position of the test point was shown in Fig. 3. As the data record must be sufficiently long in order to reduce the influence of interfering signals. The measurements last for 180 seconds with an interval of 0.001 second.

(2) Ambient vibration test results

A part of the measured accelerations of tunnel lining in span 1 were shown in Fig. 7. The HOR-1 in the figure means the acceleration in tunnel axial direction. The HOR-2 means the acceleration in tunnel circumference direction. The VER means the direction

perpendicular to the tunnel lining surface.

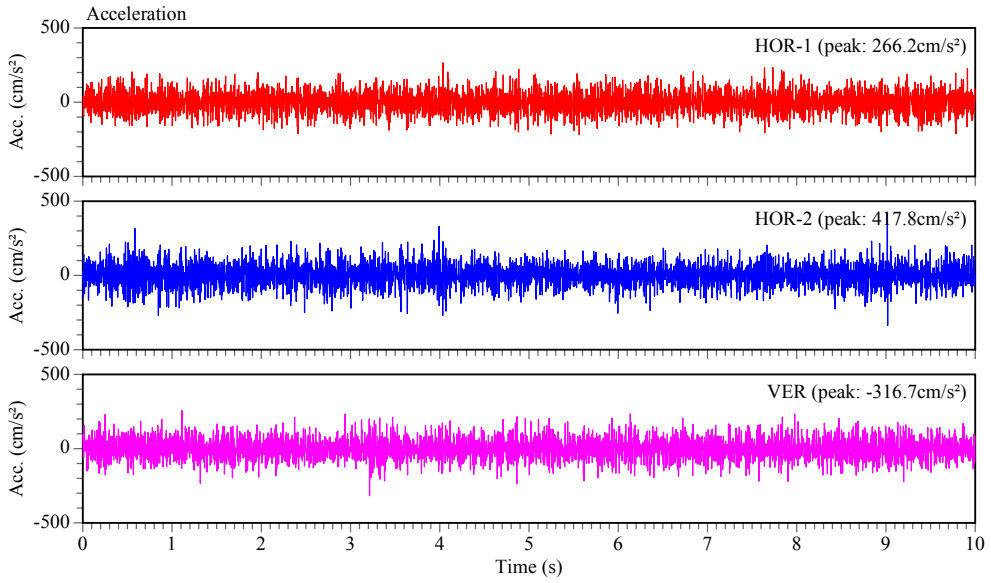

Fig. 7 A part of the measured microtremor in span 1

The results were easier to analyze in the frequency domain, and they can be obtained by Fourier transform from the time domain signal. In this study, a steady waveform of 10 seconds were selected for each measuring point. The interfering signals which may be induced by the heavy traffic were not used. The Fourier spectrum of vibration for ten studied spans were obtained, and some of the typical ones were shown in Fig. 8. In the calculation, the width of parzen window was adopted as 1Hz to smooth the curve.

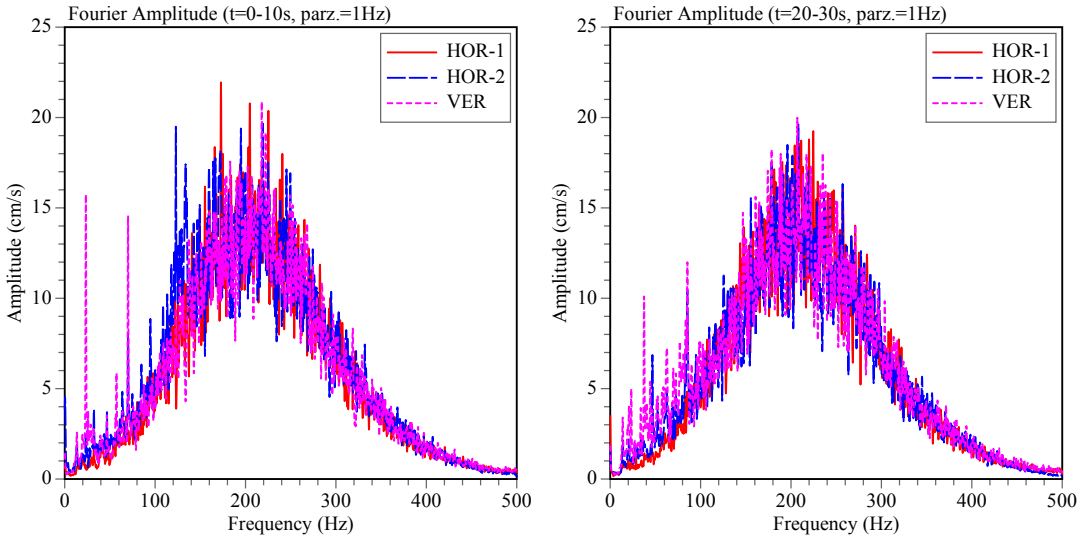

Span1 Span 18

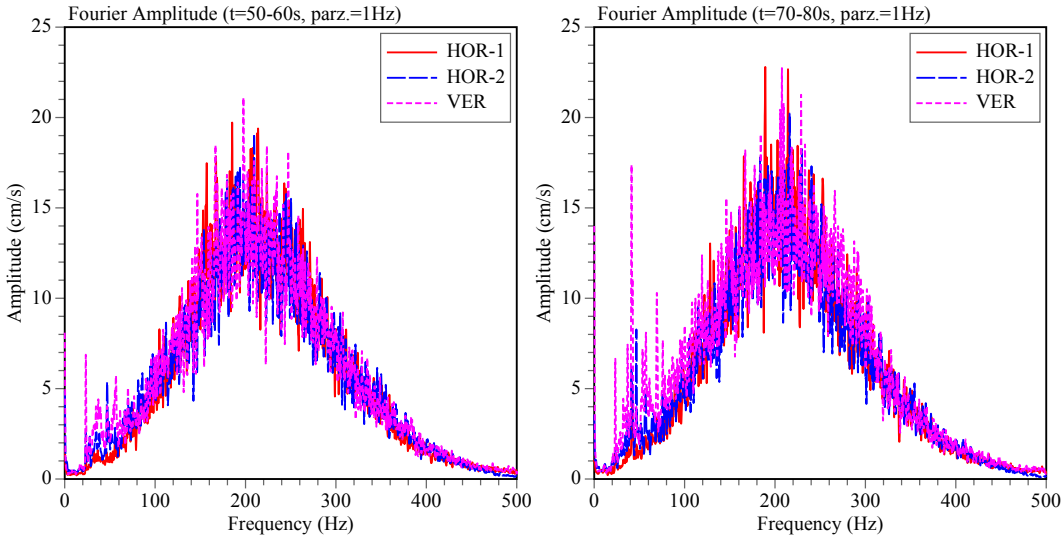

Span35 Span 49

Fig. 8 The velocity spectrum of vibration for spans 1, 18, 35 and 49

As shown in the above results, the microtremors of tunnel lining have a high noise ratio, and the frequency was distributed over a wide range, which made it difficult to identify the natural frequency exactly. Therefore, the average vibration amplitude over the spectrum were used to compare results for different spans. The average spectrum in three directions within the frequency domain of 50~200Hz was defined as S_x, S_y and S_z, respectively. The resultant average spectrum (RAS) can be obtained as equation (5). The resultant average spectrum of the concreate lining were shown Table 3.

$$\mathrm{RAS} = \sqrt{S_x^2 + S_y^2 + S_z^2} \tag{5}$$

Table 3 The resultant average spectrum (RAS) of the concreate lining

Span No.	S_x	S_y	S_z	RAS
1	7.566	8.591	7.525	13.699
12	7.435	7.329	7.488	12.847
16	7.420	7.071	7.612	12.767
18	7.470	7.586	7.904	13.260
20	7.480	7.484	8.478	13.559
35	7.389	7.213	7.681	12.869
42	7.642	7.238	7.209	12.757
49	7.657	7.578	8.441	13.686
58	7.983	8.771	7.952	14.279
65	7.927	8.384	8.605	14.393

The values of RAS range from 12.757 to 14.393. They were mainly influenced by the stiffness of concrete lining, stiffness of lining-rock joint, surrounding rock types and lining thickness. The values of RAS were supposed to be related with the stability of tunnel lining. According to the theoretical results, a larger stiffness of concrete lining will result in a smaller value of RAS. The stiffness of lining-rock joint has a similar influence. When the surrounding rock is hard rock, the value of RAS will be relatively small.

5. Correlation between the Crack Index and the Vibration Characteristics

The correlation between the crack index and the vibration characteristics were discussed in this part. According to the crack index TCI (F_0) shown in Table 2 and vibration characteristics RAS shown in Table 3, their correlation was presented in Fig. 9. The results by two different methods have shown a linear relationship with a correlation coefficient of 0.5538. The correlation coefficient is relatively small. It is because that the vibration characteristics was influenced by many factors, and the crack index is only one of them. Therefore, the correlation between the vibration characteristics and the crack index of tunnel lining was confirmed.

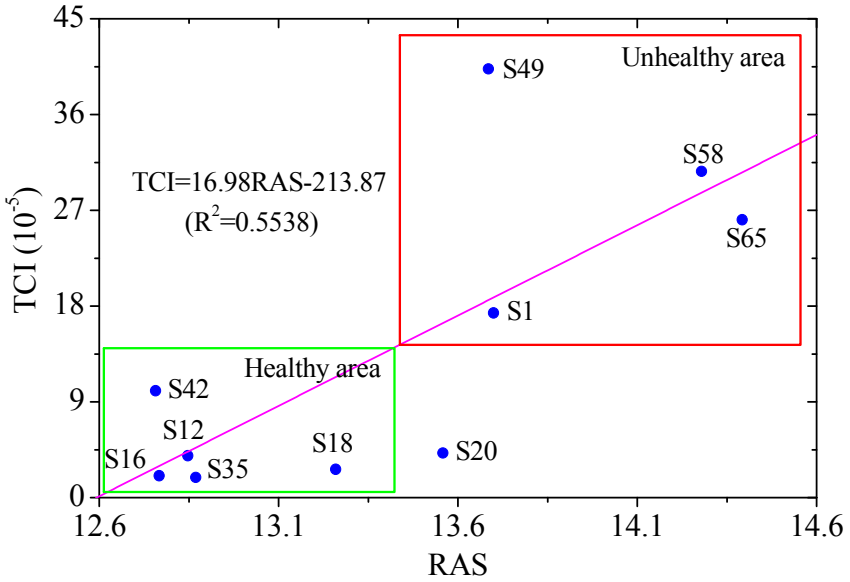

Fig. 9 The correlation between the crack index and the vibration characteristics

The concrete lining of Spans 1, 49, 58 and 65 were located in the unhealthy area by both methods. The Spans 12, 16, 35 and 42 were located in the healthy area by both methods. For these test points, the results by the two different methods were consistent with each other. However, the result of Spans 20 was quite different. It was located in

the healthy area by the conventional visual inspection test. But the ambient vibration test results showed that the value of RAS was quite large, and located in the unhealthy area. Probably, the vibration characteristics were influenced by the voids and the cracks on the inside of the lining that were invisible. This conjecture was confirmed during the grouting process, as significantly more cement was used in Span 20 than other healthy spans. Such neglected defects in conventional visual inspection test would pose a serious threat to tunnel safety.

Considering the basic conditions of the tunnel in Table 1, the factors that influence the vibration characteristics of the tunnel lining were discussed. Compared with the influence of crack index, the influence of lining thickness on the vibration characteristics was not significant. No obvious difference was found for both kinds of thickness of the lining. According to theoretical analysis, the vibration characteristics of tunnel lining should be affected by the thickness, but it was covered by other factors in these tests, especially the cracks in the lining.

The buried depth seemed to have an impact on the vibration of tunnel lining. The RAS values of Spans 1 and 65, that had small depth, were both relatively large. Obviously, a small load from the overlying rock mass will result in a large RAS value. On the other hand, these two spans were all at the ends of the tunnel, which may also affect the vibration characteristics. Inverted arches were used in Spans 1 and 65. Generally speaking, the inverted arches will reduce the values of RAS. However, this phenomenon was not reflected in the test results, as the vibration of Spans 1 and 65 were influenced by many other factors.

The surrounding rock types also affected the vibration characteristics of the tunnel lining. The hard surrounding rocks will result in small RAS values, which can be seen from the results of Spans 35 and 42. They were located in the basalt, which belong to hard rocks. The Spans 20, 58 and 65, located in the lapilli tuff, were all estimated to be unhealthy by the ambient vibration test. These results were consistent with the numerical simulation results carried out by the authors [25].

The results suggested that the conventional visual inspection test, which evaluate the health status of tunnel lining only by the surface cracks, was unreliable. It is necessary to use a different method that can check the internal structure of the lining. The ambient vibration test is a promising method in the health assessment of tunnel lining, which can estimate the overall stiffness and stability. However, the vibration

characteristics of tunnel lining were influenced by a large number of factors. More field test data and comparative study were need to interpretation the vibration test results. Nevertheless, the new health assessment method of tunnel lining is a good complement to the conventional visual inspection method.

6. Conclusions

The correlation of vibration properties and crack index of tunnel lining was studied in this paper. The development of health assessment methods for tunnel lining was first introduced. The visual inspection method was not reliable enough as the stability of tunnel lining was influenced by the voids and the cracks that were invisible.

A new method was proposed for the health assessment of tunnel lining, which evaluated the whole structural condition according to the vibration properties of tunnel lining. A series of field tests were conducted to evaluate the validity of this new method. The RAS of tunnel lining was identified according to the acceleration data of ambient vibration test of Hidake Tunnel. The TCI of studied spans in this tunnel was also obtained by digital visual inspection test.

The correlation between the crack index and the vibration characteristics was confirmed. However, some voids and cracks on the inside of the lining were neglected in conventional visual inspection test, which would pose a serious threat to tunnel safety. These defects were reflected in the new method. The significance of the new method is to identify the point where the vibration is abnormal and provide a basis for further internal testing. The vibration measurements by seismometer is an effective way to evaluate the global stability of tunnel lining. According to the ambient vibration test results, the influencing factors of tunnel lining safety was discussed in detail. A large number of field test data and detailed geological data were presented, which could be a reference for the comparative analysis in the future.

Reference

Aktan A. E., Catbas F. N., Grimmelsman K. A., and Tsikos C. J., “Issues in infrastructure health monitoring for management,” Journal of Engineering Mechanics, ASCE, Vol. 126, pp. 711–724, 2000.

Bhalla B. S., Yang Y. W., Zhao J., and Soh C. K., “Structural health monitoring of underground facilities–Technological issues and challenges,” Tunnelling and underground space technology, Vol. 20, pp. 487–500, 2005.

Chatelain J. L., Guillier B., Guéguen P., Fréchet J., Sarrault J., “Ambient Vibration Recording for Single-Station, Array and Building Studies Made Simple: CityShark II,” International Journal of Geosciences, Vol. 3, pp. 1168-1175, 2012.

Cremer L., Heckl M., Petersson B. A. T. “Structure-borne sound,” Physics Today, Vol. 28, pp. 81, 1975.

Dai Feng, Li Biao, Xu Nuwen, Zhu Yongguo, and Xiao Peiwei, “Stability Evaluation on Surrounding Rocks of Underground Powerhouse Based on Microseismic Monitoring,” Shock and Vibration, Vol. 2015, Article ID 937181, 9 pages, 2015.

Gao Y., Jiang Y. J., and Li B., “Estimation of effect of voids on frequency response of mountain tunnel lining based on microtremor method,” Tunnelling and Underground Space Technology, Vol. 42, pp. 184-194, 2014.

Gao Y., Jiang Y. J., and Li B., “Voids delineation behind tunnel lining based on the vibration intensity of microtremors,” Tunnelling and Underground Space Technology, Vol. 51, pp. 338–345, 2016.

Hayashi Y., Imai J., Yoshiduka M., Suzuki M., Shigeta Y., Nakagawa K., “Restoration measures of tunnel experienced large deformation due to natural disaster,” Doboku Gakkai Ronbunshu, Vol. 2004, No. 756, pp. 61–74, 2004.

Jiang Y., Gao Y., Wu X., “The nature frequency identification of tunnel lining based on the microtremor method,” Underground Space, Vol. 1, pp. 108–113, 2016.

Jiles D. C., “Review of magnetic methods for nondestructive evaluation,” NDT Int, Vol. 23, pp. 311-319, 1990.

Júlio E. N. B. S., Rebelo C. A. D. S., and Gouveia D. A. S., “Structural assessment of the tower of the tower of the University of Coimbra by modal identification,” Engineering Structures, Vol. 30, pp. 3468–3477, 2008.

Lai Jinxing, Wang Kaiyun, Qiu Junling, Niu Fangyuan, Wang Junbao, and Chen Jianxun, “Vibration Response Characteristics of the Cross Tunnel Structure, ” Shock and Vibration, Vol. 2016, Article ID 9524206, 16 pages, 2016.

Li X., “Study on free vibration analysis of circular cylindrical shells using wave propagation,” Journal of sound and vibration, Vol. 311, No. 3, pp. 667-682, 2008.

Magalhas F., Cunha A., and Cartano E., “Online automatic identification of the modal parameters of a long span arch bridge,” Mechanical Systems and Signal Processing, Vol. 23, pp. 316–329, 2009.

Malmgren L., Nordlund E., and Rolund S., “Adhesion strength and shrinkage of

shotcrete," Tunnelling and underground space technology, Vol. 20, No. 1, pp. 33-48, 2005.

Michel C., Guéguen P. and Bard P.Y., "Dynamic parameters of structures extracted from ambient vibration measurements: an aid for the seismic vulnerability assessment of existing buildings in moderate seismic hazard regions," Soil Dynamics and Earthquake Engineering, Vol. 28, pp. 593–604, 2008.

Park S., and Choi S., "Development of methodology for estimating the effective properties of containment buildings," Mid-term Report. Korea Institute of Nuclear Safety, KINS/HR-836, 2008.

Peeters B., Maeck J., and Roeck G.D., "Vibration-based damage detection in civil engineering: excitation sources and temperature effects," Smart Mater. Str., Vol. 10, pp. 518–527, 2001.

Poranski C. F., Greenawald E.C, and Ham Y. S., "X-ray backscatter tomography: NDT potential and limitations," Mater. Sci. Forum. Vol. 210–213, pp. 211–218. 1996

Shigeta Y., Tobita T., Kamemura K., Shinji M., Yoshitake I., Nakagawa K., "Propose of tunnel crack index (TCI) as an evaluation method for lining concrete," Doboku Gakkai Ronbunshuu, Vol. 62, No. 4, pp. 628-632, 2006.

Soedel W., "Vibrations of shells and plates", CRC Press, 1981.

Soheyli M. R., Akhaveissy A. H., and Mirhosseini S. M., "Large-Scale Experimental and Numerical Study of Blast Acceleration Created by Close-In Buried Explosion on Underground Tunnel Lining, " Shock and Vibration, Vol. 2016, Article ID 8918050, 9 pages, 2016.

Tuladhar R., Yamazaki F., Warnitchai P., Saita J., "Seismic microzonation of the Greater Bangkok area using microtremor observations," Earthquake Engineering and Structural Dynamics, Vol. 33, pp. 211-225, 2004.

Yamada T., Sano N., Baba K., Shigeta Y., Yoshitake I., Nishimura K., "evaluation method for soundness of lining concrete by tunnel-lining crack index," Doboku Gakkai Ronbunshuu, Vol. 65, No. 1, pp. 11-16, 2009.

Yu Qun, Tang Chun-An, Li Liancong, Cheng GuanWen, and Tang Lie-Xian, "Study on Rockburst Nucleation Process of Deep-Buried Tunnels Based on Microseismic Monitoring," Shock and Vibration, Vol. 2015, Article ID 685437, 17 pages, 2015.

9 Summaries

The deformation mechanics of tunnel, the support design method and health assessment method of tunnel lining are discussed in this doctoral thesis. The main conclusions are summarized in this chapter.

In Chapter 2, a modified strain-softening model is proposed to account for the non-linear evolution of residual strength under the influence of confining pressure. The parameters involved in the model are estimated via curvilinear regression analysis upon a series of stress-strain curves. The new model can realize the gradually transition from strain-softening features to idealized elastoplastic with the increasing of confining pressure. Numerical simulation is conducted to reproduce the post-failure behavior of the tested rock, and a better agreement can be observed for the new model, especially under high confining pressure conditions. The equations are programmed in the Visual Basic development environment, and a semi-analytical solution is achieved. The influence of post-failure behavior of rock mass is demonstrated through an illustrative case. The distributions of stress, displacement, principal plastic strain and transitional strength around the tunnel are presented, and the discrepancies of the idealized elastoplastic model, the strain-softening model and the new model are estimated quantitatively. In addition, the validity of semi-analytical solution is verified by numerical simulations. Parameters analysis shows that the post-peak behaviour of rock mass influence the tunnel convergence dramatically.

In Chapter 3, the influence of the confining-dependent Young's modulus in the ground reaction analyses was described. Considering the effect of confining pressure on Young's modulus, the stress and deformation of rock mass around tunnel was calculated by both analytical and numerical methods. The influence of confining-dependent Young's modulus in surrounding rock was estimated quantitatively. Finally, Tawara saka Tunnel in Japan was taken as an example to explain the influence of confining-dependent Young's modulus. The results show that the error with respect to the monitoring data was largely reduced with the confining-dependent Young's modulus model, which also indicate the necessary of considering the non-uniform distribution of Young's modulus

Chapter 4 presents a specifically designed rock bolt, which is promising to provide support for both squeezing and burst-prone rock mass encountered in mining and

tunneling at depth. Direct quasi-static pull tests are performed to examine the load capacity of tension and compression coupled anchor. The results show that the coupling action of tension to the rough rod and compression on the inner additional anchor by grout in different position can increase the ultimate bearing capacity of inner anchoring segment greatly. The performance of the conventional bolt and the new bolt subjected to fracture opening is tested. Results show that the load and strain concentration could result in premature failure of conventional rock bolt. However, the smooth segment of TCC Yielding bolt can easily detach from the grout under pull loading and provide a large deformation to accommodate rock dilations. Shear tests are performed to examine the performance of the new rock bolt subjected to fracture sliding. Results show that the smooth section of the new bolt specimen can deform freely to accommodate the sliding of fracture. The maximum shear displacement of the new bolt specimen is much larger than the conventional bolt specimen, which is promising a better ability to accommodate the large displacement sliding of fracture in the engineering practice.

In Chapter 5, the shear behavior of rock bolt inserted in the rough joints was investigated with a series of single shear tests under CNL condition. The results indicated that the shear behaviour of rock bolt was strongly influenced by the joint roughness, and quite different with the smooth joints. The shear dilatancy of bolted rock joints was smaller than the ones without rock bolt for the same JRC condition. A dimensionless mathematical model was established to predict the shear behaviour of rock bolt inserted in different roughness conditions. The maximum shear resistance of rock bolt f_T was evaluate as a negative exponential function of JRC. The maximum shear displacement of rock bolt f_s was evaluate as a linear function of JRC. Two tests with natural rough joints were conducted to verify the applicability of proposed mathematical model for the natural rough joints. The predicted values of f_T and f_s by the new model indicated good agreement with the test results with an average estimation error of 9.1%. The proposed model is capable of providing an accurate evaluation for the shear strength and shear displacement of rock bolt inserted in rough joints.

In Chapter 6, an interaction model is proposed to describe the interaction between the energy-absorbing rock bolt and the rock mass. The reinforcement mechanism of the energy-absorbing rock bolt in conventional tunneling is clearly demonstrated through an illustrative case study. The reinforcement effect of the energy-absorbing rock bolt under different conditions was estimated quantitatively, and its mechanical work transfer

ability is presented. In addition, the validity of the proposed method was verified through numerical simulations. Finally, a number of derivative cases were investigated to reveal the influence of the bolt and rock properties on the reinforcement effect and the bolt work transferred on the rock mass. In the case of higher in-situ stress or low-strength rock mass, the support effect of the energy-absorbing rock bolt is significantly improved, and the bolt absorbs more energy. Increasing the bolt installation density could always be helpful for the stabilization of the surrounding rock mass. However, additional rock-bolt length could hardly affect ground reinforcement because the bolt section embedded in the elastic region of the rock mass could barely help to constrain the elastic displacement release. The bolt should be installed no later than the stage of critical inner pressure, namely when the plastic region occurs. The results also confirmed that the bolt work transferred on the rock mass is a satisfactory estimation index, which is helpful for the support system design.

In Chapter 7, a new method was proposed for the health assessment of tunnel lining, which evaluate the lining states according to the fractal dimension of cracks. The comparative tests confirmed that fractal dimension can characterize the density, width, and distribution of cracks. The intersection of cracks, which will increase the risk of lining collapse, can also increase the fractal dimension. The correlation between fractal dimension and TCI of tunnel lining was studied. The significance of the new evaluation index is that it can identify some unusual spans of tunnel lining and provide a basis for further internal testing. As a complement to the conventional visual inspection method, the fractal dimension of the cracks is a promising health assessment index.

Chapter 8 examines the correlation of vibration properties and crack index of tunnel lining in evaluating risk of collapsing. A new method for the health assessment of tunnel lining was proposed, which can evaluate the whole structural condition according to the vibration properties of tunnel lining. A series of field tests were conducted to evaluate the validity of this new method and to make a comparative analysis with the visual inspection test results. The resultant average spectrum (RAS) of tunnel lining was identified according to the acceleration data of ambient vibration test of Hidake Tunnel in Japan. The Tunnel-lining Crack Index (TCI) was also obtained by digital visual inspection test. The correlation between the vibration characteristics and the crack index of tunnel lining was confirmed. However, the voids and the cracks on the inside of the lining were neglected in visual inspection test, which could pose a serious threat to

tunnel safety. The vibration measurements by seismometer is an effective way to evaluate the global stability of tunnel lining.

Chapter 9 summarizes the major conclusions and provides some discussions of this thesis.